Nano-Micro Letters

REVIEW

Cu-Based Materials for Enhanced C_{2+} Product Selectivity in Photo-/Electro-Catalytic CO_2 Reduction: Challenges and Prospects

Baker Rhimi[1], Min Zhou[1], Zaoxue Yan[1] ✉, Xiaoyan Cai[2] ✉, Zhifeng Jiang[1] ✉

HIGHLIGHTS

- The latest advancements in Cu-based catalysts for photocatalytic and electrocatalytic CO_2 reduction into C_{2+} products are reported.

- The relationship between the Cu surfaces and their efficiency in photocatalytic and electrocatalytic CO_2 reduction is emphasized.

- The opportunities and challenges associated with Cu-based materials in the CO_2 catalytic reduction applications are presented.

ABSTRACT Carbon dioxide conversion into valuable products using photocatalysis and electrocatalysis is an effective approach to mitigate global environmental issues and the energy shortages. Among the materials utilized for catalytic reduction of CO_2, Cu-based materials are highly advantageous owing to their widespread availability, cost-effectiveness, and environmental sustainability. Furthermore, Cu-based materials demonstrate interesting abilities in the adsorption and activation of carbon dioxide, allowing the formation of C_{2+} compounds through C–C coupling process. Herein, the basic principles of photocatalytic CO_2 reduction reactions (PCO$_2$RR) and electrocatalytic CO_2 reduction reaction (ECO$_2$RR) and the pathways for the generation C_{2+} products are introduced. This review categorizes Cu-based materials into different groups including Cu metal, Cu oxides, Cu alloys, and Cu SACs, Cu heterojunctions based on their catalytic applications. The relationship between the Cu surfaces and their efficiency in both PCO$_2$RR and ECO$_2$RR is emphasized. Through a review of recent studies on PCO$_2$RR and ECO$_2$RR using Cu-based catalysts, the focus is on understanding the underlying reasons for the enhanced selectivity toward C_{2+} products. Finally, the opportunities and challenges associated with Cu-based materials in the CO_2 catalytic reduction applications are presented, along with research directions that can guide for the design of highly active and selective Cu-based materials for CO_2 reduction processes in the future.

KEYWORDS Photocatalytic CO_2 reduction; Cu-based materials; Electrocatalytic CO_2 reduction
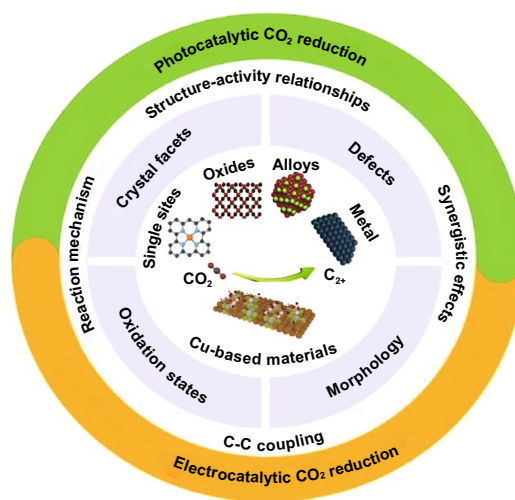
✉ Zaoxue Yan, yanzaoxue@ujs.edu.cn; Xiaoyan Cai, xycai@cumt.edu.cn; Zhifeng Jiang, jiangzf@ujs.edu.cn
[1] Institute for Energy Research, School of Chemistry and Chemical Engineering, Jiangsu University, Zhenjiang 212013, People's Republic of China
[2] School of Materials Science and Physics, China University of Mining and Technology, Xuzhou 221116, People's Republic of China

1 Introduction

Over the past few years, there has been a significant increase in the global energy consumption rate, resulting in massive use of fossil fuels such as natural gas, oil, and coal, which presently account for approximately 85% of primary energy supply [1–3]. Since fossil fuels, a non-renewable resource, are finite, their overconsumption has caused energy shortage issues. Moreover, the burning of fossil fuels is connected with excessive emissions of hazardous gases, including NO_x, SO_2, and CO_2. CO_2 is one of the primary gases that contribute to greenhouse effect, which results in rising global temperatures, ocean acidification, climatic variation, and so on [4–6]. Therefore, the mitigation of CO_2 emissions is critical in tackling the issues of global warming and energy depletion. In this context, numerous research studies have focused on developing effective ways for carrying out the artificial conversion of CO_2 in order to address these issues. It is intended to utilize CO_2 as a carbon feedstock in order to produce more value and useful hydrocarbon products through catalytic reactions. These products may then be used in a variety of industrial processes. These initiatives are crucial for promoting a sustainable approach toward energy production while also lowering the harmful impacts of carbon emissions on the environment.

As a chemical feedstock, CO_2 has attracted the attention of researchers across several fields, including thermocatalytic, electrocatalytic, and photocatalytic CO_2 conversion. However, the high cost of thermochemical carbon dioxide conversion limits its practical use. As a consequence, researchers are investigating alternative approaches for catalytically converting CO_2 into valuable products while reducing the cost of CO_2 conversion, such as wind and solar energy. Sustainable CO_2 conversion methods that use renewable energy sources at room temperature, such as photocatalytic CO_2 reduction reactions (PCO_2RR) and electrocatalytic CO_2 reduction reactions (ECO_2RR), have the potential to be more practical and cost-effective alternatives for CO_2 conversion [7, 8]. These methods differ in the source of electrons involved in the catalysis process, and the mechanisms by which this conversion is achieved are distinct: Photons are the primary source of electrons in photocatalysis, while an external electric field drives electrons in electrocatalysis.

Although the methodologies and underlying principles of PCO_2RR and ECO_2RR processes are different, their nature is essentially identical. These approaches employ catalysts to transform CO_2 into high value-added products; nevertheless, significant challenges remain in terms of CO_2 conversion efficiency and the selectivity of resulted products due to the inert nature of CO_2 molecules and the intricate nature of the process. This outcome arises from the thermodynamic stability and chemical inertness of CO_2, which is a linear molecule with completely oxidized carbon and an average C=O double bond energy of up to 804.4 kJ mol^{-1} (at 298 K) that requires substantial energy to break its carbon–oxygen (C–O) bonds [9, 10]. The thermodynamically stable nature of CO_2 makes it challenging to catalyze the CO_2 conversion process, and the inertness of its molecular structure limits the number of catalytic sites and affects the reaction selectivity, leading to low yields of value-added products. Additionally, the complexity of the CO_2 conversion process makes it difficult to optimize conditions for high activity and product selectivity, which limits the overall CO_2 conversion efficiency. These challenges underline the need for improvements in CO_2 conversion technologies, particularly in respect to developing efficient catalysts that enhance CO_2 adsorption and activation to promote higher activity and selectivity of the process. Meanwhile, finding the right catalyst for each method requires a deep understanding of the underlying mechanism of each approach.

In general, the CO_2 reduction reaction (CO_2RR) is a complex chemical process that consists of a series of electron transfer steps, hydrogenation, C–C bond coupling, and intermediate compounds. At present, products obtained from CO_2RR are often classified into C_1 and multi-carbon C_{2+} compounds. The representative C_1 compounds such as methane (CH_4), carbon monoxide (CO), methanol (CH_3OH), formaldehyde (CH_2O), and formic acid (HCOOH) have been extensively researched, whereas the formation of C_{2+} products, including but not limited to ethylene (C_2H_4), ethane (C_2H_6), ethanol (C_2H_5OH), and propanol (C_3H_7OH), poses a significant challenge because of the complex reaction pathways along with competitive reactions. Table 1 summarizes the possible reactions of CO_2RR to C_1 and C_{2+} products and their market prices [11–14]. Based on the market price point of view, C_{2+} products are more attractive in comparison with C_1 products. Thus, it is effective to produce C_{2+} through a single process via the CO_2RR. Figure 1 displays the annual count of scholarly research articles and review papers published within the timeframe of 2012–2022. The data collected from the Web of Science database indicates

Table 1 Products obtained from CO_2 reduction with their redox potentials relative to NHE (at pH 7) and their market prices

Reaction	E^0_{redox} vs. NHE (V)	Product	Market price ($/kg)	Equations
$CO_2 + e^- \rightarrow CO_2^-$	-1.90	CO_2^-	–	(1)
$CO_2 + 2H^+ + 2e^- \rightarrow CO_{(g)} + H_2O$	-0.53	Carbon monoxide	0.06	(2)
$CO_2 + 2H^+ + 2e^- \rightarrow HCOOH_{(aq)}$	-0.61	Formic acid	0.74	(3)
$CO_2 + 4H^+ + 4e^- \rightarrow HCHO_{(aq)} + H_2O$	-0.48	Formaldehyde	0.8	(4)
$CO_2 + 6H^+ + 6e^- \rightarrow CH_3OH_{(aq)} + H_2O$	-0.38	Methanol	0.58	(5)
$CO_2 + 8H^+ + 8e^- \rightarrow CH_{4(g)} + 2H_2O$	-0.24	Methane	0.18	(6)
$2CO_2 + 8H^+ + 8e^- \rightarrow CH_3COOH_{(aq)} + 2H_2O$	-0.31	Acetic acid	2.9	(7)
$2CO_2 + 12H^+ + 12e^- \rightarrow C_2H_{4(g)} + 4H_2O$	-0.34	Ethylene	1.3	(8)
$2CO_2 + 12H^+ + 12e^- \rightarrow C_2H_5OH_{(aq)} + 3H_2O$	-0.32	Ethanol	1.0	(9)
$2CO_2 + 14H^+ + 14e^- \rightarrow C_2H_{6(g)} + 4H_2O$	-0.51	Ethane	4.0	(10)
$3CO_2 + 18H^+ + 18e^- \rightarrow C_3H_7OH_{(aq)} + 5H_2O$	-0.32	Propanol	1.43	(11)
$2H^+ + 2e^- \rightarrow H_{2(g)}$	-0.41	Hydrogen	–	(12)
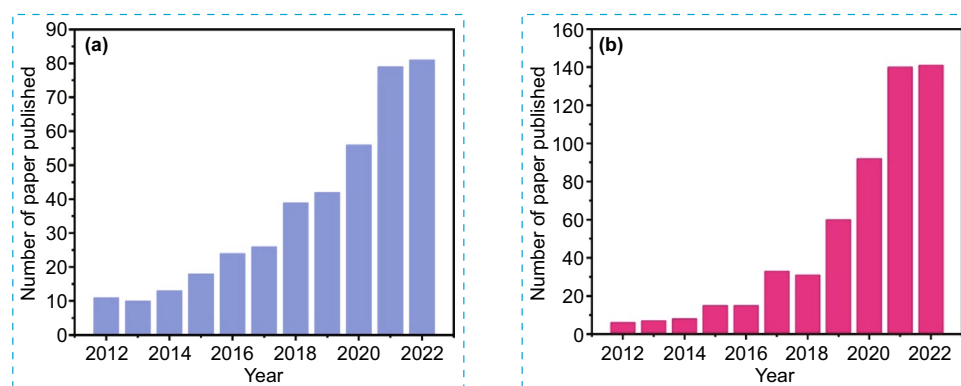
Fig. 1 The number of published articles between 2012 and 2022 retrieved from the Web of Science database: **a** photocatalytic CO_2 reduction to C_{2+} products and **b** electrocatalytic CO_2 reduction to C_{2+} products

an increasing interest among the scholarly community in the topic of photocatalytic and electrocatalytic CO_2 conversion into highly valuable C_{2+} compounds. This highlights the significance of research in this area as it could potentially offer solutions for combating climate change and energy shortage.

Over the recent decades, significant efforts have been made to enhance the selectivity of C_{2+} products and investigate the various factors that influence their distribution. Copper (Cu) displayed distinctive properties in converting CO_2 into C_{2+} chemicals such as ethylene, ethane, and ethanol, in both photocatalytic and electrocatalytic CO_2 reduction [15–19]. Copper is a readily available and cost-effective element that is abundant in the earth's reserves. It possesses multiple oxidation states, which allow for the formation of various copper-based materials such as cuprous oxide (Cu_2O) and copper oxide (CuO). CuO and Cu_2O semiconductors possess narrow bandgaps of 1.7 and 2.2 eV, respectively, making them efficient in capturing visible light energy [20, 21]. Additionally, the sufficiently negative conduction band (CB) position and the ability to effectively adsorb CO_2 make these materials efficient photoactive catalysts for CO_2 reduction [22, 23]. For instance, several structural factors, including surface states, surface defects, particle size, morphology, and crystal facet have been identified to affect the catalytic performance of Cu-based materials in PCO_2RR and ECO_2RR [24–27]. However, the synergy between these factors further complicates the understanding control of CO_2RR product selectivity. According to a recent report, the valance state of the Cu^{n+} $(0 < n < 2)$ that is present on the surface of catalysts is a crucial factor in governing C–C coupling in PCO_2RR and ECO_2RR processes. A recent study by Zhao et al. [27]

demonstrated that Cu^{2+} species present on the catalyst's surface underwent reduction to Cu^+ by photoinduced electrons, creating active sites that captured the in situ generated *CO intermediate and thereby facilitating the subsequent C–C coupling reaction. Nevertheless, maintaining the stability of Cu^+ species in aqueous solutions remains a challenging problem, as it is important for prolonging the lifetime of *CO intermediate and enhancing the CO_2 reduction into C_{2+} products. Therefore, understanding the links between the selectivity of end products and the valence state/coordination environment of copper species has been a subject of significant interest. To date, numerous electrocatalysts have been explored for the ECO_2RR, each yielding specific reduction products. The types and the number of desired products can be adjusted by fine-tuning the binding energy of adsorbed intermediates, including *CO, *COOH, *CHO, and *COH. For example, when the interaction between the electrocatalyst surface and reduction intermediates is relatively weak, the primary products are CO and formate ions ($HCOO^-$). This occurs because, in cases of weak binding, the C–O bond in these intermediates. Conversely, if electrocatalysts strongly bind *CO intermediates, the production of CO and $HCOO^-$ is limited. This is because the *CO intermediate remains attached to the catalyst surface for a more extended period, allowing it to undergo further reduction into other products. Among several catalysts investigated, Cu stands out as a unique metal because it can efficiently produce C_{2+} products including hydrocarbons and alcohols [28, 29]. The basic explanation for its ability to produce C_{2+} products is that Cu binds *CO neither too weakly nor too strongly [30, 31]. Nevertheless, the selectivity of bare Cu electrodes for particular products is generally poor, leading to the simultaneous formation of a range of reduction products. On a microscopic level, the underlying reason for Cu's poor selectivity lies in its moderate binding affinity for most reaction intermediates. Cu_2O exhibits similar characteristics to metallic copper in terms of its ability to adsorb and activate CO_2 that leads to the promotion of C–C bond coupling and the generation of C_{2+} chemical compounds. During the ECO_2RR process, Cu_2O shows rapid surface reconstruction which converts a portion of Cu^+ to Cu^0. Cu^0/Cu^+ pairs exhibit a synergistic effect that enhances the *CO adsorption on Cu_2O surface, improving the selectivity toward C_{2+} products [32–34].

Despite the significant progress made in photocatalytic and electrocatalytic CO_2 reduction, the factors that influence the ability of copper containing catalysts to tune the reaction mechanism and the selectivity toward C_{2+} products are not yet well understood. Herein, we report the latest advancements in Cu-based materials as catalysts for PCO_2RR and ECO_2RR with the aim of gaining a deeper comprehension of the structure–activity relationships. The schematic illustration of this review is shown in Fig. 2. The review begins with the fundamentals of photocatalytic and electrocatalytic CO_2RR. In particular, we summarize the detailed mechanisms and possible reaction pathways for CO_2 reduction to C_{2+} products on various Cu-based materials. We then introduce the application of Cu-based materials in PCO_2RR and ECO_2RR to C_{2+} products. To gain an in-depth knowledge of the factors that impact the catalytic performance of Cu, we have classified copper-based materials into various categories including Cu metal, Cu oxides, Cu alloys, and Cu SAs species. Finally, the main challenges to be resolved and the future perspective for Cu-based materials in converting CO_2 into C_{2+} products are envisioned.
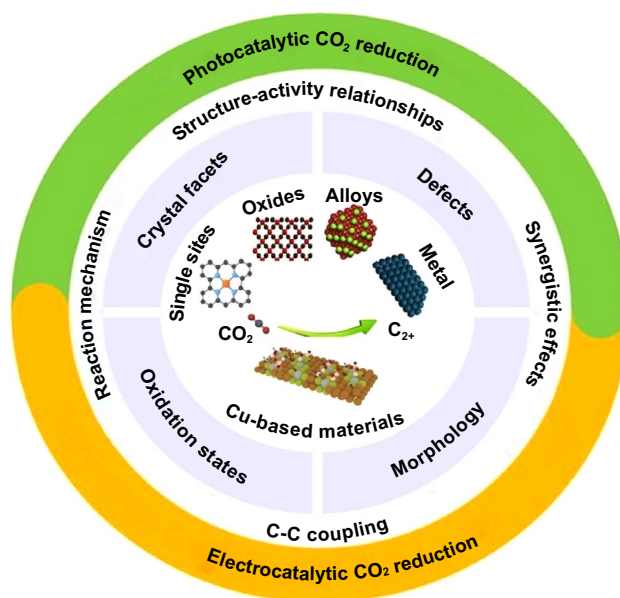

Fig. 2 Schematic illustration of the review article

2 Fundamental Understanding of the Mechanisms of CO_2 Reduction Reaction

2.1 Basic Principles of Photo- and Electro-catalytic CO_2 Reduction

2.1.1 Photocatalytic CO_2 Reduction Reaction

PCO_2RR presents a promising method for directly using solar energy to transform CO_2 into valuable products. Photocatalytic reactors are generally configured in two ways: either using particulate semiconductor photocatalysts suspended in a CO_2 gas-saturated solution or using uniformly distributed and immobilized photocatalysts mixed with CO_2 gas and H_2O vapor on a substrate. In principle, PCO_2RR process involves three stages: absorption of light (photons), separation and transfer of charges, and subsequent reactions that take place at the interface (Fig. 3). The overall efficiency of the process is determined by multiplying the efficiency of each step. The application of PCO_2RR process faces several challenges. In particular, the simultaneous absorption of light across a wide range of solar spectrum and carrying out oxidation–reduction reactions with a single semiconducting material is difficult. Materials with wide bandgaps, such as titanium dioxide (TiO_2) and zinc oxide (ZnO), exhibit photoactivity within the ultraviolet (UV) spectrum, while narrow bandgap semiconductors such as Cu_2O show activity in the visible NIR range; however, the band potentials of Cu_2O
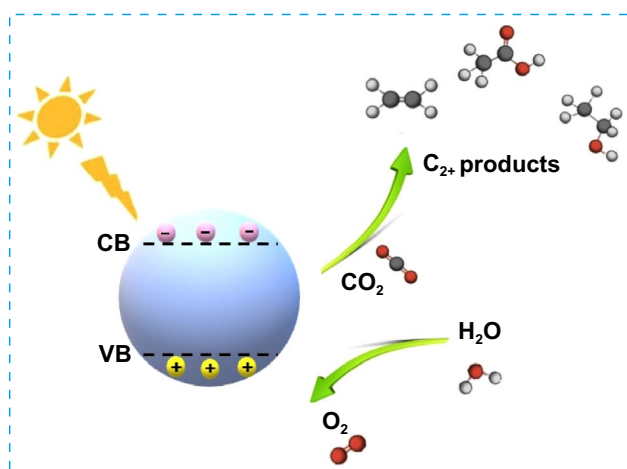

Fig. 3 Photocatalytic CO_2 reduction mechanism on a catalyst surface

semiconductors are not conducive to mediating both reduction and oxidation reactions simultaneously. As a result, single-component systems have lower efficiency for photocatalysis. In order to address this issue, researchers have attempted to develop heterostructures (in forms of nanowires, nanobelts, nanotubes, nanorods, etc.) [35–38]. In addition, it is crucial to achieve separation and transfer of spatial charges from the catalyst surface to the reactants for CO_2 reduction. Nevertheless, photogenerated electrons and hole may recombine rapidly due to the coulombic attraction and the absence of charge trapping states on the surface of the catalyst, which would lower the charge separation efficiency and consequently hinder the reaction process. Therefore, a small proportion of separated charges will move toward the reactive sites located on the catalyst surface and will take part in the redox reaction, which involves the conversion of CO_2 and H_2O into diverse oxygenated and carbon-containing compounds. The resulting products are ultimately released from the surface of the semiconductor and separated. Apart from these issues, limitations such as insufficient capacity of active sites to adsorb CO_2 inhibit charge accumulation and CO_2 activation. Moreover, PCO_2RR to C_{2+} products are hindered by the relatively slower rate of electron transfer, along with the sluggish kinetics involved in the formation of carbon–carbon (C–C) bonds, which may lead to the release of *CO from the surface of the catalyst. The release of electrons occurs before *CO can effectively accept the subsequent electrons, which are necessary for its further reduction into C_{2+} hydrocarbon products. Therefore, the attainment of efficient synthesis of C_{2+} hydrocarbons in a photocatalytic system remains a significant challenge. It was reported that Cu_2O undergoes a preferential reduction to Cu^0 during the photocatalytic process, serving as the dominant Cu species involved in the CO_2 reduction reaction [39]. Furthermore, due to excellent electrical conductivity of Cu^0, it facilitates the accumulation of photogenerated electrons, thereby increasing the electron concentration. Additionally, the higher-energy electrons generated through localized surface plasmon resonance (LSPR) of Cu can activate the typically unreactive and stable chemical bonds present in CO_2. Nonetheless, despite the effectiveness of Cu^0 as an active site for photocatalytic CO_2 reduction and C–C coupling, the recombination of charge carriers on the semiconductor photocatalyst continues to hinder the accumulation of photogenerated electrons on the Cu^0 surface. This limitation ultimately leads to relatively low photocatalytic CO_2 reduction activity. Up

to the present time, addressing this challenge and effectively bridging the gap between the lower efficiency of multie-lectron transfer and the sluggish kinetics associated with *CO coupling remains a persistent challenge. Researchers continue to explore and develop strategies to improve the effectiveness of charge transfer and the kinetics of C–C bond formation such as metal/non-metal doping, cocatalyst deposition, heterojunction construction, etc.

2.1.2 Electrocatalytic CO_2 Reduction Reaction

ECO_2RR, which can be powered by renewable energy sources, is an effective way to achieve carbon neutrality. An electrocatalytic CO_2 reduction system typically operates in a three-electrode mode. Specifically, the working electrode and reference electrode are situated at the cathode, while the counter electrode is located at the anode. To isolate the half-reactions and enable ion migration, the two electrodes are separated by an ion exchange membrane. On the anode, H_2O molecules are oxidized to produce oxygen and protons, with oxygen being collected as a gas product and the protons traverse the membrane to reach the cathode. The CO_2 molecules that are present in the electrolyte are transported to the cathode surface through a combination of convection and diffusion. At the cathode, multiple steps of proton and electron transfer convert the CO_2 into desired products through reduction potential (Fig. 4). Nevertheless, CO_2 dissolved in the electrolytes has high ohmic and mass transfer resistance because of the distance between cathode and anode, while the cathode has limited CO_2 diffusion due to its low solubility. An often employed and advantageous electrolyte is an alkaline aqueous solution, primarily because it exhibits a lower overpotential when compared to its neutral counterpart. When various alkaline aqueous solutions

Fig. 4 Typical electrocatalytic CO_2 reduction system

were examined, it was noted that higher current densities were achieved with increasing solution concentrations [40]. Electrochemical impedance spectroscopy further revealed a reduction in cell resistance as a result of increased ionic conductivity with rising concentrations. In their study, Sinton et al. [41] observed a notable 240-mV positive shift of the onset potential when they employed a 10 M KOH electrolyte solution instead of a 1 M KOH solution.

In general, CO_2 solubility can be enhanced by employing organic solvents instead of aqueous solutions as electrolytes. Despite CO_2 being a nonpolar molecule, it exhibits considerable polarizability and can form hydrogen bonds with compatible donor solvents. The majority of organic electrolytes are polar solvents, which permits electrocatalytic CO_2 reduction over a broader potential range. In addition, using an aprotic solvent-like acetonitrile or dimethylformamide could promote the dimerization of *CO–CO, whereas the production of CH_4 is favored in a protic solvent. There has also been research exploring the use of ionic liquids, added to either aqueous or organic solvents, which exhibit good thermal stability, high CO_2 solubility, and high conductivity; nevertheless, their high cost and the possibility of cathodic corrosion are the challenges that should be considered.

In electrocatalytic CO_2 reduction experiments, some researchers have introduced gaseous CO_2 to the cathode, ensuring that an ample amount of CO_2 is delivered to the catalyst, even when operating at high current densities. Certain research teams have achieved noteworthy enhancements in the current density for CO_2 reduction to C_{2+} products by employing gas diffusion electrodes (GDEs) [42, 43]. Nonetheless, a notable challenge associated with GDE-type electrolyzers is their reliance on aqueous electrolytes for the collection of liquid products. The inclusion of these aqueous electrolytes can result in the dilution of the liquid products, leading to increased expenses in terms of product recovery and separation. To address the challenge posed by GDE-type reactors, several research groups have investigated the electrocatalytic CO_2 reduction in a zero-gap type electrolyzer, which eliminates the requirement for an aqueous electrolyte [44, 45]. For example, Lee et al. introduced an effective strategy called catholyte-free electrocatalytic CO_2 reduction (CF-CO_2R) and designed to circumvent solubility limitations by incorporating an appropriate amount of water vapor along with gaseous CO_2 as a cathode reactant [45]. In this CF-CO_2R electrolyzer, water vapor serves as a carrier, facilitating the supply of dissolved CO_2 to the cathode
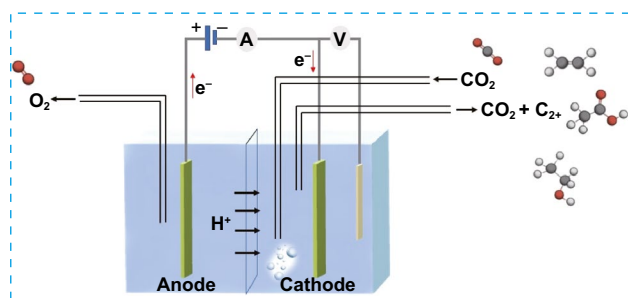
by creating a CO_2-saturated aqueous film on the catalyst surface. This approach offers the advantage of replenishing consumed CO_2 in the film directly from the bulk gas stream, thereby enhancing CO_2 mass transfer and improving reaction kinetics. However, it is noteworthy that this configuration only permits the detection of gas products. Therefore, it is crucial to carefully choose a suitable cellular arrangement based on the properties of the catalyst and the nature of the desired products.

In general, electrocatalytic systems have a more compact and flexible structure compared to photocatalytic systems. They also have higher catalytic efficiency due to the continuous transfer of electrons to the working electrode driven by an external bias. Nevertheless, the direct redox reaction on the electrode requires a higher overpotential, resulting in relatively high-energy consumption. Additionally, adjusting the strength and form of the external potential allows for easy control of the selectivity of products derived from CO_2 reduction. Meanwhile, the ECO_2RR process is not as favorable in aqueous electrolytic systems when compared to competing reactions like the hydrogen evolution reaction (HER) [46]. To improve the selectivity toward C_{2+} compounds, it is necessary to supress the HER pathway and reduce the rates of C_1 products. However, similar to the photocatalytic CO_2 reduction systems, the electrocatalytic CO_2 reduction mechanism is complex, and it results in the production of C_1 hydrocarbons, leading to selectivity issues. The diverse final products arising from this complicated pathway make it challenging to obtain the desired product with good selectivity [12, 14, 47].

2.2 The Pathway of CO_2 Reduction to C_{2+} Products over Cu-based Materials

2.2.1 CO_2 Adsorption/Activation and Different Models

To optimize the CO_2RR process for increased C_{2+} product formation, it is essential to understand the reaction intermediates and pathways that are involved. As is well known, the CO_2RR processes typically involve three main steps. The initial step entails the adsorption/activation of CO_2 on the surface of the catalyst, resulting in the production of CO_2^- anion radicals (Eq. 1 in Table 1). The second involves a sequence of complex reactions that are dependent on the transfer of e^-/H^+, leading to the production of precursors such as *CO,

*COH, and *CH$_2$, or effecting C–C coupling to produce C_{2+} chemicals as listed in Table 1 (Eqs. 2–11 in Table 1). Finally, in the third step, the formed products are desorbed from the surface of the catalyst. CO_2 is a highly stable molecule with a linear symmetry structure and its direct reduction in an aqueous solution to form CO_2^- anion radical through single-electron transfer process with a standard redox potential of -1.9 V versus NHE is thermodynamically unfavorable. Unlike the activation of CO_2 molecule over heterogeneous catalysts through surface atom interactions can effectively minimize the energy required to accept an electron by lowering the lowest unoccupied molecular orbital (LUMO) level of CO_2. This can be achieved through the alteration of the molecular properties, including the elongation of C–O bond length and bending of O–C–O angle [48–51]. Generally, the CO_2 adsorption/activation step to form CO_2^- anion radical is considered the rate-limiting step for CO_2RR process. As of now, several models for CO_2 adsorption on catalyst surfaces have been reported using different types of catalysts, including two main theories that focus on the use of either metals or metal oxides as catalysts [52–54]. At the molecular level, CO_2 activation occurs through a partial transfer of electrons into the LUMO, resulting in the generation of partially charged $CO_2^{\delta-}$ species [55, 56]. Based on metal catalysts, five configurations for CO_2 adsorption and activation were proposed as depicted in Fig. 5a. The structure of $CO_2^{\delta-}$ species varies according to the adsorption mode, namely, carbon coordination, oxygen coordination, and mixed (carbon/oxygen) coordination. Carbonate-like species ensue from the carbon binding mode wherein the carbon atom serves as electron acceptor for Lewis base centers. Dual bidentate species emerge through oxygen coordination, with two alternative structures. In this model, the oxygen atoms act as electron donor for surface Lewis acid centers owing to the pair electrons. Meanwhile, structures of both species occur in the mixed coordination mode. According to this model, CO_2 molecules serve as both an electron donor and acceptor by oxygen and carbon atoms, respectively.

As for the metal oxide surfaces, CO_2 activation can be accomplished by forming coordination bonds with adjacent metal sites, either through the carbon atom or the terminal oxygen atoms of the CO_2 molecule, resulting in the formation of monodentate or bidentate carbonate species (Fig. 5b) [48, 57]. The first two configurations show the formation of monodentate species, in which either the oxygen or carbon atom coordinates with a metal atom of the metal oxide by
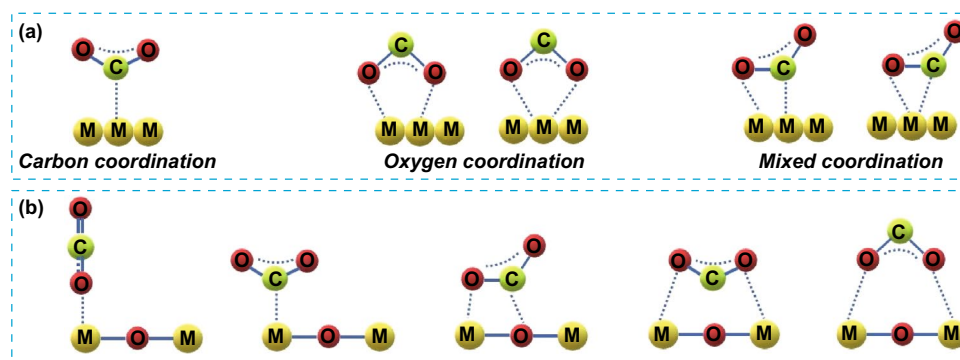
Fig. 5 The possible configurations of adsorbed CO_2 on: **a** metal catalysts and **b** metal oxide catalysts

forming M–O or M–C bonds. In the third configuration, the CO_2 molecule binds to the metal oxide surface through interactions between both oxygen with metal atom and carbon with oxygen atom of the metal oxide. The fourth configuration depicts a mixed oxygen/carbon coordination, resulting in a bridged carbonate geometry, in which two oxygen atoms bind with two metal atoms, and the carbon atom of CO_2 molecule points downward. The last configuration presents a bridging geometry through oxygen coordination, where two oxygen atoms interact with two metal atoms and the carbon atom points upward. These differed binding configurations might result in many intermediates, leading to various reaction pathways. This highlights the importance of understanding the CO_2 adsorption/activation steps in CO_2RR processes.

The surface structure of metal oxides plays a key role in CO_2 adsorption/activation process. Different structures may have different active sites and surface energies that can affect the strength of the interaction between CO_2 molecules and metal oxides. As example, the CO_2 adsorption on CuO oxide surfaces, namely, (0 1 1), (1 1 1), and (− 1 1 1), was notably strong only on the (0 1 1) surface. Conversely, a weak CO_2 adsorption was observed on CuO (1 1 1) and CuO (− 1 1 1) surfaces [58]. As reported in the literature, oxygen vacancies Vo could change the physico-chemical and electronic properties of metal oxides such as TiO_2 [59–61], CeO_2 [62], In_2O_3 [63], Zn_2GeO_4 [64], and Cu_2O [65, 66] leading to improved surface adsorption and the creation of additional active centers. Zheng and co-workers reported that copper oxide nanodendrites with partially reduced surfaces and abundant Vo (CuO_x–Vo) exhibited improved CO_2 adsorption and electroreduction abilities when compared to pure Cu and Vo-free CuO_x (Fig. 6a and b). The surface Vo has been

identified as effective Lewis base sites for the enhancement of CO_2 adsorption. Theoretical calculations showed that CuO_x–Vo provides strong binding affinities toward *COH and *CO intermediates, while displaying weak affinity toward *CH_2, resulting in efficient production of C_2H_4 with high Faradaic efficiencies reaching 63% (Fig. 6c–e). Moreover, it was demonstrated that the Faradaic efficiency for C_2H_4 production is greatly influenced by the density of Vo in CuO_x [67]. This highlighting the potential of controlling and engineering Vo defects to create more effective catalytic materials for CO_2 adsorption/activation and to adjust the selectivity toward desired products in CO_2RR. Aside from surface defects, the deposition of basic sites such as alkaline or alkali-earth metals on the catalyst surface can promote the CO_2 adsorption owing to the strong interaction with acidic CO_2 molecules. Also, increasing the catalyst's surface area could provide more active sites for CO_2 adsorption [68]. Furthermore, surface modification involving the addition of functional groups, such as hydroxyl (OH) or amino (NH_2) groups, has been observed to exert significant effects on the interaction between CO_2 and the surface, thereby improving its adsorption [69, 70].

2.2.2 The Pathway of CO_2 Reduction to C_{2+} Products

As illustrated in Table 1, the CO_2RR process includes a complex reaction mechanism, which gives rise to the production of multiple products. Consequently, obtaining the desired product becomes challenging due to selectivity concerns. The determination of the favored reaction pathway leading to the wanted product is intricately dependent on the adsorption energy of the intermediates at the active site
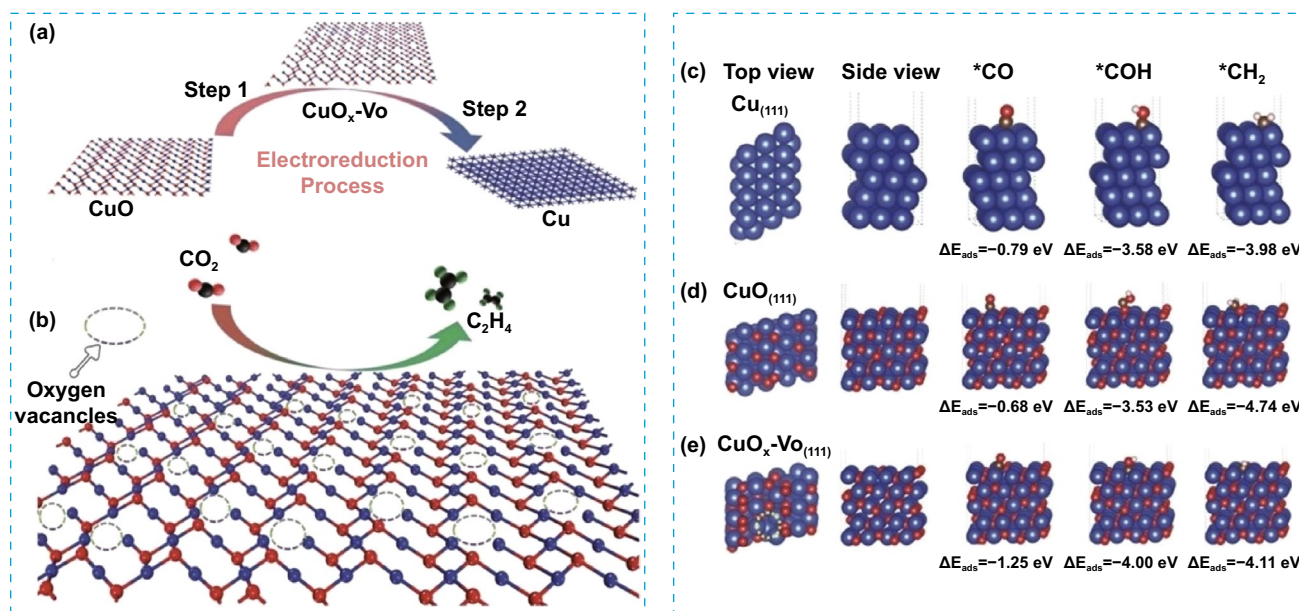
Fig. 6 **a** V_O-rich CuO_x surface via electrochemical control of oxygen vacancies. **b** Schematic illustration of ECO_2RR into C_2H_4 on Vo-rich CuO_x–Vo surface. DFT calculation results with three ECO_2RR intermediates (*CO, *COH, and *CH_2) of **c** pure Cu, **d** Vo-free CuO, and **e** CuO_x–Vo. Reproduced with permission [67]. Copyright 2018, Wiley–VCH

of the catalyst. As an example, the formation of HCOOH from the key intermediate *OCHO or *COOH depends on the type of adsorption model type resulted from the hydrogenation of the CO_2^- anion radical adsorbed onto the catalyst surface [71]. As shown in Fig. 5, *COOH is also a key intermediate in the generation of *CO, which subsequently undergoes desorption to yield the gaseous product CO [72]. The formation of C_{2+} chemicals requires the exchange of a greater number of electrons in comparison with C_1 products, and the subsequent coupling of C–C bonds is deemed to be the step that governs the reaction rate, making this process difficult to occur kinetically. *CO is a key intermediate as it plays a significant role in the C–C coupling reaction, which leads to the generation of C_{2+} products [7, 73]. It has been reported that *COCHO plays a crucial role as an intermediate in the production of C_{2+} products, which may be formed through various coupling reactions, such as the coupling of CO and *CHO (*CHO + CO → *COCHO), the coupling of CO and *COH (*COH + CO → *COCOH), or coupling *CO (*COCO + H^+ → *COCHO) [73, 74]. Compared to *COCOH, the *COCHO intermediate is more stable as it lacks a double bond to the active site or a free radical on the carbon atom. As illustrated in Fig. 7, the ethylene pathway involves the hydrogenation of *COCHO to

*COCHOH, followed by its conversion to *OCH_2COH. This ultimately yields both and ethylene (C_2H_4) and acetic acid (CH_3COOH). In the ethanol pathway, the reaction mechanism involves the conversion of *COCHO to glyoxal ($C_2H_2O_2$) through a one-step hydrogenation process. This glyoxal can be further transformed into either acetaldehyde (CH_3CHO) or ethanol (CH_3CH_2OH) based on the potential applied to the reaction. A lower potential favors the production of acetaldehyde, whereas at higher potential, the reaction yields ethanol [74, 75]. Furthermore, it is possible to form ethylene, ethane, ethanol, and acetaldehyde products through the carbene route, which entails the generation of CO* as a major intermediate compound. The CO intermediate is subsequently fully reduced to "C" and further reduced to form $CH_2^·$ and $CH_3^·$ radicals. If the photocatalyst surface can stabilize the $CH_2^·$ and $CH_3^·$ radicals, then they are more likely to couple and form C_{2+} products. However, if the surface cannot stabilize these radicals, then they will desorb as methane.

A reaction pathway involving the coupling of three carbon atoms is required for the production of C_3 products. García et al. utilized DFT calculations to conduct an in-depth analysis of the mechanism involved in CO_2 conversion to C_3 products. According to their study, C_3 products are

Fig. 7 General pathways for CO_2 reduction reactions. Reproduced with permission [22]. Copyright 2023, Wiley–VCH

formed by combining C_2 and C_1 intermediates [76]. These interactions might occur between C_1 (CH_xO^*, CH_x^*), and C_2 intermediates, which may include hydrocarbons ($CH_yCH_z^*$) or oxygenates ($CH_yOCH_zO^*$, $CH_yOCH_z^*$, and $CH_yCH_zO^*$). However, the current selectivity for C_3 products is still low. Thus, further investigations of the reaction pathways are needed design effective catalysts that can promote the formation of C_3 products.

While numerous reaction pathways have been confirmed by theoretical and experimental approaches, the actual CO_2RR processes are influenced by many factors, and the products selectivity is more complex. In the case of PCO_2RR process, the selectivity to C_{2+} is particularly intricate and largely influenced by the photoinduced e^-/h^+ density as well as the stability of the generated intermediates. The C_1 products are rapidly generated as the intermediate can easily combine with hydrogen atoms, while the opposite charge of intermediates can obstruct the C–C coupling steps. On the other hand, several factors significantly influence the ECO_2RR process's selectivity, including operating conditions, which consist of the electrolyte pH, the type of electrolyte cation/anion, and the applied overpotential [74]. In addition, both systems can be influenced by the catalyst surface properties. These properties, including surface adsorbates, defects, structure, morphology, and facets, can substantially alter the adsorption energies of critical intermediates as well as the kinetic barriers of reactions, resulting in different reaction routes [77]. Despite the fact that PCO_2RR and

ECO_2RR have certain distinctions, their practical implementation is hampered by comparable hurdles and comparable strategies aimed at increasing the efficiency and the C_{2+} products selectivity as well as the stability may be used in both systems to overcome the challenges.

3 Fine-Tuning Surface Structure of Cu-Based Catalysts for Improving the Activity/Selectivity of CO_2RR Toward C_{2+} Compounds

3.1 Photocatalytic CO_2 Reduction Reaction

Despite the potential of PCO_2RR as a promising and sustainable approach to synthesize C_{2+} compounds, the current literature points out a relatively low efficiency and selectivity of this process in C_{2+} product formation [78, 79]. This is due to limitations on light absorption, rapid charge carriers recombination that results in low electron concentrations on the photocatalyst's surface, high kinetic barriers, as well as desorption of C_1 intermediates. It is well known that Cu-based photocatalysts are effective at multi-electron transfer and can make use of weakly bound d-band electrons. They also have a short bandgap, allowing them produce sufficient charges through the absorption of sunlight within the range of visible light. Moreover, their strong CO_2 adsorption and their ability to effectively stabilize the reaction intermediates

contribute to their potential for C_{2+} product generation. Nonetheless, the development of Cu-based photocatalysts that are highly efficient and selective in generating C_{2+} products remains a significant challenge. Researchers have been exploring different approaches such as crystal phase/morphology optimization, metal doping, defect engineering, heterostructure fabrication, and bimetallic synergies to enhance the activity/selectivity of PCO_2RR toward C_{2+} compounds; nevertheless, there is still debate surrounding the origin of C_{2+} selectivity enhancement. In this section, we provide basic comprehension and discussions on these strategies to help with further enhancement of the activity/selectivity toward C_{2+} compounds in PCO_2RR. To attain a more comprehensive understanding of the structure–activity–selectivity relationships, we have categorized Cu-based photocatalysts into four groups: Cu oxides/sulfides, Cu alloys, Cu-based single-atom catalysts (Cu SACs), and Cu-based heterojunctions.

3.1.1 Cu Oxides/Sulfides

Copper oxide photocatalysts are *p*-type semiconductors with narrow bandgap energy and elevated conduction band values enabling them to convert CO_2 into various hydrocarbons [80–82]. However, the high charge recombination rate and the poor stability of Cu oxides result in a low efficiency of photocatalytic CO_2 reduction [83]. The nano-level structural modification has been widely adopted for Cu oxides to overcome these drawbacks. Xue et al. prepared a dendritic 3D porous Cu_2O structure via a method involving electrodeposition as well as a subsequent thermal oxidation [84]. The findings indicated that the 3D porous Cu_2O exhibited highly effective photocatalytic performance, with a CO yield of 26.8 μmol g^{-1} h^{-1}, which was 24 times greater than the CO yield obtained from the non-porous Cu_2O structure. The 3D porous Cu_2O with nano-sized dendrite structure was demonstrated to promote the separation of charge carriers and transport efficiency as well as the overall mass transfer efficiency of CO_2 gas, boosting the photoreduction of CO_2 and the anti-photocorrosion properties. Importantly, CH_4 and C_2H_4 products were observed for the 3D porous structure, owing to longer retention time of gas adsorption, as well as abundant active sites and high electron transfer rate offered by the porous structure. The conversion pathways of CO_2 to CO, CH_4, and C_2H_4 products are depicted in Fig. 8a. The

formation of *COOH intermediates occurred initially from CO_2 reduction, which further resulted in the generation of *CO intermediates upon dehydration. The *CO intermediates desorb rapidly to generate CO products, while longer *CO adsorption time favors the production of CH_4 and C_2H_4 compounds. Thus, the distribution of the final product depends on the stability of the *CO intermediate. The absorption of *CO intermediates was facilitated by the presence of Cu^+ species, which further undergo C–C coupling steps to produce C_2H_4 product. This work provided insight for studying the morphology control effect for PCO_2RR.

Another strategy for adjusting the C_{2+} product selectivity of CO_2 reduction is crystal phase control. Recently, Wang et al. demonstrated through DFT calculations that the conversion of CO_2 into ethanol (C_2H_5OH) can be efficiently achieved by both 2D β-phase Cu_2S bilayer and δ-phase Cu_2S monolayers [85]. Figure 8b and c illustrates the free energy profiles of CO_2 reduction on δ-Cu_2S and β-Cu_2S. Two different pathways were examined, namely, CO_2–COOH*–CO* and CO_2–HCOO*–HCOOH*. Based on the results, the CO* intermediate was more likely to be stabilized on both surfaces. This occurred because the CO_2–COOH* route has a lower energy barrier than the HCOO*–HCOOH* pathway. Specifically, the energy barrier for CO_2–COOH* pathway was 0.21 eV on δ-Cu_2S and 0.08 eV on β-Cu_2S, while the energy barrier for HCOO*–HCOOH* pathway was 0.46 eV on δ-Cu_2S and 0.43 eV on β-Cu_2S. The results of Bader charge analysis show a significant charge transfer between Cu and S atoms on the surface resulting in the generation of Cu^+ sites. This led to the adsorption of CO* and the subsequent coupling of CO* and formyl (CHO*) species, as illustrated in Fig. 8d. Notably, the kinetic barriers associated with CO*–CHO* coupling have been determined to be 0.3 eV, confirming the possibility of CO_2 to C_2H_5OH conversion. These findings offer important theoretical insights for future experimental development and synthesis of photocatalysts aiming at producing C_{2+} products from CO_2.

3.1.2 Cu Alloys

Recent studies have reported that Cu alloys have superior photocatalytic properties compared to single Cu catalysts [15, 37, 86–89]. The use of Cu alloys can improve the CO_2 activation and optimize the binding strength of the key intermediates on catalysts surface, which ultimately promotes
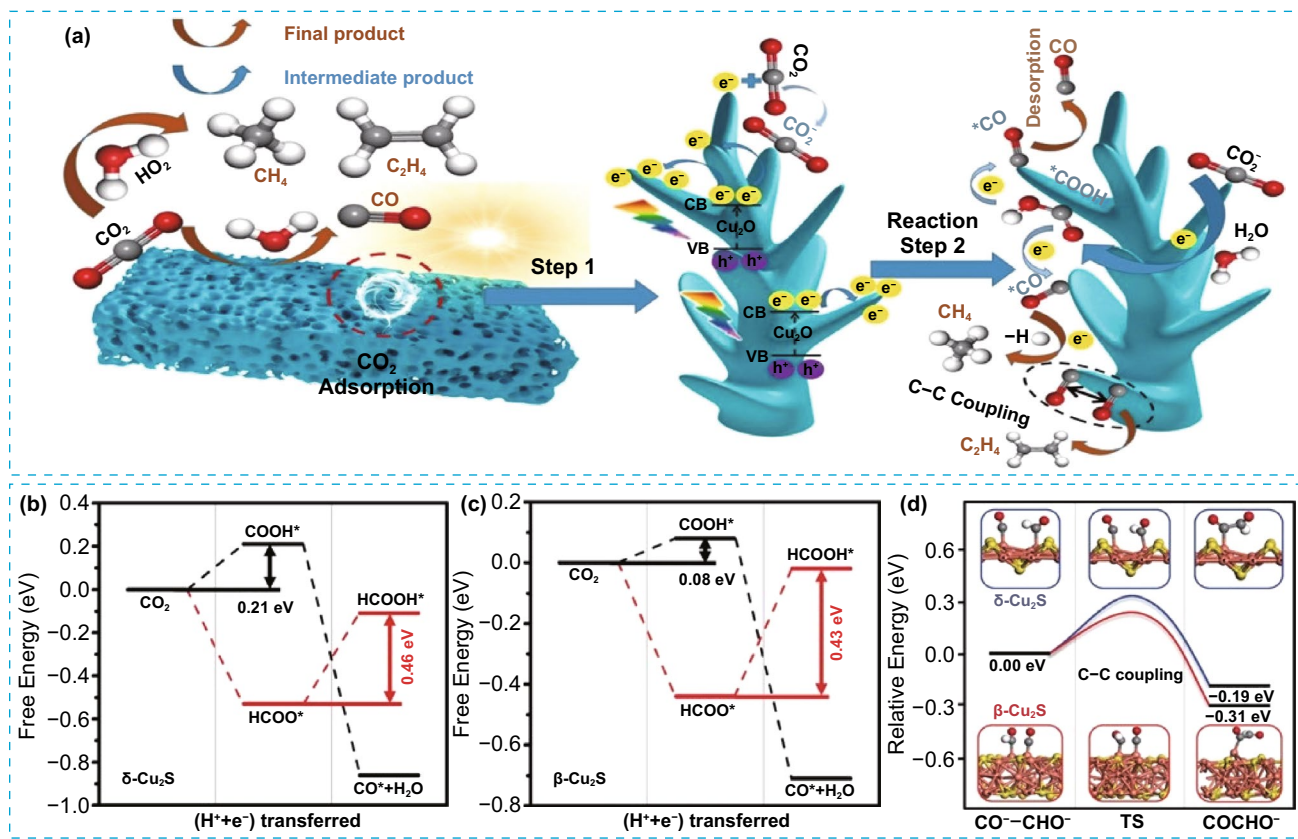
Fig. 8 a Schematic illustration of CO_2 photoreduction mechanism on 3D porous Cu_2O. Reproduced with permission [84]. Copyright 2022, Elsevier. The free energy profiles of CO_2 reduction to CO* and HCOOH* on **b** δ-Cu_2S, **c** β-Cu_2S and **d** relative energy diagram of the CHO*–CO* coupling on δ-Cu_2S and β-Cu_2S. Cu, orange; S, yellow; C, gray; O, red; and H, white. Reproduced with permission [85]. Copyright 2021, The Royal Society of Chemistry

the efficient formation of C_{2+} chemicals via C–C coupling. Therefore, by altering the catalyst composition, the reaction mechanism can be fine-tuned and tailored to C_{2+} production. For instance, Shankar et al. synthesized Pt–Cu alloys supported on TiO_2 nanotubes for photocatalytic CO_2 reduction. The hydrocarbon production rate was maximized over $Cu_{0.33}$–$Pt_{0.67}$/TiO_2 photocatalyst, and CH_4, C_2H_4, and C_2H_6 products were obtained at rates of 2.60, 0.33, and 0.47 mL g^{-1} h^{-1}, respectively. Whereas, the monometallic Cu/TiO_2 or Pt/TiO_2 catalysts and the other Cu–Pt compositions resulted in limited C_{2+} formation, with CH_4 being the major reaction product [37]. This is possibly attributed to the ability of Pt to boost the photocatalytic reduction rates and the role of Cu in promoting the C_{2+} products selectivity owing to the higher reactivity and strong adsorption of CO on copper surface. This finding underscores the importance of carefully controlling the composition of the photocatalyst to tune the selectivity toward C_{2+} products. In et al. observed

a shift in selectivity from CH_4 to C_2H_6 by CO_2 photoreduction under artificial sunlight (AM1.5) using bimetallic Cu–Pt alloys deposited reduced blue titania (Cu–Pt/BT) catalysts. The enhanced C_2H_6 selectivity was attributed to the effective transfer of high density of electrons from BT to Cu nanoparticles through Pt, along with the high concentration of stabilized $CH_3^{.}$ intermediates [78]. The formation of C_2H_6 product occurs through the reaction of two $CH_3^{.}$ radicals via a self-reaction process.

Apart from the previously mentioned limitations regarding the production of C_{2+} compounds during photocatalytic CO_2 reduction, the repulsion between reaction intermediates generated during the process also impede C–C coupling reaction required for the generation of C_{2+} compounds. To minimize the inter-adsorbate repulsive forces, one can establish nearby reaction sites with opposing charges. In this regard, Shankar et al. synthesized large-sized AgCu nanoparticles supported on TiO_2 nanotube array (AgCu-TNTA)

[15]. The obtained photocatalyst exhibited total rate of hydrocarbon production ($CH_4 + C_2H_6$) of 23.88 µmol g^{-1} h^{-1} with C_2H_6 selectivity of 60.7%. In comparison, the Ag-TNTA and Cu-TNTA catalysts showed C_2H_6 selectivity of 15.9% and 10%, respectively, indicating that the presence of both Ag and Cu in the AgCu bimetallic alloy resulted in a synergistic effect, enhancing the production of C_2H_6 in PCO_2RR process. The synergistic effect was related to the multipolar resonances in large plasmonic AgCu nanoparticles, which enabled the creation of active sites with opposite charges, thus reducing the repulsion between reaction intermediates. Additionally, the stabilization of $CH_3^{\cdot}$ radicals was observed due to the ability of both Ag and Cu to stabilize radicals through the promotion of C–C coupling on their surfaces. This occurred through charge transfer, where plasmonic electrons were injected into the TNTAs, leaving behind holes that gave the metals a positive charge. This positive charge increased the lifespan of $CH_3^{\cdot}$ radicals. Moreover, the researchers noted that a high concentration of hot spots, where the electric field is particularly strong, may increase the polarization of CO_2 molecules and promote the production of C_{2+} compounds.

Numerous studies reported that defect engineering played an important role in governing both the interface electronic structure and active sites of catalysts. This, in turn, can significantly impact the photocatalytic process [90–92]. For instance, Yu et al. fabricated a 2D ultra-thin $CuGaS_2/Ga_2S_3$ (CGS/GS) with S vacancy, which showed unprecedented selectivity toward C_2H_4 ($\approx$93.87%) with a production rate of 335.67 µmol g^{-1} h^{-1} [93]. They found that the mechanism for the multi proton–electron pathway of CO_2 reduction reaction is altered by the existence of S vacancy. This occurs because S vacancy triggers a highly delocalized electron distribution, leading to a local metallization between Cu and Ga in the vicinity of the S vacancy and resulting in the formation of Cu–Ga metallic bond (Fig. 9a and b). These bimetallic Cu–Ga dual sites could facilitate the C–C coupling and stabilize the formed intermediates, thereby lowering the energy barrier for C_2H_4 formation. Also, they noted that the photocatalysts' selectivity is dependent on the Cu oxidation state. As shown in Fig. 9c, the increase in Cu^+/Cu^{2+} ratio resulted in an increase in C_2H_4 yield and selectivity owing to the improved thermodynamics of *CO dimerization by Cu^+ species. However, when the Cu^+/Cu^{2+} ratio exceeded 2, the yield and selectivity of C_2H_4 decreased significantly, which was attributed to insufficient Cu^{2+}, resulting in a notable

reduction in the adsorption capacity of *CO intermediate. In other words, the catalyst surface underwent a charge distribution rearrangement as a result of introducing S vacancies, which dominantly affects the chemical state of Cu ions. These effects are likely to be beneficial for the production of C_{2+} compounds. The reaction mechanism has been investigated by in situ Fourier transform infrared spectroscopy (FTIR). Figure 9d shows the presence of signals relative to *COOH, *CO, and *OCCHOH intermediates, indicating that *OCCHOH was a key intermediate of coupling of C–C for C_2H_4 formation. The DFT results reveal that *COOH intermediates were generated from CO_2 reduction, which subsequently underwent coupling with H^+/e^- pairs to yield CO molecules. Eventually, *CO intermediates transform into C_2H_4 through complex processes involving electron and proton transfer (Fig. 9e–i). In addition, the formation of *CHOHCO by coupling *CO and *CHOH appears to be the most thermodynamically favorable pathway for C–C bonding formation when compared to other pathways (Fig. 9j). This study uncovered a novel approach to optimize the geometric distance of reactive sites through vacancy engineering for increasing the efficiency/selectivity of CO_2 photoreduction into C_{2+} products.

3.1.3 Cu SACs

Single-atom catalysts (SACs) have become a prominent area of research as they allow the utilization of almost all active metal sites [94–97]. To achieve this, metal particles are reduced in size and aggregation to form individual atoms with low coordination states. This leads to single-atom SAs having exclusive electronic properties that distinguish them from corresponding bulk materials [98, 99]. For PCO_2RR, metal SAs doping into substrates has been studied extensively to alter photocatalysts properties. Metal ions can act as hole trappers which, in turn, facilitate water oxidation and produce a significant amount of protons that can form specific C_1 intermediates. This can promote the C–C coupling and help in regulating the selectivity toward C_{2+} compounds by altering pathway the CO_2 photoreduction pathway [100–107].

For instance, Cu-doped semiconductors such as TiO_2 and g-C_3N_4 have been employed as catalysts for PCO_2RR. Huang et al. synthesized a catalyst composed of Cu–N_4 sites supported by phosphorus-modulated g-C_3N_4, denoted as
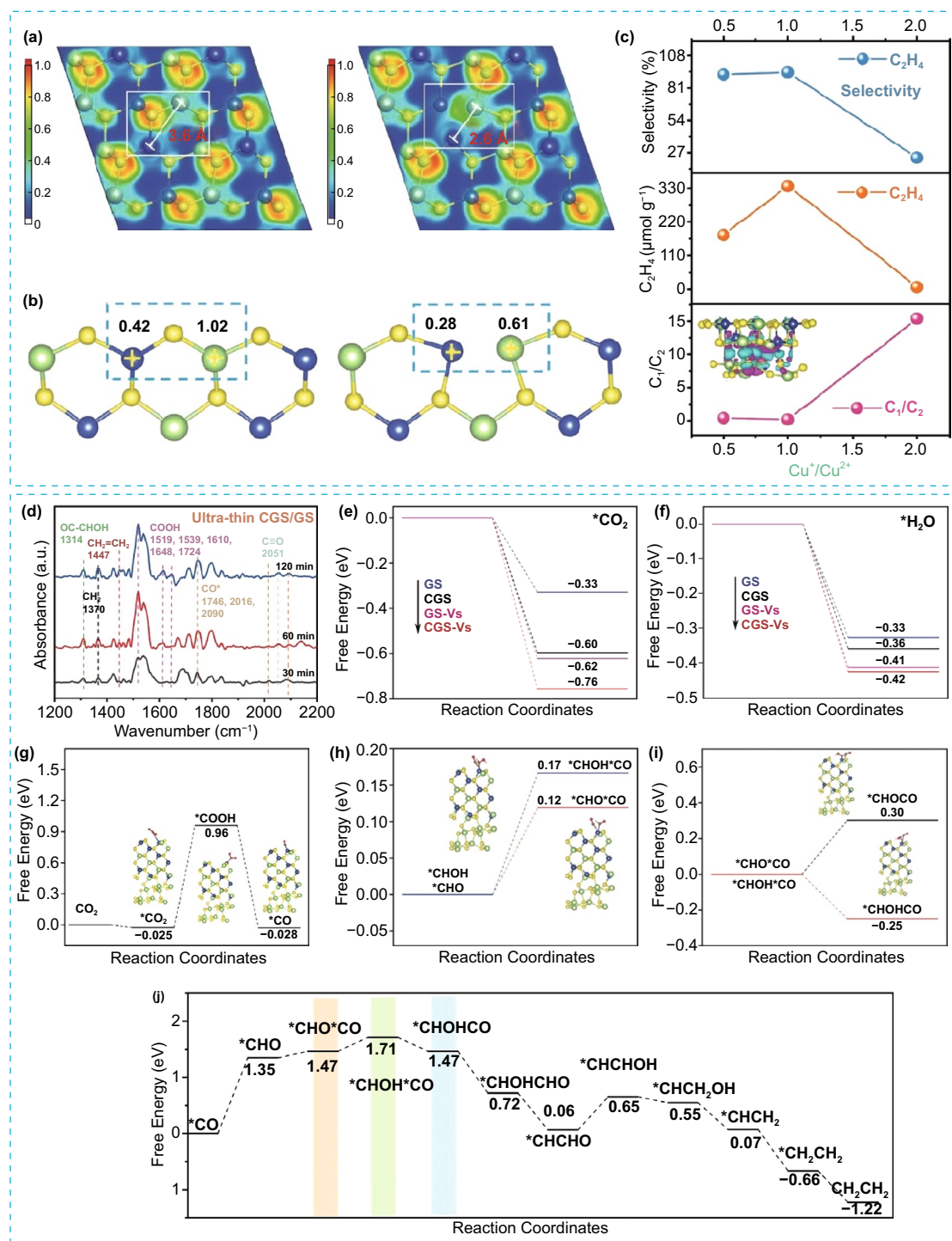
Fig. 9 **a** ELF of CGS/GS (Left) and ultra-thin CGS/GS with S vacancy (Right). **b** The calculated Bader charge of CGS/GS (Left) and ultra-thin CGS/GS with S vacancy (Right). **c** The correlation of C_1/C_2, C_2H_4, and selectivity with Cu^+/Cu^{2+}, **d** in situ FTIR spectra on ultra-thin CGS/GS. **e** Free energy of CO_2 on different active sites. **f** Free energy of H_2O on different active sites. **g** Free energy of CO_2 photoreduction to CO. **h**, **i** Free energy of different intermediates. **j** Schematic diagram of CO_2RR. Reproduced with permission [93]. Copyright 2023, Wiley–VCH

CuACs/PCN. The CuACs/PCN photocatalyst exhibited high efficiency in producing C_2H_4, demonstrating a selectivity of 53.2% and a yield rate of 30.51 μmol g^{-1}. Experimental and theoretical investigations revealed that C–C coupling intermediates could be formed on Cu–N_4 sites, and the presence of P in the surrounding microenvironment of CuACs/PCN lowered the energy levels of intermediate reactions [100]. It was found that CuACs/PCN exhibited lower energy barrier in almost all of the stepwise reactions, indicating the significant role played by P in enhancing C_2H_4 product selectivity. This research study emphasizes the importance of fine-tuning the coordination environment and the surrounding microenvironment of Cu SAs for the efficient formation of C_2H_4. Moreover, it provides a promising strategy that could be utilized to achieve selective C_2H_4 production in photocatalytic systems. Wang et al. conducted a study where they integrated Cu SAs into a UiO-66-NH_2 support for PCO_2RR [101]. They found that the Cu SAs and UiO-66-NH_2 interact through the –NH_2 groups. The resulting catalyst has the ability to transform CO_2 into liquid-phase products, including CH_3OH at a rate of 5.33 μmol h^{-1} g^{-1} and C_2H_5OH at a rate of 4.22 μmol h^{-1} g^{-1}. According to DFT calculations, the integration of Cu SAs resulted in a downshift of the HOMO and LUMO energy levels of UiO-66-NH_2, resulting in a narrowed bandgap of the catalyst. Moreover, the Fermi level of Cu/UiO-66-NH_2 was lower than the LUMO level of UiO-66-NH_2, which enhances the electron transfer efficiency. By comparing the partial density of states (PDOS) of UiO-66-NH_2 and Cu/UiO-66-NH_2, it was found that the introduction of Cu single atoms can decrease the bandgap of UiO-66-NH_2 by shifting its CBM to the Fermi level, which explain the C_{2+} products formation over Cu/UiO-66-NH_2.

Recent research suggested that bimetallic SACs exhibit superior photocatalytic performance compared to monometallic SACs for PCO_2RR. This is can be attributed to the synergistic effect between the two metals, which promotes the activation of CO_2 and stabilizes the reaction intermediates, thereby promoting the C–C coupling process that ultimately leads to the generation of C_{2+} products [102–104]. In this regard, Huang et al. developed a tandem photocatalysis strategy by combining rhenium-(I) bipyridine fac-[Re^I(bpy)(CO)$_3$Cl] (Re-bpy) and copper-porphyrinic triazine framework [PTF(Cu)] to create synergistic dual sites [91]. Under visible light irradiation, this approach effectively generated C_2H_4 at a rate of 73.2 μmol g^{-1} h^{-1}. However, using only Re-bpy or PTF(Cu) catalysts resulted in generation of CO under similar conditions, and C_2H_4 could not be obtained. The tandem photocatalytic system allowed for the CO produced at the Re-bpy sites to be adsorbed by neighboring Cu SAs in PTF(Cu), leading to a synergistic C–C coupling process that resulted in C_2H_4 formation. Liu et al. used MIL-125(Ti) metal organic framework as a precursor and template to create a cake like porous TiO_2 with doping of Cu and Co. Results showed that after 3 h of simulated sunlight irradiation in water vapor, CO and CH_4 were the main products for both pure TiO_2 and 1%Cu/TiO_2 photocatalysts [103]. The activity of 1%Cu/TiO_2 catalyst was observed to be superior to that of pure TiO_2, which can be ascribed to the reduction in the bandgap, thereby facilitating the separation of photoinduced charge carriers. Meanwhile, the introduction of trace Co ions through doping resulted in a shift of main products from CO and CH_4 to C_2H_6, with a small amount of C_3H_8 also detected. The results showed $CH_3^.$ radical enrichment over Co–Cu/TiO_2 in comparison with Cu/TiO_2 sample. Thus, doping with Co ions led to a substantial enhancement in the selectivity of C_{2+} products. It is noteworthy that the Co/TiO_2 photocatalyst did not produce any C_2H_6, indicating that the cooping of Cu and Co in the catalyst was responsible for the formation of C_{2+} products. Guo et al. conducted a study wherein they synthesized a photocatalyst composed of polymeric carbon nitride anchored with atomically dispersed Cu and In metals, referred to as InCu/PCN. The samples were synthesized by thermal polymerization method starting from mixed "$CuCl_2$ + urea + In-MOF" precursor as illustrated in Fig. 10a [104]. The findings from the SEM and STEM analyses indicated that the InCu/PCN composed of Cu and In atoms that are uniformly dispersed at the atomic level on PCN nanosheets. Additionally, the results revealed the presence of distinctively paired In-Cu configurations (Fig. 10b–d). Interestingly, a remarkable ethanol production rate of 28.5 μmol g^{-1} h^{-1} with a high selectivity of 92% was achieved by InCu/PCN photocatalyst, which is 2.4 times greater than that by Cu/PCN (Fig. 10e–g). The theoretical and experimental results indicated that the interaction between In and Cu serves to improve the separation of charges by accelerating the transfer of charges from PCN to the metallic sites. Additionally, the existence of Cu–N–In bonds allowed In to transfer electrons to Cu sites, resulting in a higher electron density at the copper active sites. The interaction between Cu and In atoms also enhanced the adsorption of *CO intermediates and reduced the energy required for C–C coupling. The improved selectivity toward
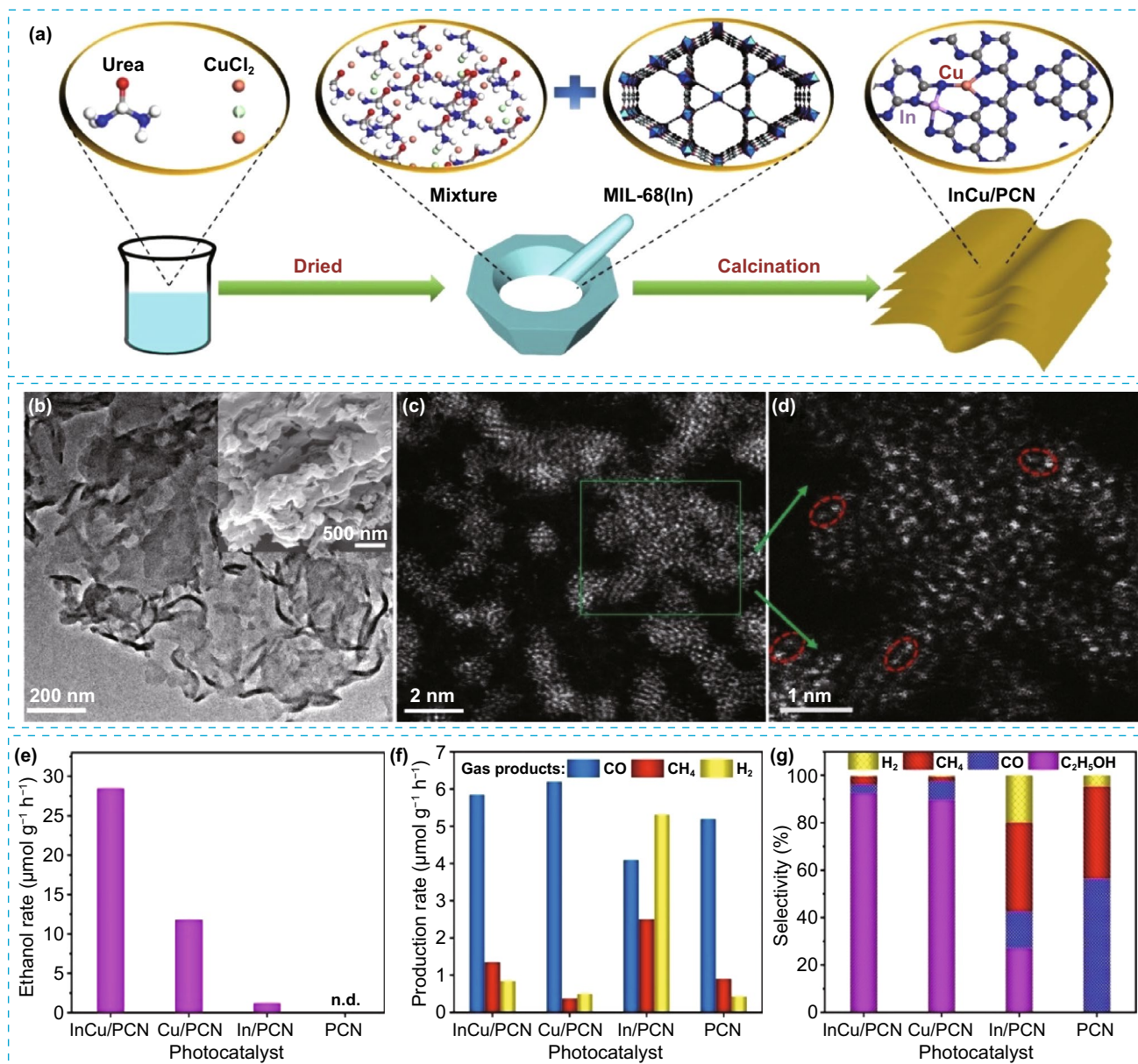
Fig. 10 **a** Schematic illustration of the synthetic process of InCu/PCN, **b** TEM image with SEM image inset of InCu/PCN sample, **c, d** AC-HAADF-STEM images of InCu/PCN, CO_2 photoreduction over InCu/PCN, Cu/PCN, In/PCN, and PCN, **e** ethanol production rate, **f** gas products generation rate, and **g** product selectivity. Reproduced with permission [104]. Copyright 2022, Wiley–VCH

C_{2+} products in CO_2 reduction reaction can be attributed to the synergistic effects of In–Cu dual-metal sites.

The strong metal–support interaction can enhance the dispersity and stability of SAs, thus leading to better performance of photocatalysis [108–110]. With this thought in view, Li et al. have synthesized $Cu^{\delta+}$ sites atomically dispersed on a CeO_2–TiO_2 support comprising of widely dispersed CeO_2 nanoparticles on a porous TiO_2 substrate

via the pyrolysis of a metal–organic framework (MIL-125-NH_2) impregnated with Cu^{2+} and Ce^{3+} ions (Fig. 11a). The obtained catalyst displayed increased activity toward CO_2 reduction to C_2H_4 under simulated sunlight with production rate of 4.51 µmol g^{-1} h^{-1} and 47.5% selectivity, which are 2.36 and 1.32 times those over the $Cu^{\delta+}$/TiO_2 sample (Fig. 11b) [105]. In situ FTIR presented the characteristic spectral peaks of *COOH, *CO, and *COCO groups
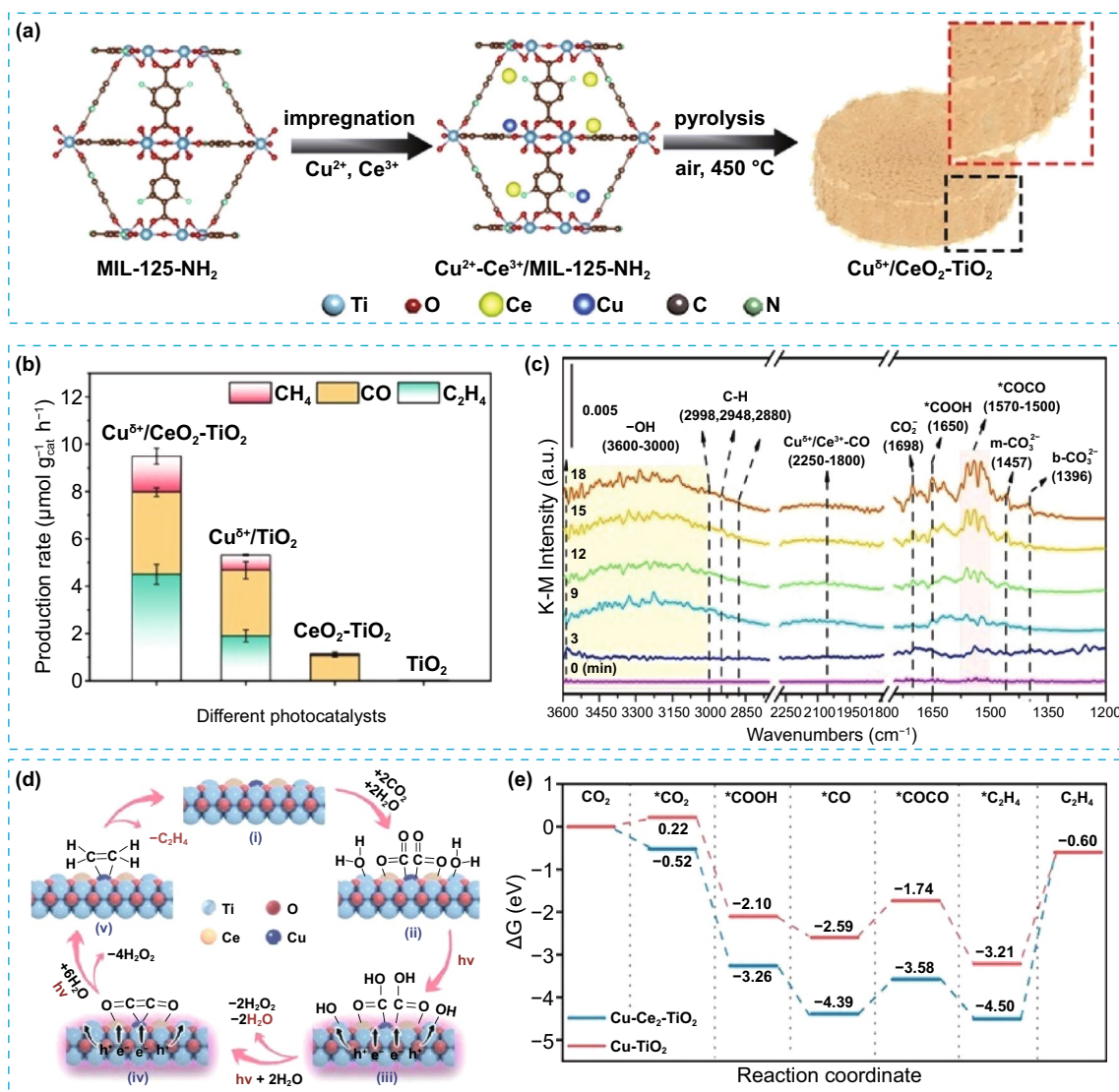
Fig. 11 **a** Schematic illustration of the steps for $Cu^{\delta+}/CeO_2$-TiO_2 preparation, **b** production rates over different photocatalysts, **c** in situ DRIFTS spectra of $Cu^{\delta+}/CeO_2$–TiO_2 photocatalyst, **d** proposed reaction pathway for CO_2 photoreduction to C_2H_4, and **e** calculated free energy diagrams for CO_2 reduction over Cu-TiO_2 and Cu–Ce_2–TiO_2 slabs. Reproduced with permission [105]. Copyright 2022, American Chemical Society

(Fig. 11c), suggesting that the CO_2 reduction pathway for producing C_2H_4 on $Cu^{\delta+}/CeO_2$–TiO_2 photocatalyst involved $CO_2 \rightarrow *CO_2 \rightarrow *COOH \rightarrow *CO \rightarrow *COCO \rightarrow C_2H_4$ (Fig. 11d). In addition, according to the Gibbs free energy calculations, the whole process of CO_2-to-C_2H_4 conversion on $Cu^{\delta+}/CeO_2$–TiO_2 catalyst is more thermodynamically favorable than on Cu/TiO_2, as shown in Fig. 11e. This is due to the presence of Cu–Ce dual active sites, which enables the efficient generation of key intermediate *CO and support the $*CO \rightarrow *COCO$ coupling reaction. This demonstrated a synergistic effect between the active sites of Cu

and Ce, which optimize the rate-limiting steps and enhance the overall CO_2-to-C_2H_4 conversion. More recently, Wang et al. conducted a study exploring how the valence state and coordination environment of SAs active sites affect the C_{2+} products selectivity using 2D WO_3 catalyst modified by depositing SAs Cu and Pt (CuPt/WO_3). The CuPt/WO_3 photocatalyst was found to be much more efficient than pristine 2D WO_3, Cu/WO_3, and Pt/WO_3 in producing acetic acid (CH_3COOH), with a production rate of 19.41 µmol g^{-1} h^{-1} and a selectivity of 88.1%. It has been demonstrated that stabilization of Cu^+ species by forming a coordinated complex

with Cl in aqueous solution is the key to attain superior efficiency and selectivity toward C_{2+} products [106]. All the components in CuPt/WO_3 photocatalyst work synergistically toward the production of C_{2+} products. Cu^+ species coordinated with Cl enhanced the CO adsorption capacity and increased the lifespan of CO* intermediate, both of which aid in the C–C coupling reaction. On the other side, SAs Pt active sites located in close proximity provided protons for the hydrogenation of CO* intermediate, ultimately leading to the formation of C_{2+} products.

Based on the amount of studies published on photocatalytic CO_2 reduction to C_2 vs C_3 products, it is obvious that direct conversion of CO_2 into C_3 products is much more difficult [107, 111]. This is due to the fact that the process requires a higher-order reaction pathway involving the creation of multiple C–C bonds. This, in turn, necessitates the integration of two distinct catalytic steps of CO_2-to-CO and CO-to-C_{2+} at different active sites [112–114]. Creating these C–C bonds is particularly challenging as it involves energy-intensive endothermic reactions with significant uphill energy barriers, primarily due to the high-energy levels of the critical $*C_2$ and $*C_3$ intermediates. This is mainly due to the lack of efficient catalytic active sites to stabilize these intermediates and reduce energy barriers. To address this concern, Xiong et al. recently developed an efficient photocatalyst for the direct CO_2 conversion into C_3H_8 [107]. The catalyst consisting of Cu SAs implanted on $Ti_{0.91}O_2$ atomically thin single layers (Cu–Ti–V_O/$Ti_{0.91}O_2$-SL), which showed superior efficiency toward CO_2 photoreduction to C_{2+} products with high selectivity of 50.2% for C_{2+} products and 32.4% for C_3H_8 as shown in Fig. 12a–c. As a comparative experiment, on Cu–O/$Ti_{0.91}O_2$–SL without V_O only showed the detection of CO and CH_4, while $Ti_{0.91}O_2$–SL showed mainly CO_2 reduction to CO product. Notably, the presence of V_O resulted in a strong coordination interaction between Cu SAs and neighboring Ti atoms, leading to high electron accumulation at copper sites and electron depletion at Ti sites. Conversely, Cu–O/$Ti_{0.91}O_2$–SL catalyst exhibited isolated single-metal structures with minimal interactions between Cu SAs and Ti atoms. In situ DRIFTS analysis confirmed the generation of the intermediate species (*COOH, *CO, *CHO, and *CHOCO) on Cu–Ti–V_O/$Ti_{0.91}O_2$–SL catalyst (Fig. 12d). DFT calculations showed that the pristine $Ti_{0.91}O_2$–SL *CO exhibited a high CO selectivity due to the facile desorption of *CO rather than undergo subsequent hydrogenation or C–C coupling (Fig. 12e). Moreover,

C–C coupling on the Cu–O site in the absence of Vos was challenging because of the high uphill energy changes, with hydrogenation of *CO into CH_4 being more favorable (Fig. 10f). Figure 10g shows the possible pathway of obtaining C_3H_8 product Cu–Ti–V_O unit. The initial step involved the transformation of absorbed CO_2 to *CHO via *COOH and *CO intermediates. Next, *CHO at Cu–Ti–V_O unit could react with CO coming from adjacent $Ti_{0.91}O_2$ units, resulting in the formation of *CHOCO intermediates. The subsequent C_1–C_2 coupling (*CH_2OCO + *CO → *CH_2OCOCO) was found to be a thermodynamically favorable exothermic process. The DFT results revealed that Cu–Ti–V_O units have the ability to stabilize *CHOCO and *CH_2OCOCO intermediates, leading to a reduction in their energy levels. This stabilization was probably due to the largely alleviation of electron accumulation and relaxation of the intermolecular and intramolecular electrostatic repulsion within Cu–Ti–VO units. This mechanism can potentially enable both C_1–C_1 and C_1–C_2 coupling processes to become favorable exothermic reactions.

3.1.4 Cu-Based Heterojunctions

The construction of heterojunctions is regarded as one of the most effective strategies for enhancing the charge separation and transfer processes, consequently improving overall photocatalytic efficiency [115–118]. Copper-based heterojunctions may involve copper in various forms, such as Cu NPs or CuO, combined with other semiconductor materials, in a way that forms a junction between them. For instance, the introduction of Cu (metal, oxide, and quantum dots) as cocatalyst for heterostructures with various semiconductors (such as g-C_3N_4, TiO_2, ZnV_2O_4, etc.) was demonstrated to effectively broaden the photoresponse range and effectively improve the PCO_2RR activity/selectivity toward C_{2+} compounds [119–126]. It is worth noting that despite metal copper itself does not have photocatalytic activity, it has high electrical conductivity, which may enhance the effectiveness of other photocatalysts when combined with them. For instance, Zhao et al. successfully constructed a metal–semiconductor (m–s) heterojunction of Cu-dispersive protonated g-C_3N_4 (PCN) through a thermal reduction process of Cu_2O/PCN, where the total conversion rate of CO_2 to CH_3OH and C_2H_5OH reached 25.0 µmol g^{-1} under UV–Vis irradiation for 4 h.
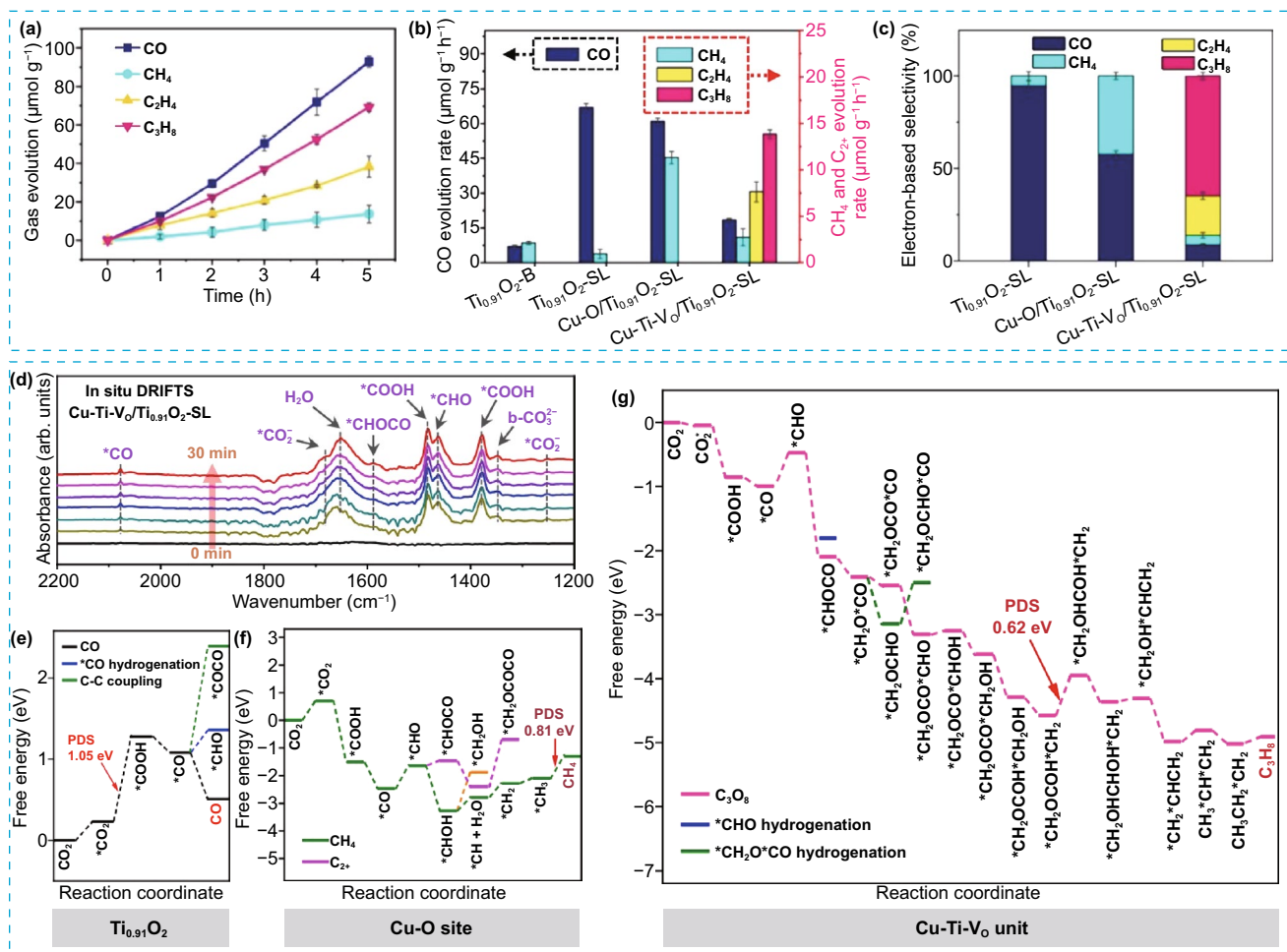
Fig. 12 a The evolution of photocatalytic production as a function of light irradiation times on Cu–Ti–V_O/Ti$_{0.91}$O$_2$–SL, **b** production rates, **c** electron-based selectivity, **d** in situ DRIFTS spectra of CO$_2$ reduction on Cu-Ti-V_O/Ti$_{0.91}$O$_2$-SL photocatalyst, gibbs free energy diagrams of CO$_2$ reduction on **e** Ti$_{0.91}$O$_2$ matrix, **f** Cu–O site, and **g** Cu–Ti–VO unit. Reproduced with permission [107]. Copyright 2023, Nature

This value was 4.18 and 1.84 times higher than those obtained from PCN and Cu$_2$O/PCN, respectively [123]. The Cu/PCN heterojunction demonstrated a selectivity of 51.42% for CH$_3$OH and 46.14% for C$_2$H$_5$OH. These outcomes indicated that the heterojunction effectively facilitates the separation of charge carriers and inhibits their recombination, resulting in high yield of C$_1$ and C$_2$ products. In another study, Zhao et al. reported the preparation of metal–semiconductor Cu/ZnV$_2$O$_4$ heterojunction for the photocatalytic CO$_2$ reduction to CH$_3$OH and C$_2$H$_5$OH [124]. They found that composite Cu^0-ZnV$_2$O$_4$ increased the surface area and adjusted the energy band position in a way that matched with the reaction potential toward CH$_3$OH and C$_2$H$_5$OH. The improved photocatalytic activity over Cu/ZnV$_2$O$_4$ was due to the heterojunction

interface's ability to facilitate rapid transmission and hinder the recombination of the photogenerated charges.

In a study conducted by Yu et al., they investigated the impact of depositing CuO$_x$ onto BiVO$_4$ for the photocatalytic conversion of CO$_2$ into hydrocarbons [127]. They synthesized monoclinic BiVO$_4$ crystals with a truncated tetragonal bipyramidal shape, allowing for controlled ratios of exposed {010} and {110} facets. Notably, they observed that CuO$_x$ NPs were selectively deposited onto the {010} facets of the BiVO$_4$ crystals. Compared to pure BiVO$_4$, the CuO$_x$/BiVO$_4$ catalysts, which maintained a uniform truncated tetragonal bipyramidal morphology, exhibited a higher rate of hydrocarbon fuel formation, including CH$_4$, C$_2$H$_6$, and C$_3$H$_8$. The improved photocatalytic activity was attributed to the enhanced efficiency of charge carrier separation, facilitated

by the presence of a Z-scheme junction at the interface between α-CuO_x and $BiVO_4$. In another study [128], Z-type Cu_2O-modified BiOI microspheres were synthesized through chemical deposition. The incorporation of Cu_2O onto the surface of BiOI served to enhance the specific surface area of BiOI, providing more exposed active sites. Additionally, the close interaction between Cu_2O and BiOI facilitated the efficient separation and migration of photogenerated carriers, as well as the use of sunlight. Compared to pristine BiOI, the Cu_2O/BiOI heterojunction photocatalyst exhibited superior photocatalytic activity. Notably, it resulted in higher yields of CH_3OH and C_2H_5OH CO_2 photoreduction, with yields reaching 609.05 and 273.96 μmol g_{cat}^{-1}, respectively.

Besides, Zhao et al. reported the construction of hybrid photocatalyst (CuO_X@p-ZnO) in which CuO_X is evenly distributed throughout polycrystalline ZnO. This photocatalyst demonstrated the ability to reduce CO_2 to C_2H_4, achieving a production rate of 22.3 μmol g^{-1} h^{-1} and a selectivity of 32.9% [27]. The combination of X-ray absorption fine structure spectra and in situ FT-IR studies demonstrated that Cu was predominantly present as CuO (Cu^{2+}) in the initial catalyst. Nevertheless, during the photocatalytic process, a distinctive surface layer of Cu^+ emerged over the CuO matrix, which served as the active site for capturing in situ generated CO and promoting its transformation into C_2H_4 through C–C coupling. In situ FT-IR analysis successfully identified *OC–COH intermediate during the PCO$_2$RR, marking the first experimental observation of this intermediate. Additionally, theoretical calculations revealed the significant contribution of Cu^+ sites in improving the binding of *CO and enhancing the stabilization of the *OC–COH intermediate (Fig. 13a). This study reveals how the Cu valence state could affect the reaction pathway of CO_2 reduction to produce C_{2+} compounds. The same group recently successfully synthesized a π–π stacking hybrid structure between g-C_3N_4 and 2D MOF of Cu-CuTCPP [125]. The resulting catalyst was able to convert CO_2 to C_2H_6 and achieving a C_2H_6 selectivity of 44% (Fig. 13b and c). Interestingly, they identified a light-driving reconstruction of Cu-CuTCPP moiety ($Cu^{II}_2(COO)_4 \rightarrow Cu^{1+\delta}_2(COO)_3$) by the photoinduced
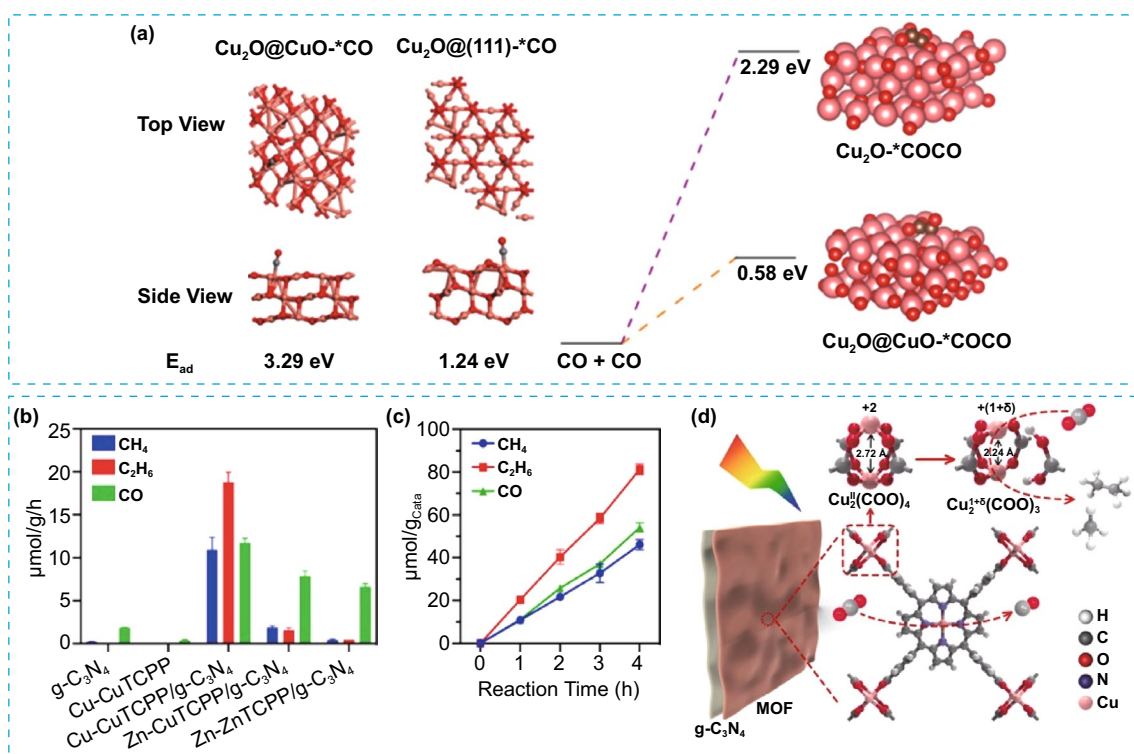

Fig. 13 **a** Theoretical calculations of the adsorption energy of *CO and first-principles calculations of the C–C coupling process on Cu_2O and Cu_2O@CuO. Reproduced with permission [27]. Copyright 2021, American Chemical Society. **b** PCO$_2$RR results on g-C_3N_4, Cu-CuTCPP, Cu-CuTCPP/g-C_3N_4, Zn-CuTCPP/g-C_3N_4, and Zn-ZnTCPP/g-C_3N_4, **c** photocatalytic CO_2 reduction on Cu-CuTCPP/g-C_3N_4, and **d** the self-reconstruction of paddle-wheel $Cu^{II}_2(COO)_4$ during the PCO$_2$RR. Reproduced with permission [125]. Copyright 2022, Elsevier

electrons from excited g-C$_3$N$_4$ as depicted in Fig. 13d. The self-reconstruction mainly improved the stabilization of *CO intermediates as well as the synergistic effect of the dual-Cu site, leading to efficient C–C coupling to produce C$_2$H$_6$.

As mentioned above, the selectivity of Cu-based photocatalysts depends on the oxidation state of Cu. However, the use of Cu in photocatalysis is not yet fully developed as it exhibits poor stability caused by the variations in its oxidation states by the photoinduced charges. Therefore, it is crucial to ensure the stability of Cu to fully utilize its intrinsic photocatalytic properties. To date, the formation of heterojunctions with other photocatalysts is a widely employed approach to improve the stability of Cu. For

example, Liu et al. employed a complexation oxidation approach for the encapsulation of CuO QDs in the pores of metal organic framework of MIL-125(Ti) and further combined it with g-C$_3$N$_4$ to construct a composite photocatalyst, (g-C$_3$N$_4$/CuO@MIL-125(Ti)), as illustrated in Fig. 14a [126]. This encapsulating structure ensured high stability and reusability of the catalyst. Furthermore, the obtained composite facilitated an efficient electron transfer from MIL-125(Ti) and g-C$_3$N$_4$ nanosheets to the CuO QDs, boosting the density of electrons over the QDs (Fig. 14b). Consequently, the initial composition of the product shifted from C$_1$ (CH$_3$OH, CO) to mainly C$_{2+}$ compounds (CH$_3$CH$_2$OH, CH$_3$CHO) for g-C$_3$N$_4$/CuO@
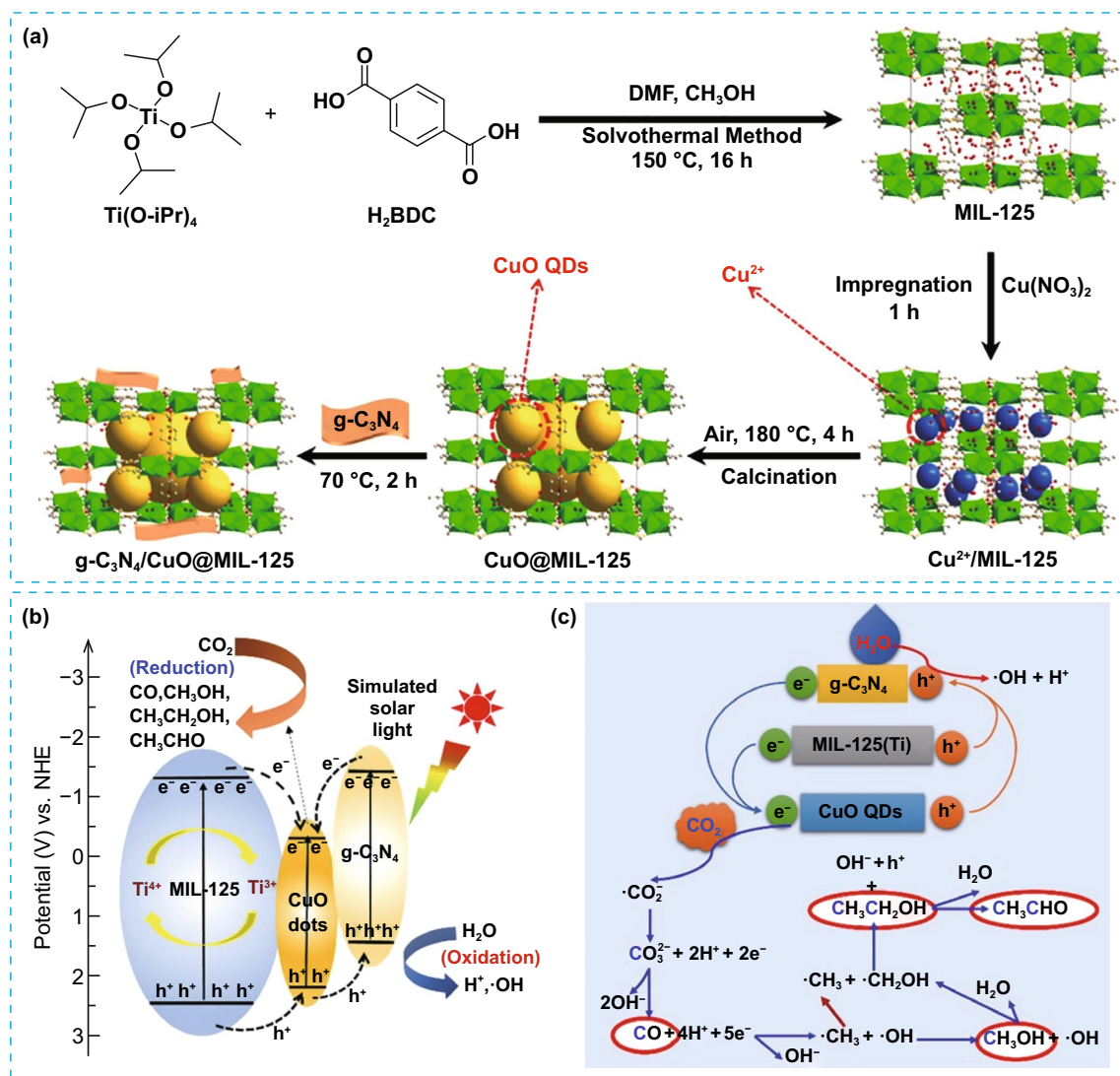
Fig. 14 **a** Schematic illustration for the synthesis of g-C$_3$N$_4$/CuO@MIL-125(Ti) composite photocatalyst, **b** the charge transfer process, and **c** the proposed reaction pathway over g-C$_3$N$_4$/CuO@MIL-125(Ti) photocatalyst. Reproduced with permission [126]. Copyright 2020, Elsevier

MIL-125(Ti), representing about 77% of the total formed products as shown in Fig. 14c.

In summary, several approaches such as optimising crystal phase and morphology, introducing metal doping, engineering defects, fabricating heterostructures, and utilizing bimetallic synergies have been shown to enhance the efficiency and selectivity of Cu-based materials toward the formation of C_{2+} products in PCO_2RR. These approaches impact the reaction routes primarily by stabilizing the crucial C_1 or C_2 intermediates, decreasing the reaction barrier, offering more active sites, as well as increasing the electron and proton density to facilitate the C–C coupling for the C_{2+} production. Table 2 lists the photocatalytic systems that have been reported for PCO_2RR into C_{2+} products.

3.2 Electrocatalytic CO_2 Reduction Reaction

The selection of the right electrocatalyst is a critical factor that determines the efficacy ECO_2RR process. It impacts the reaction kinetics, selectivity of possible products, and the required overpotential. So far, copper-based materials are the most effective electrocatalysts for ECO_2RR to C_{2+} products, but they are still relatively unselective. This is owing to the moderate binding affinity of copper to carbon monoxide which allows the generation of a wide range of products including, but not limited to, methane, methanol, ethylene, ethane, ethanol, and propanol [129–136]. Nevertheless, the origin of the enhanced activity/selectivity of Cu-based materials in ECO_2RR toward C_{2+} chemicals production is not easily identified. To date, many factors have been shown to affect the overall mechanism to C_{2+} products including the experimental setup conditions (pH, cation/anion of electrolyte, temperature, pressure, and applied overpotential) [137–143] and the catalyst surface properties (morphology, oxidation states, exposed facets, and defects) [144–148]. In this section, the relationship between the Cu surface and the performance of ECO_2RR is discussed, with the aim of comprehending the origin of the improvement observed in C_{2+} production over Cu-based materials. The discussion is approached from a materials viewpoint, and the Cu-based materials for ECO_2RR are categorized into three groups: Cu metal/oxides, Cu alloys, and Cu-based single-atom catalysts (Cu SACs). Table 3 provides a summary of the use of Cu-based catalysts in ECO_2RR to C_{2+} compounds.

3.2.1 Cu Metal/Oxides

The copper surface morphology and geometry have significant effects on the type of products generated during ECO_2RR. The faradic efficiencies (FE) for the formation of methane and C_2 products (ethylene and ethanol) on polycrystalline Cu surfaces at -5 mA cm^{-2} in 0.1 M KHCO$_3$ are approximately 29% and 37%, respectively. The presence of heterogeneous catalytic sites on the polycrystalline Cu plane may account for the insufficient selectivity [135]. Significant improvements were found by using single-crystal Cu(100) and cleaved Cu(100) surfaces with high-indexed planes. For example, Cu(S)-[4(100)×(111)] surface showed the formation of ethanol and ethylene with a total FE of about 57% [149]. It is suggested that the atomic steps and a square arrangement of Cu atoms in the (100) terraces facilitate the coupling of CH$_x$O intermediates, thereby contributing to the generation of more C_{2+} products. Even though Cu(100) single crystals are the optimal for ethylene production, they still produce a considerable quantity of methane. However, the use of Cu cubes with (100) facets, having an edge length of approximately 100 nm, can further enhance ethylene selectivity by almost completely suppressing methane formation [150].

In a study by Buonsanti et al., the influence of size and shape of Cu nanocrystals (NCs) on the activity and selectivity in ECO_2RR was investigated [151]. By using colloidal chemistry approach, Cu NC spheres with two distinct sizes (7.5 and 27 nm) and Cu NC cubes with three different sizes (24, 44, and 63 nm) were synthesised (Fig. 15a–e). The X-ray diffraction patterns for Cu NC cubes and spheres were compared, revealing that the Cu cubes were dominated by {100} facets, as indicated by the more pronounced (200) peak compared to the bulk fcc Cu reference (Fig. 15f). The results showed that, while smaller nanoparticles with the same morphology demonstrated greater activity, the cube-shaped nanoparticles displayed greater intrinsic activity compared to the spheres (Fig. 15g). A noteworthy observation was the nonlinear trend in selectivity, as Cu cube nanoparticles with a side length of 44 nm exhibited 80% selectivity toward carbon products, of which 50% was identified as ethylene. The superior activity observed in the Cu NC cubes (44 nm) can be attributed to the optimal proportion of edge sites to (100) plane sites ($N_{edge}/N_{100} = 0.025$), as evidenced by the statistical analysis of the surface atom density (Fig. 13h), which emphasizes the crucial role of edge

Table 2 Summary of activity of Cu-based photocatalysts for C_{2+} products

Photocatalyst	Light source	Main products	Yield	References
$Cu_{0.33}$-$Pt_{0.67}$/TiO_2	Solar simulator 32 cm. AM1.5 sunlight	CH_4	2.60 mL g^{-1} h^{-1},	[37]
		C_2H_4	0.33 mL g^{-1} h^{-1}	
		C_2H_6	0.47 mL g^{-1} h^{-1}	
Three-dimensional porous Cu_2O	300 W Xe lamp ($\lambda > 420$ nm)	CO	26.8 μmol g^{-1} h^{-1}	[84]
		CH_4	4.04 μmol g^{-1} h^{-1}	
		C_2H_4	0.66 μmol g^{-1} h^{-1}	
CdS/(Cu-TNTs)	450 W Xe lamp ($\lambda > 420$ nm)	CH_4	49.1%	[86]
		C_2H_4	1.3%	
		C_2H_6	31.3%	
		C_3H_6	0.5%	
		C_3H_8	17.9%	
AuCu/g-C_3N_4	300 W Xe lamp ($\lambda > 420$ nm)	CH_3OH	0.14 mmol g^{-1} h^{-1}	[87]
		CH_3CH_2OH	0.89 mmol g^{-1} h^{-1}	
$Cu_{0.8}Au_{0.2}$/TiO_2	300 W xenon lamp (light intensity, 500 mW cm^{-2})	CH_4	3578.9 μmol g^{-1} h^{-1}	[88]
		C_2H_4	369.8 μmol g^{-1} h^{-1}	
Cu–Pt/BT (blue titania)	Xe-arc lamp with an AM 1.5 filter (100 W, 100 mW cm^{-2})	CH_4	3.0 mmol g^{-1} h^{-1}	[89]
		C_2H_6	0.15 mmol g^{-1} h^{-1}	
AgCu-TNTA	Solar simulator, AM1.5 sunlight	CH_4	9.38 μmol g^{-1} h^{-1}	[15]
		C_2H_6	14.5 μmol g^{-1} h^{-1}	
$CuGaS_2$/Ga_2S_3	300 W Xe lamp with a 420 nm cutoff filter ($\lambda > 420$ nm)	CO	51 μmol g^{-1} h^{-1}	[93]
		CH_4	19 μmol g^{-1} h^{-1}	
		C_2H_4	335 μmol g^{-1} h^{-1}	
CuACs/PCN	300 W Xe lamp ($\lambda > 420$ nm)	CH_4	26.85 μmol g^{-1}	[100]
		C_2H_4	30.51 μmol g^{-1}	
Cu SAs/UiO-66-NH_2	300 W Xe lamp with a cut-off filter of 400 nm	CH_3OH	5.33 μmol g^{-1} h^{-1}	[101]
		CH_3CH_2OH	4.22 μmol g^{-1} h^{-1}	
Re-bpy/PTF(Cu)	300 W Xe lamp ($\lambda > 420$ nm)	CO	-	[102]
		CH_4	-	
		C_2H_4	73.2 μmol g^{-1} h^{-1}	
0.02%Co-1%Cu/TiO_2	Solar simulator, AM1.5 sunlight	CO	135.94 μmol	[103]
		CH_4	127.05 μmol	
		C_2H_6	267.60 μmol	
		C_3H_8	10.07 μmol	
InCu/PCN	Solar simulator, AM1.5 sunlight	CO	5.8 μmol g^{-1} h^{-1}	[104]
		CH_4	1.2 μmol g^{-1} h^{-1}	
		CH_3CH_2OH	28.5 μmol g^{-1} h^{-1}	
$Cu^{\delta+}$/CeO_2-TiO_2	300 W Xe lamp (light intensity 200 mW cm^{-2})	CO	3.47 μmol g^{-1} h^{-1}	[105]
		CH_4	1.52 μmol g^{-1} h^{-1}	
		C_2H_4	4.51 μmol g^{-1} h^{-1}	
CuPt/WO_3	300 W xenon lamp	HCOOH	2.62 μmol g^{-1} h^{-1}	[106]
		CH_3COOH	19.41 μmol g^{-1} h^{-1}	
Cu-Ti-V_O/$Ti_{0.91}O_2$-SL	300 W Xe lamp	CO	18.6 μmol g^{-1} h^{-1}	[107]
		C_2H_4	7.6 μmol g^{-1} h^{-1}	
		C_3H_8	13.8 μmol g^{-1} h^{-1}	
15 wt% Cu/GO	Halogen lamp (light intensity 100 mW cm^{-2})	CH_3CHO	1.79 μmol g^{-1} h^{-1}	[119]
SCN-Cu/TiO_2-SBO Defective titania	300 W xenon lamp simulated sunlight	CO	2.3 μmol g^{-1} h^{-1}	[121]
		CH_4	10 μmol g^{-1} h^{-1}	
		C_2H_4	4.8 μmol g^{-1} h^{-1}	

Table 2 (continued)

Photocatalyst	Light source	Main products	Yield	References
Nb_2O_5/CuO 2.5%	UVC lamp (light intensity 21.49 mW cm^{-2})	CH_4	28 μmol g^{-1}	[122]
		HCOOH	7.5 μmol g^{-1}	
		CH_3COOH	72 μmol g^{-1}	
Cu/PCN	300 W xenon lamp (luminous power of 2.5 W)	CH_3OH	13.8 μmol g^{-1}	[123]
		CH_3CH_2OH	11.2 μmol g^{-1}	
Cu/ZnV_2O_4	300 W xenon lamp	CO	–	[124]
		CH_4	–	
		CH_3OH	3.30 μmol g^{-1} h^{-1}	
		CH_3CH_2OH	0.86 μmol g^{-1} h^{-1}	
CuO_X@p-ZnO	300 W xenon lamp (150 mW cm^{-2})	CO	27.3 μmol g^{-1} h^{-1}	[27]
		CH_4	17.9 μmol g^{-1} h^{-1}	
		C_2H_4	22.3 μmol g^{-1} h^{-1}	
Cu-CuTCPP/g-C_3N_4	300 W xenon lamp with both UV-cut and IR-cut filter (150 mW cm^{-2})	CO	12.3 μmol g^{-1} h^{-1}	[125]
		CH_4	11.6 μmol g^{-1} h^{-1}	
		C_2H_6	18.5 μmol g^{-1} h^{-1}	
g-C_3N_4/CuO@MIL-125(Ti)	300 W xenon lamp	CO	180.1 μmol g^{-1}	[126]
		CH_3OH	997.2 μmol g^{-1}	
		CH_3CH_2OH	1505.7 μmol g^{-1}	
		CH_3CHO	531.5 μmol g^{-1}	

Table 3 Summary of recent Cu-based catalysts applied for CO_2RR to C_{2+} products

Catalyst	Electrolyte	Potential	Products	FE (%)	References
Cu/CNS	0.1 M $KHCO_3$	-1.2 V$_{RHE}$	CH_3CH_2OH	63	[134]
Cu_2O	0.1 M $KHCO_3$	-0.99 V$_{RHE}$	C_2H_4	39	[136]
			CH_3CH_2OH	16	
Cu cubes	0.1 M $KHCO_3$	-1.1 V$_{RHE}$	C_2H_4	41	[153]
Cu foils	0.1 M $KHCO_3$	-0.9 V$_{RHE}$	C_2H_4	60	[155]
Cu_2O	0.1 M $KHCO_3$	-1.1 V$_{RHE}$	C_2H_4	57.3	[156]
Cu	0.1 M $KHCO_3$	-1.2 V$_{RHE}$	$C_2H_4 + CH_3CH_2OH + CH_3COOH$	54	[150]
Gd/CuO_x	2 M KOH	-0.8 V$_{RHE}$	$C_2H_4 + CH_3CH_2OH + CH_3COOH + $ n-Pr	81.4	[164]
Zn-Cu	0.1 M $KHCO_3$	-1.1 V$_{RHE}$	C_2H_4	33	[168]
Ag–Cu	0.1 M $KHCO_3$	-1.1 V$_{RHE}$	C_2H_4	37	[169]
Cu-Ag	1M KOH	-0.7 V$_{RHE}$	C_2H_4	60	[173]
			CH_3CH_2OH	25	
Ag_xCu_{100-x} Cu rich	0.5 M $KHCO_3$	-0.9 V$_{RHE}$	C_2H_4	60.3	[174]
			CH_3CH_2OH		
HKUST-1	1M KOH	-1.07V$_{RHE}$	C_2H_4	45	[179]
Cu(OH)BTA	1M KOH	-0.87 V$_{RHE}$	C_2H_4	57	[182]
			CH_3CH_2OH	11	
			CH_3COOH	4	
			n-Pr	1	
Cu-SA/NPC	0.1 M $KHCO_3$	-0.76V$_{RHE}$	CH_3COCH_3	36.7	[183]
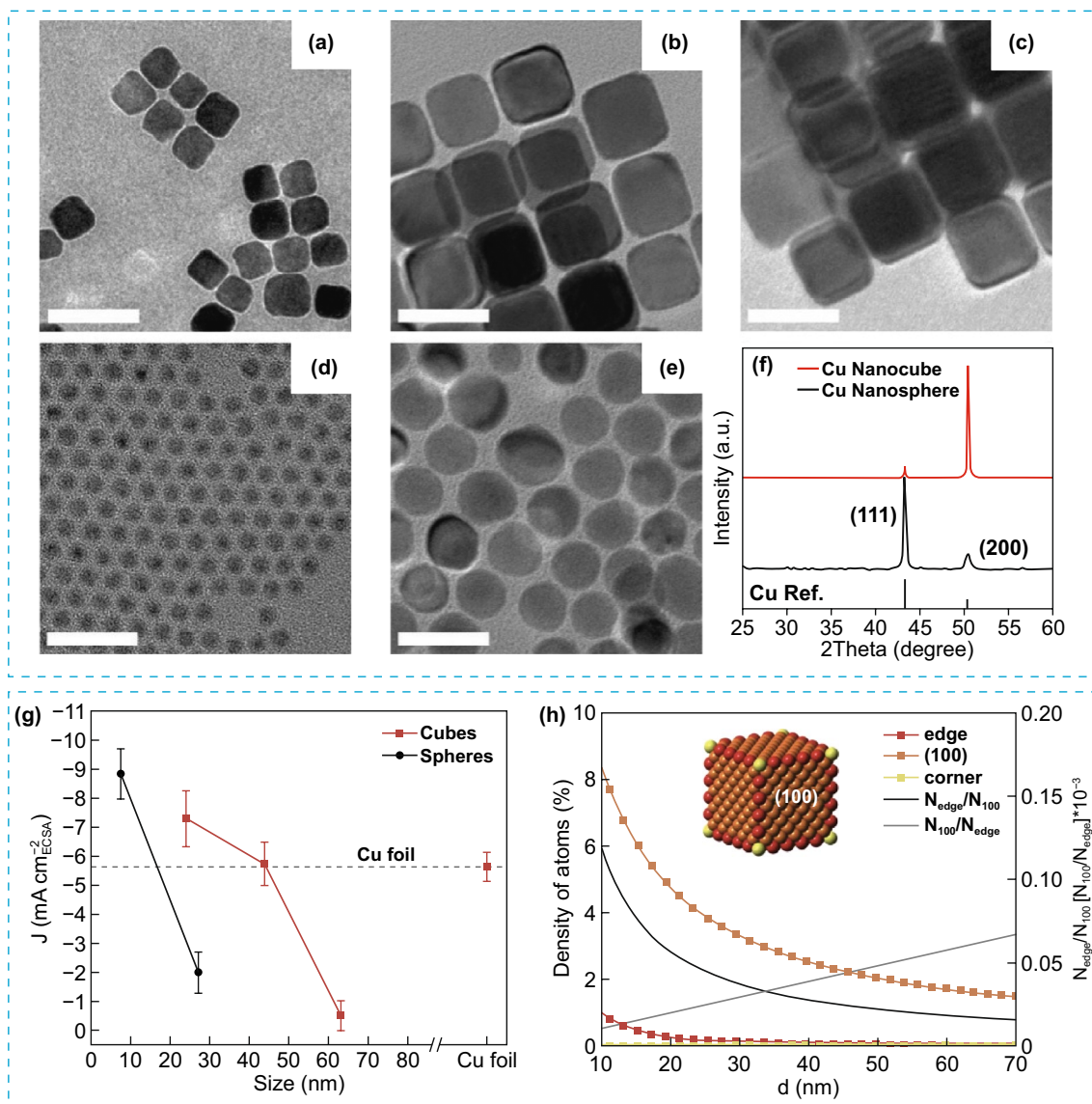
Fig. 15 TEM images of Cu cubes with an average edge length of **a** 24 nm, **b** 44 nm, **c** 63 nm, TEM images of Cu spheres with an average diameter of **d** 7.5 nm, **e** 27 nm, **f** XRD patterns of the Cu cubes and Cu spheres, **g** current density at -1.1 V_{RHE} plotted versus the size of the Cu NC catalysts, and **h** density of adsorption sites in Cu NC cubes (left axis) and trend Nedge/N100 and N100/Nedge (right axis) versus the edge length. Reproduced with permission [151]. Copyright 2016, Wiley–VCH

atoms in the active sites that selectively drive ECO$_2$RR and ethylene production in these Cu nanocrystal cubes.

In another study, researchers explored the effect of copper nanowire (Cu NW) morphology on ECO$_2$RR toward C$_{2+}$ hydrocarbons [152]. It was observed that the selectivity for C$_{2+}$ hydrocarbons, on Cu NWs array electrodes could be finely adjusted by systematically modifying the Cu NW length and density, which could be controlled by varying the reaction times (Fig. 16a–d). Their findings indicated a

gradual increase in the formation of C$_2$H$_4$ as the length and thickness of Cu nanowires increased. As shown in Fig. 15e, at a length of 8.1 mm for the Cu NWs, the FE for C$_2$H$_4$ formation reached 17.4%, while the production of H$_2$ is simultaneously reduced.

Nanomaterials with controlled morphology play a pivotal role in both assessing the effect of different facets on the ECO$_2$RR and designing catalysts with superior performance and selectivity. In this regard, Yin and colleagues [153]
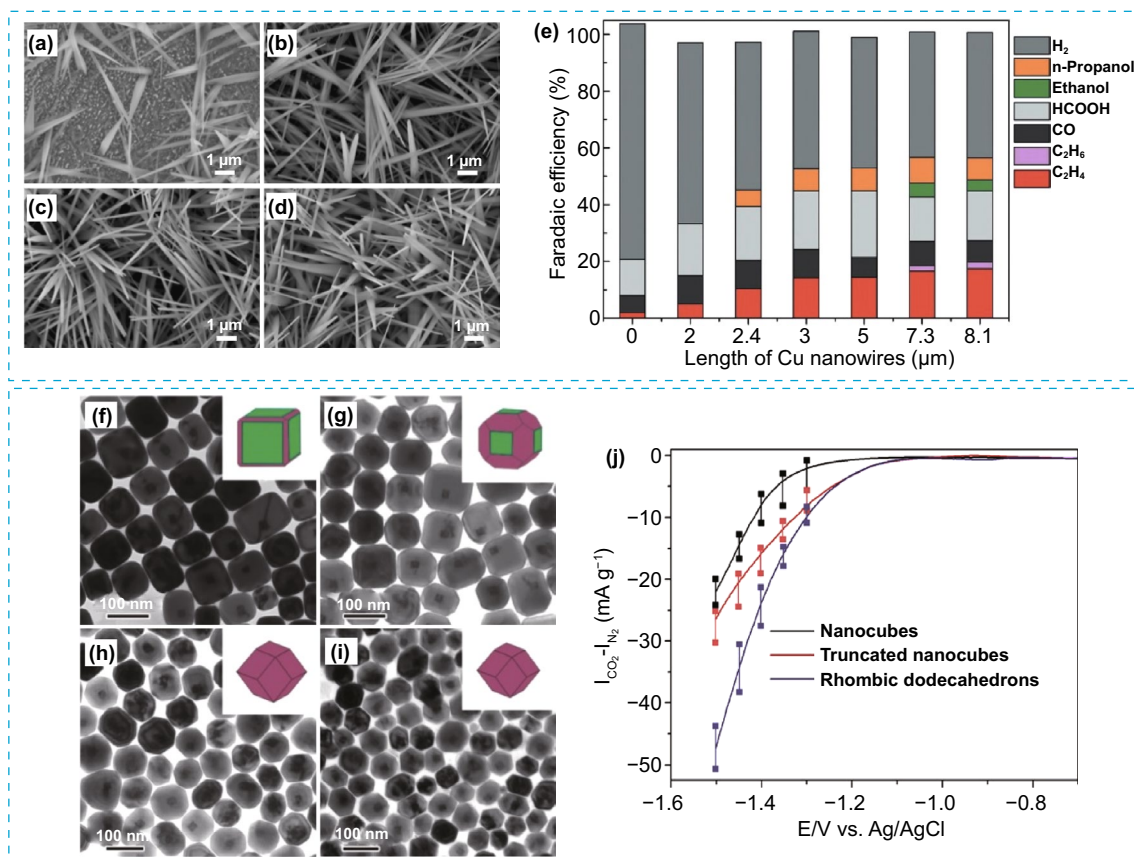
Fig. 16 a–d SEM images of Cu(OH)$_2$ nanowires with synthesis time of 1, 3, 5, and 8 min, respectively, **e** FE for different products on Cu nanowire arrays with different lengths at -1.1 V$_{RHE}$ in CO$_2$-saturated 0.1 M KHCO$_3$ electrolytes. Reproduced with permission [152]. Copyright 2016, Wiley–VCH. **f-i** TEM images of as-etched Cu NCs subjected to different etching periods of 4 h, 8 h, 12 h, and 24 h, respectively. Reproduced with permission [153]. Copyright 2016, American Chemical Society

reported the synthesis of cubic Cu NPs through chemical etching, spanning across different time intervals, leading to the formation of various shapes as illustrated in Fig. 16f–i. Notably, when the nanocrystals were etched for a duration exceeding 12 h, they exhibited a rhombic dodecahedral morphology, prominently exposing high-energy (110) facets. When compared to Cu nanocubes, rhombic dodecahedral Cu NPs exhibit a positive onset potential of -1.1 V$_{RHE}$. Additionally, at -1.4 V$_{RHE}$, the current density for the rhombic dodecahedral structure is approximately three times higher than that of Cu nanocubes. This observation indicates that the Cu crystal structure with enriched (110) facets outperforms the one with (100) facets in terms of catalytic activity as depicted in Fig. 16j. The presence of high-energy (110) facets in the rhombic dodecahedral Cu structure leads to increased selectivity for the formation of C$_{2+}$ products, including C$_2$H$_4$, C$_2$H$_6$, and C$_3$H$_8$ when compared to the

original (100) facet of cubic Cu. These findings suggest that the (110) facet of rhombic dodecahedral Cu is particularly conducive to the formation of C$_{2+}$ hydrocarbons in ECO$_2$RR.

In addition to considering structural parameters including particle size/shape and reactive facets, it has been suggested that the surface state of Cu is an important factor influencing the activity and product selectivity in ECO$_2$RR. Recently, it was demonstrated that the interaction between the surfaces made of Cu$^+$ and Cu^0 restrains the C$_1$ pathways while promoting CO–CO dimerization owing to the attraction between carbon atoms with opposite charges stimulated by the interface between Cu$^+$ and Cu^0 [154]. According to a recent study, oxide-derived copper catalysts, activated using oxygen plasma, showed a noteworthy ethylene FE of 60% at -0.9 V$_{RHE}$. This high efficiency was related to the existence of Cu$^+$ species. Interestingly, through the in situ hard X-ray absorption spectroscopy (hXAS) analysis, it was observed

that stable Cu$^+$ species were detected at notably negative potentials of about -1.0 V$_{RHE}$ during the ECO$_2$RR [155].

In a study conducted by Hwang et al., it was found that the initial stages of ECO$_2$RR caused fragmentation of Cu$_2$O NPs, leading to improved C$_2$H$_4$ selectivity and activity [156]. The researchers utilized a cysteamine immobilization agent to synthesize Cu$_2$O nanoparticles by direct growth on carbon black, which initially measured at a size of 20 nm, but were found to be broken down into smaller sizes (2–4 nm) with denser arrangement and deformed crystal planes after 10 h of ECO$_2$RR. These morphological changes over reaction time led to higher activity, with a C$_2$H$_4$ FE of 57.3% achieved at -1.1 V$_{RHE}$ in 0.1 M KHCO$_3$. In situ/operando XANES analysis revealed a shift in oxidation state from Cu$^+$ to Cu^0, suggesting that Cu^0 was the dominant state during the electrochemical CO$_2$ reduction, even in Cu catalysts derived from the oxide material. Upon fragmentation of the initial Cu NPs, they underwent re-oxidation to Cu$^+$ states without air exposure, whereas large Cu NPs retained their Cu^0 state when subjected to open-circuit potential conditions, suggesting that the morphological alterations observed in fragmented Cu$_2$O nanoparticles enable greater oxygen access and contribute to improved CO$_2$ reduction efficiency.

In another study, Sargent et al. reported the electro-redeposition of Cu (ERD Cu) from a Cu$_2$(OH)$_3$Cl sol–gel precursor to control the morphology and oxidation state of Cu in order to inhibit CH$_4$ formation and enhance C$_2$H$_4$ production [150]. Various structural morphologies appeared as a function of applied potential, including rounded nanostructures (at -0.7 V$_{RHE}$), sharper needles (at -1.0 V$_{RHE}$), sharper nanowhiskers (at -1.2 V$_{RHE}$), and dendrites with rounded tips (at -1.4 V$_{RHE}$). The ERD Cu catalyst was found to exhibit a 54% FE for C$_{2+}$ products (ethylene, acetate, and ethanol) and an 18% FE for C$_1$ products (carbon monoxide, methane, and formate) at -1.2 V$_{RHE}$. Additionally, the C$_2$H$_4$ partial current density was high for ERD Cu in both the H-cell (22 mA cm^{-2} at -1.2 V$_{RHE}$) and flow cell (161 mA cm^{-2} at -1.0 V$_{RHE}$) configurations accompanied by notable inhibition of CH$_4$ with a C$_2$H$_4$/CH$_4$ ratio of 200. Notably, the high local pH induced by ERD Cu is an important factor in the suppression of CH$_4$. This is because ERD Cu generated remarkably high current densities, with a recorded 60 mA cm^{-2} in H-cell and 450 mA cm^{-2} in flow cell, resulting in a rapid consumption of protons that led to the elevated local pH [157, 158]. At high pH levels, CO dimerization pathway is most likely to occur because the CO

hydrogenation step is kinetically limited. At very negative potentials (less than -1.0 V$_{RHE}$), in situ soft X-ray absorption (sXAS) spectroscopy indicated the existence of Cu$^+$ species. For over 1 h of operation, it was up to 23% of the ERD Cu electrocatalyst consisted of Cu$^+$ species, even when subjected to a negative applied bias as low as -1.2 V$_{RHE}$, indicating a crucial role of Cu$_2$(OH)$_3$Cl sol–gel in stabilizing Cu$^+$ species at higher negative applied potentials. According to DFT calculation, it was observed that the ERD Cu(211) model, comprising of 25% Cu$^+$ species, closely resembling the optimal Cu$^+$ quantity identified through sXAS analysis, demonstrated the minimum Gibbs free energy of formation of the OCCOH* intermediate (1.13 eV). This value was 0.76 eV lower than that of the Cu(211) model. Moreover, the ERD Cu(211) surface showed the highest CO binding, as evidenced by a binding energy of -1.45 eV, indicating that the Cu$^+$ species has a significant impact on the stabilization of the OCCOH* intermediate, thereby promoting the formation of C$_2$ products over C$_1$ products. Overall, the Cu$^+$ site plays a crucial role in enhancing the selectivity toward C$_{2+}$ products by promoting the C–C coupling reaction through strengthened *CO adsorption and stabilized C$_2$ intermediates. Nevertheless, the low stability of Cu$^+$ species at negative potentials during the ECO$_2$RR remains a major impediment to its large-scale implementation. To address this challenge, metal doping is suggested as effective way to boost the stability of Cu$^+$ species [159–163].

Recently, the study conducted by Han et al. applied DFT calculations and multiple characterization tests to investigate the impact of atomic dopants on the efficiency of Cu-based catalysts or CO$_2$ electroreduction to C$_{2+}$ products [164]. Starting with DFT calculations, they explored the effectiveness of doping various single-atom metals (Ag, Pd, Ni, Zn, Sn, Ce, Sm, and Gd) of Cu$_2$O and identified single-atom Gd-doped Cu$_2$O as a highly promising choice for ECO$_2$RR to C$_{2+}$ products. This was attributed to its ability to enhance the CO$_2$ conversion to *CO, suppress HER, demonstrated lower thermodynamic limiting potentials for ECO$_2$RR, and exhibited moderate *CO binding energy. The characterization results of as-prepared Gd/CuO$_x$ confirmed that has the ability to stabilize Cu$^+$ species and induce tensile strain in the catalyst. The Gd/CuO$_x$ catalyst exhibited superior CO$_2$ conversion to C$_{2+}$ product, with a Faradaic efficiency of 81.4% and a partial current density of C$_{2+}$ product reaching 444.3 mA cm^{-2} at -0.8 V$_{RHE}$. Both DFT calculations and experiments revealed that the stability of

the key intermediate O*CCO was enhanced by Gd doping. Additionally, the energy barrier for the CO dimerization to O*CCO step is significantly affected by tensile strain, ultimately contributing to the superior performance of the Gd/CuO$_x$ catalyst in ECO$_2$RR to C$_{2+}$ products.

3.2.2 Cu Alloys

The introduction of a secondary metal to single Cu crystal can alter its chemical composition, leading to improved activity/selectivity by adjusting the binding strength of key intermediates on the catalyst surface. Thus, Cu alloys have garnered significant attention in this regard. Based on the previous experiments, Qiao et al. [165] introduced a classification system for the secondary metal of Cu alloys based on their relative affinities toward H and oxygen O, as illustrated in Fig. 17a. They proceeded to examine the distinct catalytic mechanisms and resultant product variations associated with each of these four affinity categories separately. For ECO$_2$RR, metals that exhibit a higher affinity for O but a lower affinity for H compared to Cu, such as Sn, In, Hg, and Pb, tend to result in the formation of a weakly bound *COOH intermediate after the initial reaction step. Consequently, the primary product of CO$_2$ reduction on these metal surfaces is HCOOH. There is even evidence to suggest that the reaction may proceed through an O-bound *OCHO intermediate on these metals. Conversely, metals with lower affinities for both O and H than Cu, including Zn, Ag, and Au, exhibit a stronger binding affinity for *COOH compared to *CO. Consequently, CO is desorbed as the primary product, with the formation of *COOH serving as the

potential determining step [166]. On the other hand, metals that possess both a stronger affinity for O and H than Cu, which include Co, Ni, Fe, and Pt, generally tend to favor the competitive HER with a minor amounts of hydrocarbons and alcohols being detected on the surfaces of these metal catalysts.

It was found that when group 1 metals including Au, Zn, and Ag (denoted as M$_1$) are the predominant component in Cu–M$_1$ systems, the primary product is CO, and the FE is generally better than that of the parent metals. This outcome is likely due to the increased O affinity of Cu, which stabilizes the *COOH intermediate, while the weak binding ability of M$_1$ metals for *CO facilitates the desorption of CO. However, in cases where M$_1$ provides a moderate contribution to the active sites, C$_{2+}$ products are generally produced with a high FE due to the synergistic effect between Cu and M$_1$. Moreover, the weak binding of H also suppresses HER, enhancing the overall selectivity for ECO$_2$RR (as illustrated in Fig. 17b). For group 2 metals (M$_2$), the trend suggests a preference for 2e$^-$ reduction products in Cu-M$_2$ systems, likely due to the weak H binding, which inhibits pathways beyond CO. When M$_2$ metals dominate the active sites, HCOOH becomes the major reduction product. This is attributed to the increased availability of O-binding sites, potentially leading to better stabilization of the *OCHO intermediate and a favorable pathway to HCOOH formation. It is noteworthy that there is limited research on the coupling of group 3 metals (M$_3$, specifically Pd) with Cu, and the intermetallic arrangement of these materials significantly influences product selectivity. When the metallic arrangement is more regular, CO becomes the major product and is
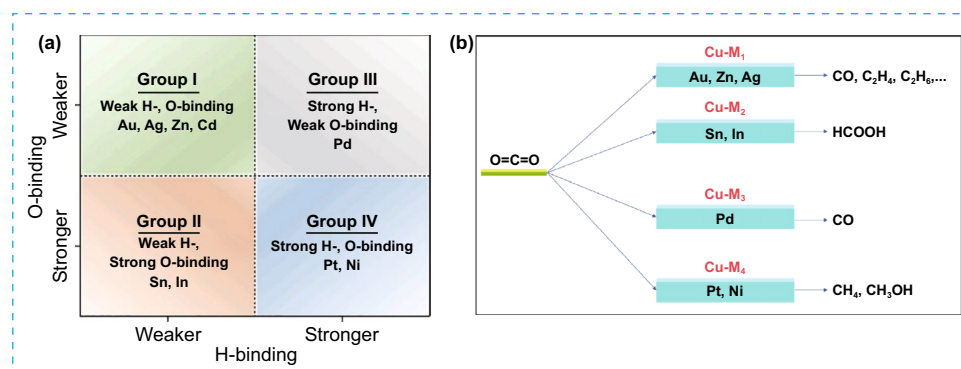

Fig. 17 a Classification of various metals into four groups in relation to Cu alloys based on O and H affinities from the previous studies. Reproduced with permission [165]. Copyright 2018, Elsevier. **b** Reaction products of electrocatalytic CO$_2$ reduction on different Cu alloys

produced with a high FE. There are fewer examples of group 4 metals including Pt and Ni (M_4) being coupled with Cu in the literature. Although M_4 metals with a strong affinity for CO should be avoided, these materials can produce CH_4 and CH_3OH with relatively high FE, indicating their potential for specific applications in ECO_2RR [165].

As mentioned above, the synergetic effect between Cu and group 1 metals (e.g., Au, Ag, or Zn) has been reported to improve the production of C_{2+} compounds [160, 167–171]. Specifically, the *CO dimerization process (which generates *OCCO) on bimetallic Cu surfaces could be facilitated owing to the enhanced reduction of CO_2 to CO via Au, Ag, or Zn sites. For instance, Kuhl et al. reported that the selectivity toward C_{2+} products of Au–Cu alloys was significantly higher than that of a monometallic Cu catalyst at -0.7 V_{RHE} using 0.1 M $KHCO_3$ as electrolyte [160]. In a study by Du et al., it was found that of C_2H_4 FE increased from 15 to 33% for a Cu and a Cu_4Zn_1 alloy catalyst, respectively [168]. Meanwhile, Buonsanti et al. explored Ag–Cu alloys and determined that, when operating at -1.1 V_{RHE}, using 0.1 M $KHCO_3$ as electrolyte, the C_2H_4 FE increased from 13 to 37% with Ag_1–$Cu_{1.1}$ alloy catalyst, as compared to the pure Cu catalyst [169]. Based on these studies, the guest metals (Au, Ag, and Zn) can boost the CO concentration near the catalyst surface, making it easier for Cu sites to convert it into C_{2+} products. The disposition of the guest metals on the surface of copper has the potential to alter the electronic states of the catalyst and to modify the interatomic distance between surface atoms and influence the reaction kinetics of the adsorbed intermediates on the surface. These factors may ultimately affect the chemical binding strengths of reaction, thereby modulating the reaction toward pathways that are more advantageous [171, 172]. For example, recent experiments by Timoshenko et al. using in situ EXAFS demonstrated how the composition and structure affect the product distribution of CO_2RR. The researchers observed that Cu-ZnNPs with shorter interatomic distances have a greater affinity for producing CH_4, whereas NPs with longer Cu–Zn distances are more likely to generate CO, which is then reduced to C_{2+} compounds [172].

Related to the high levels of C_{2+} selectivity at high activity challenges (current density $<< -200$ mA cm^{-2}, applied potentials $>> -1.0$ V_{RHE}) on Cu alloy-based catalysts, Gewirth et al. demonstrated the enhanced selectivity of ECO_2RR toward ethylene and ethanol with bimetallic CuAg catalyst synthesized by using additive-controlled electrodeposition method [173]. In an alkaline flow electrolyzer, the CuAg catalyst that has a nanoporous structure and a small amount of Ag ($< 10\%$) showed high ethylene selectivity ($\sim 60\%$) and ethanol production ($\sim 25\%$) at a relatively low applied potential of -0.7 V_{RHE} and a high current density of -300 mA cm^{-2}. According to the findings from in situ Raman analysis and control experiments, it can be inferred that the improved selectivity toward ethylene and ethanol can be ascribed to the presence of an optimal amount of Ag responsible for stabilizing the Cu_2O overlayer and to the higher flux of CO generated by the active promoter Ag that generated more CO intermediates during the ECO_2RR process. Recently, Shen et al. reported the use of Ag–Cu bimetallic surface alloys (Ag_xCu_{100-x}) prepared by a modified polyol method followed by electrochemical reduction as illustrated in Fig. 18a [174]. The chemical compositions of Ag_xCu_{100-x} alloys were rationally adjusted from Cu-rich to Ag-rich. Interestingly, different products including CO, C1 hydrocarbons/alcohols (C1-H/A) and C2 hydrocarbons/alcohols were selectively obtained over Ag_xCu_{100-x} alloys by modulating the surface chemical compositions and applied potentials. The findings indicated that the Ag_xCu_{100-x} alloys catalysts, having Cu-rich surface ranging from 14 to 34 at%, exhibited good selectivity toward C2-H/A products (C_2H_4 and C_2H_5OH) when subjected to applied potentials within the range of -0.85 to -1.0 V_{RHE}, as illustrated in Fig. 18b and c. For example, $Ag_{16}Cu_{84}$ catalyst showed a high $FE_{C2-H/A}$ of 60.3% at -0.90 V_{RHE}. Meanwhile, the increase in surface Ag compositions (Ag: 27–55 at%) in Ag_xCu_{100-x} alloys resulted in an enhanced formation of C1-H/A (namely, CH_4 and CH_3OH) with applied potentials shifted from -1.00 to -1.10 V_{RHE}. Specifically, the nearly-balanced Ag/Cu surface $Ag_{43}Cu_{57}$ displayed a high $FE_{C1-H/A}$ reaching 41.4% at -1.10 V_{RHE}. As expected, the Ag-rich surface alloys (Ag: > 74 at%) selectively convert CO_2 to CO at applied potentials between -0.90 and -1.15 V_{RHE}. As example, the $Ag_{83}Cu_{17}$ catalyst exhibited a high FE_{CO} of 74.0% at -1.10 V_{RHE}. The findings from DFT calculations show that the high-energy levels of d-band centers (E_d) on the surface of Cu-rich Ag_xCu_{100-x} result in a strong binding affinity for *CO and allow for coupling of *CO into *COCO over a wide potential range (-0.80 to -1.20 V_{RHE}), leading to a yield of C2H/A with high selectivity. For Ag/Cu balanced Ag_xCu_{100-x} alloys (Fig. 18e), a moderate binding strength of *CO was determined by the
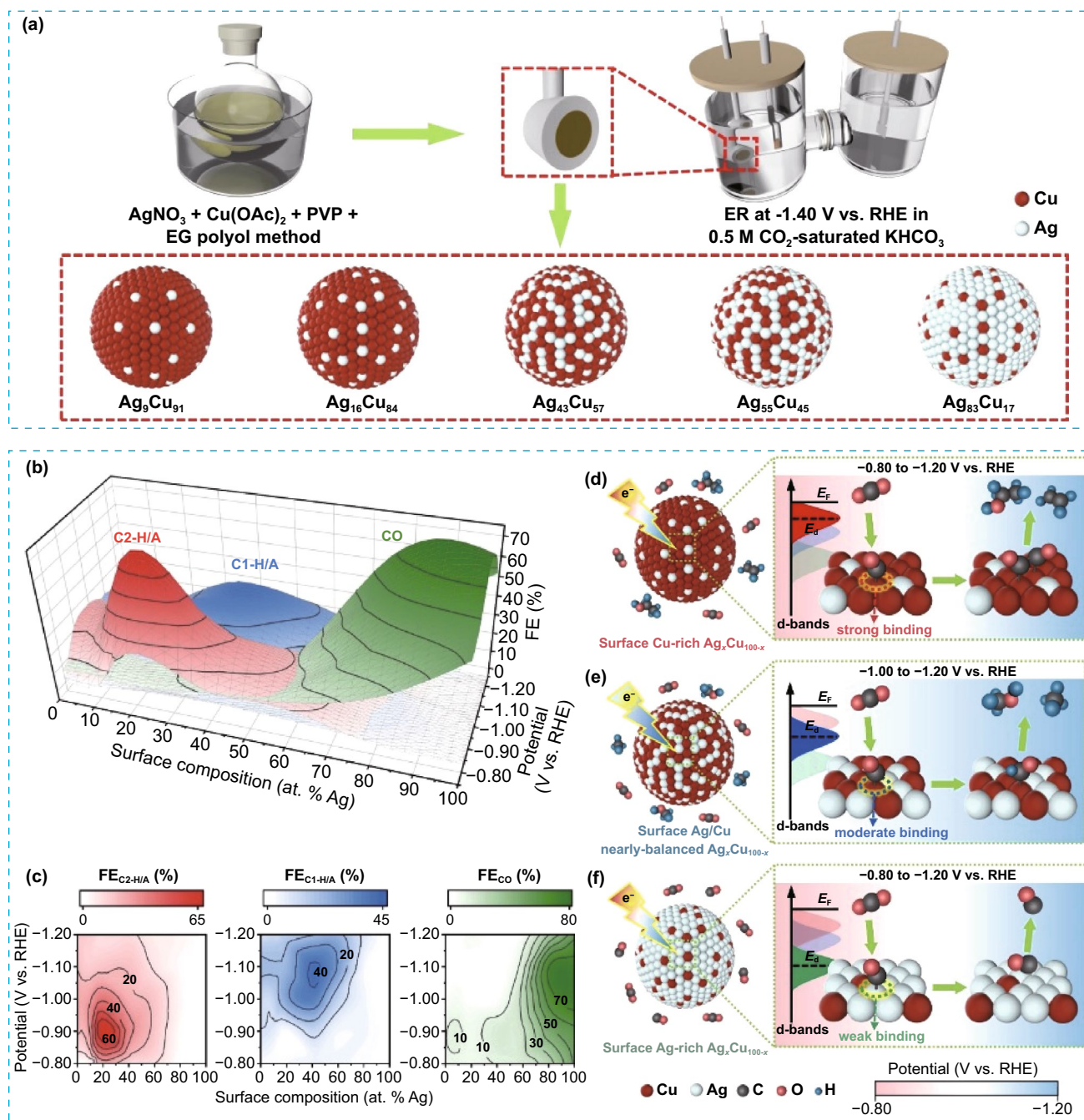
Fig. 18 a Schematic illustration of the synthetic processes of Ag_xCu_{100-x} alloys, **b** 3D colormap surface plot, **c** corresponding colortour maps for FE of different products vs. surface compositions and applied cathodic potentials, mechanism illustrations of selective production on Ag_xCu_{100-x} alloys, **d** C2H/A over surface Cu-rich, **e** C1H/A over surface Ag/Cu nearly-balanced, and **f** CO over surface Ag-rich. Reproduced with permission [174]. Copyright 2023, Wiley–VCH

downshifted E_d (− 3.24 to − 3.80 eV), which renders the hydrogenation of *CO to *CHO as predominate reaction, leading to selective formation of C1H/A products at high potential (more negative than − 1.0 V_{RHE}). However, in the Ag-rich Ag_xCu_{100-x} alloys (Ag: > 60 at%), the further

decreased E_d (< − 4.08 eV) resulting in weaker binding of *CO intermediates on the surface (Fig. 18f), which facilitate the desorption of *CO intermediates from the surface to generate CO with high selectivity across a wide range of potentials (− 0.80 to − 1.20 V_{RHE}). This study presents a

3.2.3 Cu SACs

Catalysts consisting of a single atom (SAs) with active metal centers distributed at the atomic level have been found to exhibit improved activity and tunable selectivity in ECO$_2$RR. This can be attributed mainly to the outstanding effectiveness in atom utilization, distinctive electronic structure, and unsaturated coordination surroundings of the metallic centers [175–177]. Considering that the CO$_2$RR occurs over solid–liquid–gas boundaries, maximizing the surface area is crucial in order to attain optimal electron and proton transfer across these interfaces. This can be achieved by reducing the CO$_2$RR to a single-atom scale and utilizing substrates that are highly porous and stable. Cu-SACs are of great interest among the SACs due to their remarkable ability to produce high C$_{2+}$ products with high selectivity. N-doped conductive carbon supports with N-chelated metal sites are frequently used examples for ECO$_2$RR. For instance, Guan et al. reported the use of a nitrogen coordination strategy for dispersing SAs Cu catalysts on nitrogen-doped carbon [178]. The incorporation of nitrogen promoted the dispersion and interaction of atomic copper species onto carbon frameworks doped with nitrogen via Cu–N$_x$ coordinations. The study revealed that when the Cu concentration reached 4.9%mol, the close proximity of Cu–N$_x$ species was sufficient to facilitate C–C coupling, leading to the generation of C$_2$H$_4$. Conversely, when the Cu concentration was below 2.4%mol, the gap between Cu–N$_x$ species was significant, favoring the production of CH$_4$. According to DFT calculations, the generation of C$_2$H$_4$ was facilitated by coupling two *CO intermediates on adjacent Cu–N$_2$ sites, whereas isolated Cu–N$_2$ and Cu–N$_4$ sites as well as neighboring Cu–N$_4$ sites promoted the production of CH$_4$. Despite the promising performance of Cu-SACs, there is still a need for more improvement in terms of C$_{2+}$ product selectivity and Faradaic efficiency. This is mainly due to the existence of ambiguous catalytic sites and the adverse electronic properties of Cu when coordinated with N.

According to reports, Cu-SACs have the ability to facilitate the crucial C–C coupling reaction, which is necessary for C$_{2+}$ products formation. Nonetheless, it was proven that these catalysts undergo in situ transformation into metallic agglomerations during operation [179–181]. The utilization of a Cu SACs coordinated with nitrogen has demonstrated remarkable ethanol selectivity in ECO$_2$RR. Operando X-ray absorption spectroscopy (XAS) has indicated that isolated Cu species underwent reversible conversion to Cu NPs, which functioned as the authentic active sites during operation [180, 181]. The stability of Cu single sites during ECO$_2$RR and their ability to catalyze C–C coupling without undergoing initial structural changes that lead to Cu agglomeration is uncertain. In line with this, Zeng et al. reported a Cu coordination polymer (Cu(OH)BTA) with a stable single-site and periodic neighboring Cu centers, as illustrated in Fig. 19a [182]. The Cu(OH)BTA catalysts have been found to efficiently promote the conversion of CO$_2$ to C$_{2+}$ products, including ethylene, ethanol, acetate, and n-propanol, at a low overpotential with ethylene has been identified as the predominant product. At a potential of −0.87 V, the total FE of C$_{2+}$ was 73%, and a maximum FE of 57% for ethylene was achieved with a partial current density of 285 mA cm^{-2}. The FE for ethanol, acetate, and *n*-propanol reached 11%, 4%, and 1%, respectively (Fig. 19b). Cu(OH)BTA demonstrated a 1.5-fold enhancement in ethylene selectivity in comparison with its metallic analogue. Operando XAS and in situ Raman as well as infrared spectroscopies (Fig. 19c–f) revealed that Cu(OH)BTA retained its structural stability and did not undergo any dynamic transformation during ECO$_2$RR. Cyclic voltammetry (CV) studies were conducted in order to gain additional insight into the stability origins of the Cu(OH)BTA catalyst. The findings indicate that Cu(OH)BTA exhibits instability when subjected to Ar atmosphere during redox reactions involving Cu^{2+}/Cu^{1+}/Cu^0, and such instability was observed only after 10 scans. In contrast, the use of 1 M KOH as electrolyte in the same flow cell under a CO$_2$ atmosphere did not result in any redox process. The researchers postulated that the ECO$_2$RR had the ability to establish a favorable local environment that acted as a protective shield for the Cu(OH)BTA molecule against the harsh alkaline environment, thereby maintaining its structural integrity. The results obtained from DFT calculations indicate that the polymer's neighboring Cu atoms provide dual-Cu sites that are appropriately spaced. These sites facilitate the formation of an energetically suitable *OCCHO intermediate following a rate-determining step of CO hydrogenation. The energy barrier for C–C coupling was low, measuring 0.82 V, as illustrated in Fig. 19g and h.
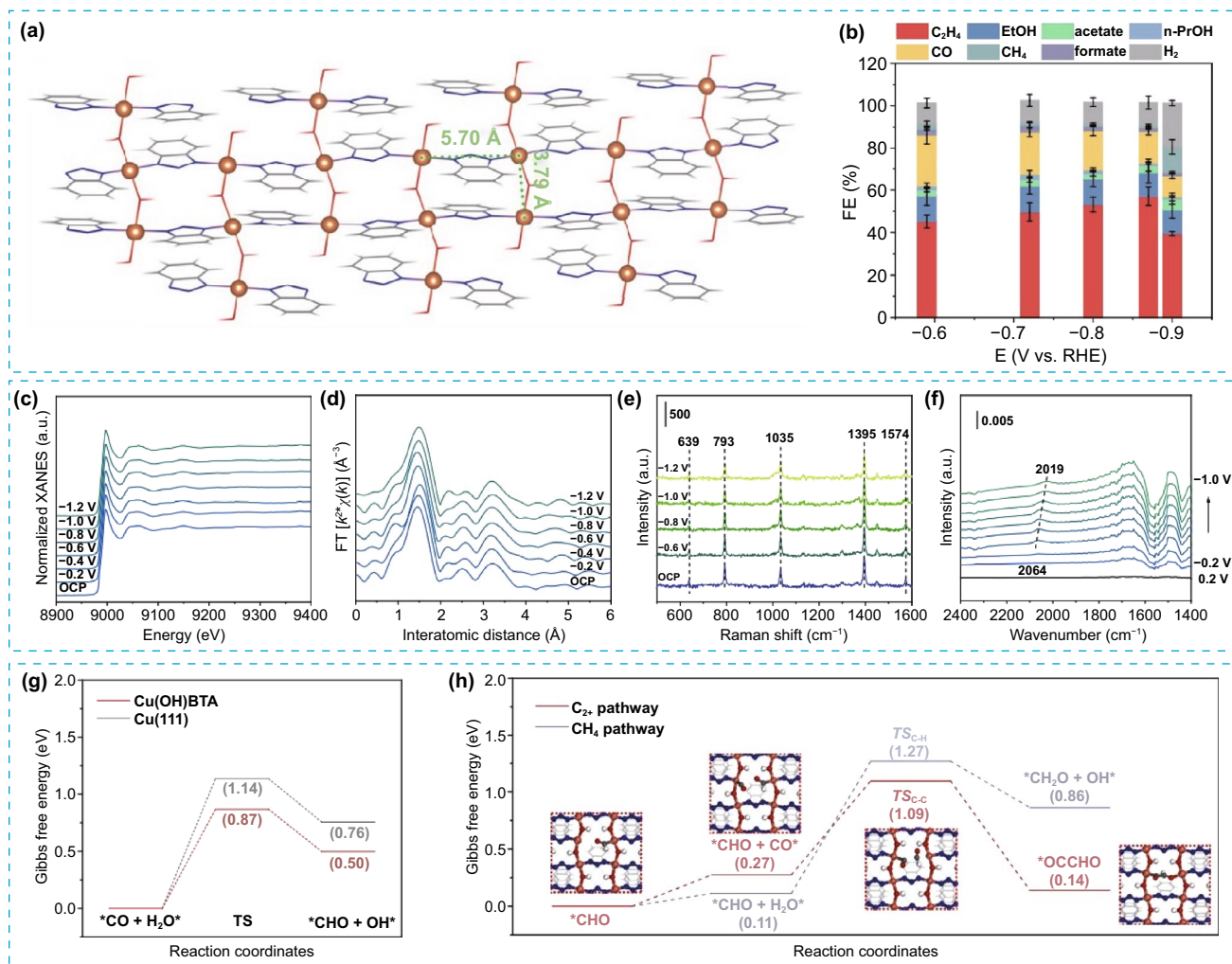
Fig. 19 a The proposed model of Cu(OH)BTA with isolated Cu atoms, **b** FEs of all products at different applied potentials over Cu(OH)BTA, **c** operando Cu K-edge XANES, **d** EXAFS of Cu(OH)BTA under CO_2 atmosphere at applied potentials ranging from -0.2 to -1.2 V, **e** in situ Raman spectra of Cu(OH)BTA under CO_2 atmosphere at the applied potential of -0.6 to -1.2 V, **f** in situ ATR-SEIRAS spectra of Cu(OH)BTA in CO_2-saturated 0.1 M $KHCO_3$ electrolyte at the applied potential of -0.2 to -1.0 V, **g** Gibbs free energy diagram of *CO hydrogenation on Cu(OH)BTA slab and Cu(111) slab, and **h** Gibbs free energy diagram of ECO_2RR to C_{2+} and CH_4 pathway on Cu(OH)BTA slab. Reproduced with permission [182]. Copyright 2023, Nature

It is noteworthy to mention that the effective conversion of CO_2 into C_3 products using Cu-based electrocatalysts is rarely reported. It is necessary to conduct an in-depth investigation of the reaction pathways of Cu-based electrocatalysts and their resultant products in order to gain a comprehensive understanding of the electrocatalytic CO_2 conversion to C_3 compounds. Chen et al. have recently reported that Cu SAs anchored in N-doped porous carbon (Cu-SA/NPC) catalysts can convert CO_2 to ethanol, acetic acid, and acetone products at a low overpotential. Interestingly, acetone was found to be the major product, with a production rate of 336.1 μg h^{-1} and a Faradaic efficiency of 36.7%. The authors performed an investigation into the impact of copper distribution and local coordination environment of Cu SAs in order to gain insight into the ECO_2RR to C_3 oxygenates [183]. The DFT calculations and the experimental results revealed that the high ability of Cu-SA/NPC catalyst for producing acetone from CO_2 reduction was ascribed to the crucial role of Cu-pyrrolic-N_4 active sites in stabilizing the intermediates associated with acetone production and promoting C–C coupling reactions owing to the synergistic effect in Cu–N configuration.

4 Summary and Outlook

This review provides an overview of the latest research advancements in Cu-based materials and their role in photocatalytic and electrocatalytic CO_2 reduction to C_{2+} products. The primary emphasis is placed on understanding the structure–activity relationships. The economic advantages of C_{2+} products surpass those of C_1 products, thereby underscoring the significance of developing efficient catalysts. The inherent advantages of Cu-based materials make them a promising option for CO_2 reduction processes. However, there is a need to improve maximum selectivity and intrinsic activity for C–C bond formation, which remains a challenge in C_{2+} chemical production.

Various strategies have been employed to enhance the effectiveness and selectivity of PCO_2RR toward C_{2+} products, including crystal phase and morphology optimization, metal doping, defect engineering, heterostructure fabrication, and bimetallic synergies. The aforementioned improvements are related to the semiconductor's ability to effectively separate and transfer photo-induced charge carriers to the active site with minimal recombination, concentrate electrons on the active site, increase CO_2 adsorption capacity, and facilitate C–C coupling reactions for the formation of C_{2+} products. The C–C coupling process in PCO_2RR involves stabilizing intermediates and accumulating electrons to reduce *CO intermediates into C_{2+} products. In order to enhance the reduction capability of the photocatalyst and extend its charge lifetime, it is imperative to adequately inhibit charge recombination and precisely adjust the conduction band's position toward a significantly negative direction.

Improving the proportion of Cu species can enhance the efficiency of Cu-based materials in PCO_2RR to C_{2+} compounds. Nevertheless, the influence of various ratios of copper valences on its catalytic activity has not been exhaustively studied due to difficulties in precisely controlling Cu^0, Cu^+, and Cu^{2+} ratios in Cu-based catalysts. Therefore, modifying the structural properties of these catalysts to enhance their PCO_2RR performance is a preferred research direction. Strategies such as pursuing controlled morphology and particle size with abundant efficient active sites as well as inducing surface defects can significantly improve the catalyst's performance. As example, engineering the defects or oxygen/metal vacancies on the surface of copper catalyst may create more efficient active sites and allows for a continuous supply of Cu^+ species to be available in sufficient amounts. Presently, the available methods for characterization are limited to the assessment of the microstructure and local coordination environment of the catalyst before and after the reaction. Therefore, it is necessary to employ sophisticated in situ/operando characterization methodologies to effectively to dynamically monitor the evolution of copper species on Cu-based materials under reaction conditions. Copper single-atom catalysts (Cu-SACs) exhibit great potential for effective photoconversion of CO_2 to C_{2+} products. However, despite their promising performance, they have not been widely investigated or examined. Hence, the development of Cu-SACs that enable C–C coupling for the production of higher hydrocarbon products is necessary. Optimization of the host material, incorporation of various dopants for anchoring Cu-SAs, or modification of the photoreaction parameters may potentially facilitate the aforementioned outcome.

Despite the significant progress in PCO_2RR to C_{2+} products, the selectivity for C_{2+} products over C_1 products, as well as the suppression of HER, remain inadequate for practical applications. This is due to various factors such as charge recombination and inefficient reaction rates. In addition, it is a commendable goal to produce C_{3+} products which possess higher energy and value compared to C_2 products. Despite the considerable differences in charge supply and density from electrochemistry, and the presence of a high kinetic barrier, empirical findings demonstrate the possibility of achieving CO_2 reduction C_{3+} products through photocatalysis, providing that near theoretical efficiency is attained.

Reaction conditions can have a significant impact on product selectivity. When compared to vapor-phase CO_2 reduction conditions, aqueous-phase CO_2 reduction reactions offer advantages in terms of charge and mass transfer processes, which are conducive to CO_2 reduction. However, the aqueous phase also tends to result in more pronounced competitive HER, which can lead to changes in product selectivity. Furthermore, the use of a suitable hole sacrificial agent can enhance the separation of photogenerated holes and electrons by eliminating the holes. This allows a greater number of photogenerated electrons to participate in photoreduction reactions, offering a better opportunity to produce C_{2+} products. Furthermore, to thoroughly investigate product

selectivity, it is imperative to employ a robust product detection system that can both qualitatively and quantitatively measure all possible products, even those found at extremely low concentrations. Developing such a detection system is of paramount importance, as it greatly contributes to achieving more accurate studies on reaction mechanisms and product selectivity.

For ECO_2RR to C_{2+} products, most of the electrocatalysts are made of Cu as the base due to its unique ability to facilitate the C–C coupling process. Nevertheless, attaining high FE at low overpotential for the production of C_{2+} chemicals, including ethylene and ethanol, remains a challenging task. Typically, these products are generated at higher potentials due to the necessity of surpassing the kinetic barriers of CO_2 intermediates associated with the progression toward the C_{2+} pathway. Various research studies have been conducted to optimize the properties of Cu-based catalysts for attaining high performance in ECO_2RR. Aspects such as morphology, surface composition, size, facet, defect density, and oxidation state are considered while designing these catalysts. The efficiency and selectivity of ECO_2RR on Cu catalysts depend largely on various factors such as the composition of the electrocatalyst, local pH, and applied potential. The improvement of catalytic activity/selectivity in Cu-based electrocatalysts can be attributed to several factors, which results in complexity in identifying the catalytic center driving the ECO_2RR performance. Although the supply of stable Cu^0 and oxidized Cu (Cu^+ or Cu^{2+}) is essential during catalysis, other factors such as particle size, surface area, facet, defect, and morphological effects also play a significant role in achieving excellent ECO_2RR performance. Thus, understanding the relationship between the Cu surface and CO_2RR activity is necessary to design effective catalysts for ECO_2RR in the future.

Moreover, incorporating secondary metals such as Pt, Ag, Au, or Zn into the single Cu crystal or Cu SAs catalyst has shown to be an effective strategy, as these alloys or bimetallic species have shown higher selectivity and stability toward C_{2+} products during ECO_2RR. The role of guest metals in altering the catalyst's electronic states, reaction kinetics, and binding energies of surface adsorbed intermediates depends on their arrangement on the Cu surface. The combination of metallic copper with secondary metals such as Au, Ag, and Zn may produce interfaces that change the electronic structure and facilitate tandem catalytic reactions, so enhancing the metals' intrinsic activity. The segregation of bimetallic

phases may potentially enhance the transfer of CO from the guest metal sites responsible for CO production to the Cu sites, thereby leading to an increase in the concentration of *CO on the active Cu sites, which could lead to higher C–C coupling rates. Tailoring Cu-based electrocatalysts with support materials like carbon or MOFs not only preserves the catalyst structure but also provides beneficial synergistic effects that improve catalytic efficiency.

Furthermore, the utilization of DFT calculation is imperative in investigating the correlation between the microstructure of Cu-based catalysts and their catalytic performance, given the rapid progressions in computer technology and artificial intelligence. Additionally, the implementation of machine learning techniques can facilitate the exploration of prospective Cu-based catalysts for the purpose of CO_2 reduction. The utilization of in situ and operando characterization techniques is crucial in recognizing the CO_2 reduction mechanism and identifying the intermediates produced during the reaction. Regarding this matter, the use of in situ infrared and Raman spectroscopy, alongside in situ and operando XAS and APXPS, has been found to offer reliable data, thereby enabling the suggestion of more precise reaction mechanisms. The combined use of in situ and operando analysis is urged for the investigation of the complex and ongoing controversial mechanism of CO_2 reduction reaction.

The advancement of technologies such as flow cells, GDE, and MEA has led to significant enhancements in reducing overpotential, improving Faradaic efficiency, increasing current density, and ensuring the stability of the ECO_2RR. As a result, the integrated approach of combining catalyst design with operational technology represents a promising avenue for achieving the production of C_{2+} products at a low economic cost. It is anticipated that practical applications of ECO_2RR will be realized in the industrial sector in the near future. Finally, this review aims to stimulate novel approaches in the design of Cu-based materials that can improve the efficiency of PCO_2RR and ECO_2RR in producing C_{2+} products.

Declarations

Conflict of interest The author declares no interest conflict. He has no known competing financial interests or personal relationships that could have appeared to influence the work reported in this paper.

References

1. J. Xie, R. Jin, A. Li, Y. Bi, Q. Ruan et al., Highly selective oxidation of methane to methanol at ambient conditions by titanium dioxide-supported iron species. Nat. Catal. **1**, 889–896 (2018). https://doi.org/10.1038/s41929-018-0170-x

2. S. Yao, X. Zhang, W. Zhou, R. Gao, W. Xu et al., Atomic-layered Au clusters on α-MoC as catalysts for the low-temperature water-gas shift reaction. Science **357**, 389–393 (2017). https://doi.org/10.1126/science.aah4321

3. E. Gong, S. Ali, C.B. Hiragond, H.S. Kim, N.S. Powar et al., Solar fuels: research and development strategies to accelerate photocatalytic CO_2 conversion into hydrocarbon fuels. Energy Environ. Sci. **15**, 880–937 (2022). https://doi.org/10.1039/D1EE02714J

4. S.I. Seneviratne, M.G. Donat, A.J. Pitman, R. Knutti, R.L. Wilby, Allowable CO_2 emissions based on regional and impact-related climate targets. Nature **529**, 477–483 (2016). https://doi.org/10.1038/nature16542

5. M. Forkel, N. Carvalhais, C. Rödenbeck, R. Keeling, M. Heimann et al., Enhanced seasonal CO_2 exchange caused by amplified plant productivity in northern ecosystems. Science **351**, 696–699 (2016). https://doi.org/10.1126/science.aac4971

6. Z.-J. Wang, H. Song, H. Liu, J. Ye, Coupling of solar energy and thermal energy for carbon dioxide reduction: status and prospects. Angew. Chem. Int. Ed. **59**, 8016–8035 (2020). https://doi.org/10.1002/anie.201907443

7. G.H. Han, J. Bang, G. Park, S. Choe, Y.J. Jang et al., Recent advances in electrochemical, photochemical, and photoelectrochemical reduction of CO_2 to C_{2+} products. Small **19**, 2205765 (2023). https://doi.org/10.1002/smll.202205765

8. X. Li, J. Wang, X. Lv, Y. Yang, Y. Xu et al., Hetero-interfaces on Cu electrode for enhanced electrochemical conversion of CO_2 to multi-carbon products. Nano-Micro Lett. **14**, 134 (2022). https://doi.org/10.1007/s40820-022-00879-5

9. C. Wang, Z. Sun, Y. Zheng, Y.H. Hu, Recent progress in visible light photocatalytic conversion of carbon dioxide. J. Mater. Chem. A **7**, 865–887 (2019). https://doi.org/10.1039/C8TA09865D

10. Y. Gao, K. Qian, B. Xu, Z. Li, J. Zheng et al., Recent advances in visible-light-driven conversion of CO_2 by photocatalysts into fuels or value-added chemicals. Carbon Resour. Convers. **3**, 46–59 (2020). https://doi.org/10.1016/j.crcon.2020.02.003

11. J. Albero, Y. Peng, H. García, Photocatalytic CO_2 reduction to C^{2+} products. ACS Catal. **10**, 5734–5749 (2020). https://doi.org/10.1021/acscatal.0c00478

12. S. Nitopi, E. Bertheussen, S.B. Scott, X. Liu, A.K. Engstfeld et al., Progress and perspectives of electrochemical CO_2 reduction on copper in aqueous electrolyte. Chem. Rev. **119**, 7610–7672 (2019). https://doi.org/10.1021/acs.chemrev.8b00705

13. M. Jouny, W. Luc, F. Jiao, General techno-economic analysis of CO_2 electrolysis systems. Ind. Eng. Chem. Res. **57**, 2165–2177 (2018). https://doi.org/10.1021/acs.iecr.7b03514

14. Q. Lu, F. Jiao, Electrochemical CO_2 reduction: electrocatalyst, reaction mechanism, and process engineering. Nano Energy **29**, 439–456 (2016). https://doi.org/10.1016/j.nanoen.2016.04.009

15. E. Vahidzadeh, S. Zeng, A.P. Manuel, S. Riddell, P. Kumar et al., Asymmetric multipole plasmon-mediated catalysis shifts the product selectivity of CO_2 photoreduction toward C_{2+} products. ACS Appl. Mater. Interfaces **13**, 7248–7258 (2021). https://doi.org/10.1021/acsami.0c21067

16. X. Wu, Y. Li, G. Zhang, H. Chen, J. Li et al., Photocatalytic CO_2 conversion of $M_{0.33}WO_3$ directly from the air with high selectivity: insight into full spectrum-induced reaction mechanism. J. Am. Chem. Soc. **141**, 5267–5274 (2019). https://doi.org/10.1021/jacs.8b12928

17. X. Li, J. Wang, X. Lv, Y. Yang, Y. Xu et al., Hetero-interfaces on Cu electrode for enhanced electrochemical conversion of CO_2 to multi-carbon products. Nanomicro Lett. **14**, 134 (2022). https://doi.org/10.1007/s40820-022-00879-5

18. V.S.S. Mosali, X. Zhang, Y. Liang, L. Li, G. Puxty et al., CdS-enhanced ethanol selectivity in electrocatalytic CO_2 reduction at sulfide-derived Cu–Cd. Chemsuschem **14**, 2924–2934 (2021). https://doi.org/10.1002/cssc.202100903

19. D. Zang, Q. Li, G. Dai, M. Zeng, Y. Huang et al., Interface engineering of Mo_8/Cu heterostructures toward highly selective electrochemical reduction of carbon dioxide into acetate. Appl. Catal. B Environ. **281**, 119426 (2021). https://doi.org/10.1016/j.apcatb.2020.119426

20. M.G. Méndez-Medrano, E. Kowalska, B. Ohtani, D. Bahena Uribe, C. Colbeau-Justin et al., Heterojunction of CuO nanoclusters with TiO_2 for photo-oxidation of organic compounds and for hydrogen production. J. Chem. Phys. **153**, 034705 (2020). https://doi.org/10.1063/5.0015277

21. Y. Song, M. Ichimura, H_2O_2 treatment of electrochemically deposited Cu_2O thin films for enhancing optical absorption. Int. J. Photoenergy **2013**, 738063 (2013). https://doi.org/10.1155/2013/738063

22. C.-F. Li, R.-T. Guo, Z.-R. Zhang, T. Wu, W.-G. Pan, Converting CO_2 into value-added products by Cu_2O-based catalysts: from photocatalysis, electrocatalysis to photoelectrocatalysis. Small **19**, 2207875 (2023). https://doi.org/10.1002/smll.202207875

23. W. Wang, L. Wang, W. Su, Y. Xing, Photocatalytic CO_2 reduction over copper-based materials: a review. J. CO2 Util. **61**, 102056 (2022). https://doi.org/10.1016/j.jcou.2022.102056

24. D.D. Zhu, J.L. Liu, S.Z. Qiao, Recent advances in inorganic heterogeneous electrocatalysts for reduction of carbon dioxide. Adv. Mater. **28**, 3423–3452 (2016). https://doi.org/10.1002/adma.201504766

25. Y. Lum, T. Cheng, W.A. Goddard 3rd., J.W. Ager, Electrochemical CO reduction builds solvent water into oxygenate products. J. Am. Chem. Soc. **140**, 9337–9340 (2018). https://doi.org/10.1021/jacs.8b03986

26. Y.Y. Birdja, E. Pérez-Gallent, M.C. Figueiredo, A.J. Göttle, F. Calle-Vallejo et al., Advances and challenges in understanding the electrocatalytic conversion of carbon dioxide to fuels. Nat. Energy **4**, 732–745 (2019). https://doi.org/10.1038/s41560-019-0450-y

27. W. Wang, C. Deng, S. Xie, Y. Li, W. Zhang et al., Photocatalytic C–C coupling from carbon dioxide reduction on copper oxide with mixed-valence copper(I)/copper(II). J. Am. Chem. Soc. **143**, 2984–2993 (2021). https://doi.org/10.1021/jacs.1c00206

28. F. Chang, M. Xiao, R. Miao, Y. Liu, M. Ren et al., Copper-based catalysts for electrochemical carbon dioxide reduction to multicarbon products. Electrochem. Energy Rev. **5**, 4 (2022). https://doi.org/10.1007/s41918-022-00139-5

29. M.K. Birhanu, M.-C. Tsai, A.W. Kahsay, C.-T. Chen, T.S. Zeleke et al., Copper and copper-based bimetallic catalysts for carbon dioxide electroreduction. Adv. Mater. Interfaces **5**, 1800919 (2018). https://doi.org/10.1002/admi.201800919

30. A. Bagger, W. Ju, A.S. Varela, P. Strasser, J. Rossmeisl, Electrochemical CO_2 reduction: a classification problem. ChemPhysChem **18**, 3266–3273 (2017). https://doi.org/10.1002/cphc.201700736

31. O. Zoubir, L. Atourki, H. Ait Ahsaine, A. BaQais, Current state of copper-based bimetallic materials for electrochemical CO_2 reduction: a review. RSC Adv. **12**, 30056–30075 (2022). https://doi.org/10.1039/D2RA05385C

32. W. Fu, Z. Liu, T. Wang, J. Liang, S. Duan et al., Promoting C^{2+} production from electrochemical CO_2 reduction on shape-controlled cuprous oxide nanocrystals with high-index facets. ACS Sustain. Chem. Eng. **8**, 15223–15229 (2020). https://doi.org/10.1021/acssuschemeng.0c04873

33. B. Liu, X. Yao, Z. Zhang, C. Li, J. Zhang et al., Synthesis of Cu_2O nanostructures with tunable crystal facets for electrochemical CO_2 reduction to alcohols. ACS Appl. Mater.

Interfaces **13**, 39165–39177 (2021). https://doi.org/10.1021/acsami.1c03850

34. X. Yuan, S. Chen, D. Cheng, L. Li, W. Zhu et al., Controllable Cu^0-Cu^+ sites for electrocatalytic reduction of carbon dioxide. Angew. Chem. Int. Ed. Engl. **60**, 15344–15347 (2021). https://doi.org/10.1002/anie.202105118

35. K. Yang, Z. Yang, C. Zhang, Y. Gu, J. Wei et al., Recent advances in CdS-based photocatalysts for CO_2 photocatalytic conversion. Chem. Eng. J. **418**, 129344 (2021). https://doi.org/10.1016/j.cej.2021.129344

36. M.Q. Yang, M. Gao, M. Hong, G.W. Ho, Visible-to-NIR photon harvesting: progressive engineering of catalysts for solar-powered environmental purification and fuel production. Adv. Mater. **30**, e1802894 (2018). https://doi.org/10.1002/adma.201802894

37. X. Zhang, F. Han, B. Shi, S. Farsinezhad, G.P. Dechaine et al., Photocatalytic conversion of diluted CO_2 into light hydrocarbons using periodically modulated multiwalled nanotube arrays. Angew. Chem. Int. Ed. **51**, 12732–12735 (2012). https://doi.org/10.1002/anie.201205619

38. S. Yan, J. Wang, H. Gao, N. Wang, H. Yu et al., An ion-exchange phase transformation to $ZnGa_2O_4$ nanocube towards efficient solar fuel synthesis. Adv. Funct. Mater. **23**, 758–763 (2013). https://doi.org/10.1002/adfm.201202042

39. L. Chen, M. Sun, J. Meng, B. Chu, X. Xie et al., Control of charge transfer direction by spatial engineering of redox active centers for boosting photocatalytic CO_2 reduction. Appl. Surf. Sci. **637**, 157948 (2023). https://doi.org/10.1016/j.apsusc.2023.157948

40. S. Verma, X. Lu, S. Ma, R.I. Masel, P.J.A. Kenis, The effect of electrolyte composition on the electroreduction of CO_2 to CO on Ag based gas diffusion electrodes. Phys. Chem. Chem. Phys. **18**, 7075–7084 (2016). https://doi.org/10.1039/c5cp05665a

41. C.M. Gabardo, A. Seifitokaldani, J.P. Edwards, C.-T. Dinh, T. Burdyny et al., Combined high alkalinity and pressurization enable efficient CO_2 electroreduction to CO. Energy Environ. Sci. **11**, 2531–2539 (2018). https://doi.org/10.1039/C8EE01684D

42. J. Wicks, M.L. Jue, V.A. Beck, J.S. Oakdale, N.A. Dudukovic et al., 3D-printable fluoropolymer gas diffusion layers for CO_2 electroreduction. Adv. Mater. **33**, e2003855 (2021). https://doi.org/10.1002/adma.202003855

43. F.P. García de Arquer, C.-T. Dinh, A. Ozden, J. Wicks, C. McCallum et al., CO_2 electrolysis to multicarbon products at activities greater than 1 A cm^{-2}. Science **367**, 661–666 (2020). https://doi.org/10.1126/science.aay4217

44. G. Díaz-Sainz, M. Alvarez-Guerra, A. Irabien, Continuous electroreduction of CO_2 towards formate in gas-phase operation at high current densities with an anion exchange membrane. J. CO2 Util. **56**, 101822 (2022). https://doi.org/10.1016/j.jcou.2021.101822

45. W. Lee, Y.E. Kim, M.H. Youn, S.K. Jeong, K.T. Park, Catholyte-free electrocatalytic CO_2 reduction to formate. Angew. Chem. Int. Ed. **57**, 6883–6887 (2018). https://doi.org/10.1002/anie.201803501

46. H.-K. Lim, H. Shin, W.A. Goddard 3rd., Y.J. Hwang, B.K. Min et al., Embedding covalency into metal catalysts for efficient electrochemical conversion of CO_2. J. Am. Chem. Soc. **136**, 11355–11361 (2014). https://doi.org/10.1021/ja503782w

47. K.A. Adegoke, R.O. Adegoke, A.O. Ibrahim, S.A. Adegoke, O.S. Bello, Electrocatalytic conversion of CO_2 to hydrocarbon and alcohol products: realities and prospects of Cu-based materials. Sustain. Mater. Technol. **25**, e00200 (2020). https://doi.org/10.1016/j.susmat.2020.e00200

48. U.J. Etim, C. Zhang, Z. Zhong, Impacts of the catalyst structures on CO_2 activation on catalyst surfaces. Nanomaterials **11**, 3265 (2021). https://doi.org/10.3390/nano11123265

49. X. Chang, T. Wang, J. Gong, CO_2 photo-reduction: insights into CO_2 activation and reaction on surfaces of photocatalysts. Energy Environ. Sci. **9**, 2177–2196 (2016). https://doi.org/10.1039/C6EE00383D

50. Megha, K. Mondal, A. Banerjee, T.K. Ghanty, Adsorption and activation of CO_2 on Zr_n ($n = 2$–7) clusters. Phys. Chem. Chem. Phys. **22**, 16877–16886 (2020). https://doi.org/10.1039/d0cp02505d

51. S.N. Habisreutinger, L. Schmidt-Mende, J.K. Stolarczyk, Photocatalytic reduction of CO_2 on TiO_2 and other semiconductors. Angew. Chem. Int. Ed. **52**, 7372–7408 (2013). https://doi.org/10.1002/anie.201207199

52. J. Li, S.U. Abbas, H. Wang, Z. Zhang, W. Hu, Recent advances in interface engineering for electrocatalytic CO_2 reduction reaction. Nano-Micro Lett. **13**, 216 (2021). https://doi.org/10.1007/s40820-021-00738-9

53. W. Tu, Y. Zhou, Z. Zou, Photocatalytic conversion of CO_2 into renewable hydrocarbon fuels: state-of-the-art accomplishment, challenges, and prospects. Adv. Mater. **26**, 4607–4626 (2014). https://doi.org/10.1002/adma.201400087

54. J. Fu, K. Jiang, X. Qiu, J. Yu, M. Liu, Product selectivity of photocatalytic CO_2 reduction reactions. Mater. Today **32**, 222–243 (2020). https://doi.org/10.1016/j.mattod.2019.06.009

55. S. Samanta, R. Srivastava, Catalytic conversion of CO_2 to chemicals and fuels. Mater. Adv. **1**, 1506–1545 (2020). https://doi.org/10.1039/D0MA00293C

56. Megha, A. Banerjee, T.K. Ghanty, Role of metcar on the adsorption and activation of carbon dioxide: a DFT study. Phys. Chem. Chem. Phys. **23**, 5559–5570 (2021). https://doi.org/10.1039/d0cp05756h

57. J. Jia, C. Qian, Y. Dong, Y.F. Li, H. Wang et al., Heterogeneous catalytic hydrogenation of CO_2 by metal oxides: defect engineering–perfecting imperfection. Chem. Soc. Rev. **46**, 4631–4644 (2017). https://doi.org/10.1039/C7CS00026J

58. A.K. Mishra, A. Roldan, N.H. de Leeuw, CuO surfaces and CO_2 activation: a dispersion-corrected DFT+U study. J. Phys. Chem. C **120**, 2198–2214 (2016). https://doi.org/10.1021/acs.jpcc.5b10431

59. J. Lee, D.C. Sorescu, X. Deng, Electron-induced dissociation of CO_2 on $TiO_2(110)$. J. Am. Chem. Soc. **133**, 10066–10069 (2011). https://doi.org/10.1021/ja204077e

60. W. Chu, Q. Zheng, O.V. Prezhdo, J. Zhao, CO_2 photoreduction on metal oxide surface is driven by transient capture of hot electrons: *Ab initio* quantum dynamics simulation. J. Am. Chem. Soc. **142**, 3214–3221 (2020). https://doi.org/10.1021/jacs.9b13280

61. S. Huygh, A. Bogaerts, E.C. Neyts, How oxygen vacancies activate CO_2 dissociation on TiO_2 anatase (001). J. Phys. Chem. C **120**, 21659–21669 (2016). https://doi.org/10.1021/acs.jpcc.6b07459

62. Z. Cheng, B.J. Sherman, C.S. Lo, Carbon dioxide activation and dissociation on ceria (110): a density functional theory study. J. Chem. Phys. **138**, 014702 (2013). https://doi.org/10.1063/1.4773248

63. P. Gao, S. Li, X. Bu, S. Dang, Z. Liu et al., Direct conversion of CO_2 into liquid fuels with high selectivity over a bifunctional catalyst. Nat. Chem. **9**, 1019–1024 (2017). https://doi.org/10.1038/nchem.2794

64. L. Liu, W. Fan, X. Zhao, H. Sun, P. Li et al., Surface dependence of CO_2 adsorption on Zn_2GeO_4. Langmuir **28**, 10415–10424 (2012). https://doi.org/10.1021/la301679h

65. H. Chen, T. Fan, Y. Ji, CO_2 reduction mechanism on the $Cu_2O(110)$ surface: a first-principles study. ChemPhysChem **24**, e202300047 (2023). https://doi.org/10.1002/cphc.202300047

66. L.I. Bendavid, E.A. Carter, CO_2 adsorption on $Cu_2O(111)$: a DFT+U and DFT-D study. J. Phys. Chem. C **117**, 26048–26059 (2013). https://doi.org/10.1021/jp407468t

67. Z. Gu, N. Yang, P. Han, M. Kuang, B. Mei et al., Oxygen vacancy tuning toward efficient electrocatalytic CO_2 reduction to C_2H_4. Small Methods **3**, 1800449 (2019). https://doi.org/10.1002/smtd.201800449

68. C. Hiragond, S. Ali, S. Sorcar, Su-Il In, Hierarchical nanostructured photocatalysts for CO_2 photoreduction. Catalysts **9**, 370 (2019). https://doi.org/10.3390/catal9040370

69. H. Molavi, A. Eskandari, A. Shojaei, S.A. Mousavi, Enhancing CO_2/N_2 adsorption selectivity via post-synthetic modification of NH_2-UiO-66(Zr). Microporous Mesoporous Mater. **257**, 193–201 (2018). https://doi.org/10.1016/j.micromeso.2017.08.043

70. X. Ma, L. Li, R. Chen, C. Wang, H. Li et al., Heteroatom-doped nanoporous carbon derived from MOF-5 for CO_2 capture. Appl. Surf. Sci. **435**, 494–502 (2018). https://doi.org/10.1016/j.apsusc.2017.11.069

71. R. Zhao, P. Ding, P. Wei, L. Zhang, Q. Liu et al., Recent progress in electrocatalytic methanation of CO_2 at ambient conditions. Adv. Funct. Mater. **31**, 2009449 (2021). https://doi.org/10.1002/adfm.202009449

72. J.T. Feaster, C. Shi, E.R. Cave, T. Hatsukade, D.N. Abram et al., Understanding selectivity for the electrochemical reduction of carbon dioxide to formic acid and carbon monoxide on metal electrodes. ACS Catal. **7**, 4822–4827 (2017). https://doi.org/10.1021/acscatal.7b00687

73. J. Santatiwongchai, K. Faungnawakij, P. Hirunsit, Comprehensive mechanism of CO_2 electroreduction toward ethylene and ethanol: the solvent effect from explicit water–Cu(100)

interface models. ACS Catal. **11**, 9688–9701 (2021). https://doi.org/10.1021/acscatal.1c01486

74. A.J. Garza, A.T. Bell, M. Head-Gordon, Mechanism of CO_2 reduction at copper surfaces: pathways to C_2 products. ACS Catal. **8**, 1490–1499 (2018). https://doi.org/10.1021/acscatal.7b03477

75. Z. Sun, T. Ma, H. Tao, Q. Fan, B. Han, Fundamentals and challenges of electrochemical CO_2 reduction using two-dimensional materials. Chem **3**, 560–587 (2017). https://doi.org/10.1016/j.chempr.2017.09.009

76. S. Pablo-García, F.L.P. Veenstra, L.R.L. Ting, R. García-Muelas, F. Dattila et al., Mechanistic routes toward C_3 products in copper-catalysed CO_2 electroreduction. Catal. Sci. Technol. **12**, 409–417 (2022). https://doi.org/10.1039/d1cy01423d

77. G.M. Tomboc, S. Choi, T. Kwon, Y.J. Hwang, K. Lee, Potential link between Cu surface and selective CO_2 electroreduction: perspective on future electrocatalyst designs. Adv. Mater. **32**, e1908398 (2020). https://doi.org/10.1002/adma.201908398

78. N.J. Azhari, N. Nurdini, S. Mardiana, T. Ilmi, A.T.N. Fajar et al., Zeolite-based catalyst for direct conversion of CO_2 to C_{2+} hydrocarbon: a review. J. CO2 Util. **59**, 101969 (2022). https://doi.org/10.1016/j.jcou.2022.101969

79. L. Liao, G. Xie, X. Xie, N. Zhang, Advances in modulating the activity and selectivity of photocatalytic CO_2 reduction to multicarbon products. J. Phys. Chem. C **127**, 2766–2781 (2023). https://doi.org/10.1021/acs.jpcc.2c08963

80. M.E. Aguirre, R. Zhou, A.J. Eugene, M.I. Guzman, M.A. Grela, Cu_2O/TiO_2 heterostructures for CO_2 reduction through a direct Z-scheme: protecting Cu_2O from photocorrosion. Appl. Catal. B Environ. **217**, 485–493 (2017). https://doi.org/10.1016/j.apcatb.2017.05.058

81. S. Rej, M. Bisetto, A. Naldoni, P. Fornasiero, Well-defined Cu_2O photocatalysts for solar fuels and chemicals. J. Mater. Chem. A **9**, 5915–5951 (2021). https://doi.org/10.1039/D0TA10181H

82. L. Yu, G. Li, X. Zhang, X. Ba, G. Shi et al., Enhanced activity and stability of carbon-decorated cuprous oxide mesoporous nanorods for CO_2 reduction in artificial photosynthesis. ACS Catal. **6**, 6444–6454 (2016). https://doi.org/10.1021/acscatal.6b01455

83. H. Huo, D. Liu, H. Feng, Z. Tian, X. Liu et al., Double-shelled Cu_2O/MnO_x mesoporous hollow structure for CO_2 photoreduction with enhanced stability and activity. Nanoscale **12**, 13912–13917 (2020). https://doi.org/10.1039/D0NR02944K

84. L. Cui, L. Hu, Q. Shen, X. Liu, H. Jia et al., Three-dimensional porous Cu_2O with dendrite for efficient photocatalytic reduction of CO_2 under visible light. Appl. Surf. Sci. **581**, 152343 (2022). https://doi.org/10.1016/j.apsusc.2021.152343

85. S. Wang, X. Bai, Q. Li, Y. Ouyang, L. Shi et al., Selective visible-light driven highly efficient photocatalytic reduction of CO_2 to C_2H_5OH by two-dimensional Cu_2S monolayers. Nanoscale Horiz. **6**, 661–668 (2021). https://doi.org/10.1039/d1nh00196e

86. H. Park, H.-H. Ou, A.J. Colussi, M.R. Hoffmann, Artificial photosynthesis of C1–C3 hydrocarbons from water and CO_2 on titanate nanotubes decorated with nanoparticle elemental copper and CdS quantum dots. J. Phys. Chem. A **119**, 4658–4666 (2015). https://doi.org/10.1021/jp511329d

87. P. Li, L. Liu, W. An, H. Wang, H. Guo et al., Ultrathin porous g-C_3N_4 nanosheets modified with AuCu alloy nanoparticles and C–C coupling photothermal catalytic reduction of CO_2 to ethanol. Appl. Catal. B Environ. **266**, 118618 (2020). https://doi.org/10.1016/j.apcatb.2020.118618

88. Y. Yu, X.-A. Dong, P. Chen, Q. Geng, H. Wang et al., Synergistic effect of Cu single atoms and Au–Cu alloy nanoparticles on TiO_2 for efficient CO_2 photoreduction. ACS Nano **15**, 14453–14464 (2021). https://doi.org/10.1021/acsnano.1c03961

89. S. Sorcar, Y. Hwang, J. Lee, H. Kim, K.M. Grimes et al., CO_2, water, and sunlight to hydrocarbon fuels: a sustained sunlight to fuel (Joule-to-Joule) photoconversion efficiency of 1%. Energy Environ. Sci. **12**, 2685–2696 (2019). https://doi.org/10.1039/C9EE00734B

90. Y. Zhang, B. Xia, J. Ran, K. Davey, S.Z. Qiao, Atomic-level reactive sites for semiconductor-based photocatalytic CO_2 reduction. Adv. Energy Mater. **10**, 1903879 (2020). https://doi.org/10.1002/aenm.201903879

91. J. Zhang, S. Yuan, J. Lin, $Cd_{1-x}Zn_xS$ nanorod solid solutions with sulfur vacancies as effective electron traps for highly efficient photocatalytic hydrogen evolution. J. Phys. Chem. C **125**, 25600–25607 (2021). https://doi.org/10.1021/acs.jpcc.1c08457

92. P. Xia, M. Antonietti, B. Zhu, T. Heil, J. Yu et al., Designing defective crystalline carbon nitride to enable selective CO_2 photoreduction in the gas phase. Adv. Funct. Mater. **29**, 1900093 (2019). https://doi.org/10.1002/adfm.201900093

93. J. Wang, C. Yang, L. Mao, X. Cai, Z. Geng et al., Regulating the metallic Cu–Ga bond by S vacancy for improved photocatalytic CO_2 reduction to C_2H_4. Adv. Funct. Mater. **33**, 2213901 (2023). https://doi.org/10.1002/adfm.202213901

94. C. Gao, J. Low, R. Long, T. Kong, J. Zhu et al., Heterogeneous single-atom photocatalysts: fundamentals and applications. Chem. Rev. **120**, 12175–12216 (2020). https://doi.org/10.1021/acs.chemrev.9b00840

95. M.B. Gawande, K. Ariga, Y. Yamauchi, Single-atom catalysts. Small **17**, 2101584 (2021). https://doi.org/10.1002/smll.202101584

96. Y. Xia, M. Sayed, L. Zhang, B. Cheng, J. Yu, Single-atom heterogeneous photocatalysts. Chem. Catal. **1**, 1173–1214 (2021). https://doi.org/10.1016/j.checat.2021.08.009

97. C.B. Hiragond, N.S. Powar, J. Lee, S.-I. In, Single-atom catalysts (SACs) for photocatalytic CO_2 reduction with H_2O: activity, product selectivity, stability, and surface chemistry. Small **18**, 2201428 (2022). https://doi.org/10.1002/smll.202201428

98. A. Zhang, M. Zhou, S. Liu, M. Chai, S. Jiang, Synthesis of single-atom catalysts through top-down atomization approaches. Front. Catal. **1**, 754167 (2021). https://doi.org/10.3389/fctls.2021.754167

99. X. Tan, H. Li, S. Yang, Single-atom catalysts-enabled reductive upgrading of CO_2. ChemCatChem **13**, 4859–4877 (2021). https://doi.org/10.1002/cctc.202100966

100. W. Xie, K. Li, X.-H. Liu, X. Zhang, H. Huang, P-mediated Cu–N_4 sites in carbon nitride realizing CO_2 photoreduction to C_2H_4 with selectivity modulation. Adv. Mater. **35**, e2208132 (2023). https://doi.org/10.1002/adma.202208132

101. G. Wang, C.-T. He, R. Huang, J. Mao, D. Wang et al., Photoinduction of Cu single atoms decorated on UiO-66-NH_2 for enhanced photocatalytic reduction of CO_2 to liquid fuels. J. Am. Chem. Soc. **142**, 19339–19345 (2020). https://doi.org/10.1021/jacs.0c09599

102. R. Xu, D.-H. Si, S.-S. Zhao, Q.-J. Wu, X.-S. Wang et al., Tandem photocatalysis of CO_2 to C_2H_4 via a synergistic rhenium-(I) bipyridine/copper-porphyrinic triazine framework. J. Am. Chem. Soc. **145**, 8261–8270 (2023). https://doi.org/10.1021/jacs.3c02370

103. N. Li, B. Wang, Y. Si, F. Xue, J. Zhou et al., Toward high-value hydrocarbon generation by photocatalytic reduction of CO_2 in water vapor. ACS Catal. **9**, 5590–5602 (2019). https://doi.org/10.1021/acscatal.9b00223

104. H. Shi, H. Wang, Y. Zhou, J. Li, P. Zhai et al., Atomically dispersed indium-copper dual-metal active sites promoting C–C coupling for CO_2 photoreduction to ethanol. Angew. Chem. Int. Ed. **61**, e202208904 (2022). https://doi.org/10.1002/anie.202208904

105. T. Wang, L. Chen, C. Chen, M. Huang, Y. Huang et al., Engineering catalytic interfaces in $Cu^{\delta+}$/CeO_2–TiO_2 photocatalysts for synergistically boosting CO_2 reduction to ethylene. ACS Nano **16**, 2306–2318 (2022). https://doi.org/10.1021/acsnano.1c08505

106. D. Zeng, H. Wang, X. Zhu, H. Cao, W. Wang et al., Photocatalytic conversion of CO_2 to acetic acid by CuPt/WO_3: chloride enhanced C–C coupling mechanism. Appl. Catal. B Environ. **323**, 122177 (2023). https://doi.org/10.1016/j.apcatb.2022.122177

107. Y. Shen, C. Ren, L. Zheng, X. Xu, R. Long et al., Room-temperature photosynthesis of propane from CO_2 with Cu single atoms on vacancy-rich TiO_2. Nat. Commun. **14**, 1117 (2023). https://doi.org/10.1038/s41467-023-36778-5

108. J.J. Plata, J. Graciani, J. Evans, J.A. Rodriguez, J.F. Sanz, Cu deposited on CeO_x-modified TiO_2(110): synergistic effects at the metal–oxide interface and the mechanism of the WGS reaction. ACS Catal. **6**, 4608–4615 (2016). https://doi.org/10.1021/acscatal.6b00948

109. J. Yang, Y. Huang, H. Qi, C. Zeng, Q. Jiang et al., Modulating the strong metal-support interaction of single-atom catalysts via vicinal structure decoration. Nat. Commun. **13**, 4244 (2022). https://doi.org/10.1038/s41467-022-31966-1

110. T. Pu, W. Zhang, M. Zhu, Engineering heterogeneous catalysis with strong metal–support interactions: characterization, theory and manipulation. Angew. Chem. Int. Ed. **62**, e202212278 (2023). https://doi.org/10.1002/anie.202212278

111. S. Yu, P.K. Jain, Plasmonic photosynthesis of C_1–C_3 hydrocarbons from carbon dioxide assisted by an ionic liquid. Nat. Commun. **10**, 2022 (2019). https://doi.org/10.1038/s41467-019-10084-5

112. H. Zhang, X. Chang, J.G. Chen, W.A. Goddard 3rd., B. Xu et al., Computational and experimental demonstrations of one-pot tandem catalysis for electrochemical carbon dioxide reduction to methane. Nat. Commun. **10**, 3340 (2019). https://doi.org/10.1038/s41467-019-11292-9

113. D.-L. Meng, M.-D. Zhang, D.-H. Si, M.-J. Mao, Y. Hou et al., Highly selective tandem electroreduction of CO_2 to ethylene over atomically isolated nickel-nitrogen site/copper nanoparticle catalysts. Angew. Chem. Int. Ed. **60**, 25485–25492 (2021). https://doi.org/10.1002/anie.202111136

114. T. Zhang, J.C. Bui, Z. Li, A.T. Bell, A.Z. Weber et al., Highly selective and productive reduction of carbon dioxide to multicarbon products via *in situ* CO management using segmented tandem electrodes. Nat. Catal. **5**, 202–211 (2022). https://doi.org/10.1038/s41929-022-00751-0

115. F. Zhang, Y.-H. Li, M.-Y. Qi, Z.-R. Tang, Y.-J. Xu, Boosting the activity and stability of Ag-Cu_2O/ZnO nanorods for photocatalytic CO_2 reduction. Appl. Catal. B Environ. **268**, 118380 (2020). https://doi.org/10.1016/j.apcatb.2019.118380

116. Z. Jiang, W. Wan, H. Li, S. Yuan, H. Zhao, P.K. Wong, A hierarchical Z-scheme α-Fe_2O_3/g-C_3N_4 hybrid for enhanced photocatalytic CO_2 reduction. Adv. Mater. **30**(10), 1706108 (2018). https://doi.org/10.1002/adma.201706108

117. B. Wang, J. Zhao, H. Chen, Y.-X. Weng, H. Tang et al., Unique Z-scheme carbonized polymer dots/$Bi_4O_5Br_2$ hybrids for efficiently boosting photocatalytic CO_2 reduction. Appl. Catal. B Environ. **293**, 120182 (2021). https://doi.org/10.1016/j.apcatb.2021.120182

118. C.-Y. Wu, C.-J. Lee, Y.-H. Yu, H.-W. Tsao, Y.-H. Su et al., Efficacious CO_2 photoconversion to C2 and C3 hydrocarbons on upright SnS–SnS_2 heterojunction nanosheet frameworks. ACS Appl. Mater. Interfaces **13**, 4984–4992 (2021). https://doi.org/10.1021/acsami.0c18420

119. I. Shown, H.C. Hsu, Y.C. Chang, C.H. Lin, P.K. Roy et al., Highly efficient visible light photocatalytic reduction of CO_2 to hydrocarbon fuels by Cu-nanoparticle decorated graphene oxide. Nano Lett. **14**, 6097–6103 (2014). https://doi.org/10.1021/nl503609v

120. H. Ge, B. Zhang, H. Liang, M. Zhang, K. Fang et al., Photocatalytic conversion of CO_2 into light olefins over TiO_2 nanotube confined Cu clusters with high ratio of Cu^+. Appl. Catal. B Environ. **263**, 118133 (2020). https://doi.org/10.1016/j.apcatb.2019.118133

121. L. Zhang, T. Liu, T. Liu, S. Hussain, Q. Li et al., Improving photocatalytic performance of defective titania for carbon dioxide photoreduction by Cu cocatalyst with SCN^- ion modification. Chem. Eng. J. **463**, 142358 (2023). https://doi.org/10.1016/j.cej.2023.142358

122. A.E. Nogueira, G.T.S.T. Silva, J.A. Oliveira, O.F. Lopes, J.A. Torres et al., CuO decoration controls Nb_2O_5 photocatalyst selectivity in CO_2 reduction. ACS Appl. Energy Mater. **3**, 7629–7636 (2020). https://doi.org/10.1021/acsaem.0c01047

123. H. Du, X. Gao, Q. Ma, X. Yang, T.-S. Zhao, Cu/PCN metal-semiconductor heterojunction by thermal reduction for

photoreaction of CO_2-aerated H_2O to CH_3OH and C_2H_5OH. ACS Omega **7**, 16817–16826 (2022). https://doi.org/10.1021/acsomega.2c01827

124. H. Du, Q. Ma, X. Gao, T.-S. Zhao, Cu/ZnV_2O_4 heterojunction interface promoted methanol and ethanol generation from CO_2 and H_2O under UV–vis light irradiation. ACS Omega **7**, 7278–7286 (2022). https://doi.org/10.1021/acsomega.1c07108

125. S. Xie, Y. Li, B. Sheng, W. Zhang, W. Wang et al., Self-reconstruction of paddle-wheel copper-node to facilitate the photocatalytic CO_2 reduction to ethane. Appl. Catal. B Environ. **310**, 121320 (2022). https://doi.org/10.1016/j.apcatb.2022.121320

126. N. Li, X. Liu, J. Zhou, W. Chen, M. Liu, Encapsulating CuO quantum dots in MIL-125(Ti) coupled with g-C_3N_4 for efficient photocatalytic CO_2 reduction. Chem. Eng. J. **399**, 125782 (2020). https://doi.org/10.1016/j.cej.2020.125782

127. X. Yu, V.V. Ordomsky, A.Y. Khodakov, Selective deposition of cobalt and copper oxides on $BiVO_4$ facets for enhancement of CO_2 photocatalytic reduction to hydrocarbons. ChemCatChem **12**, 740–749 (2020). https://doi.org/10.1002/cctc.201901115

128. J. Cai, Y. Xiao, Y. Tursun, A. Abulizi, Z-type heterojunction of Cu_2O-modified layered BiOI composites with superior photocatalytic performance for CO_2 reduction. Mater. Sci. Semicond. Process. **149**, 106891 (2022). https://doi.org/10.1016/j.mssp.2022.106891

129. D. Kim, C.S. Kley, Y. Li, P. Yang, Copper nanoparticle ensembles for selective electroreduction of CO_2 to C_2–C_3 products. Proc. Natl. Acad. Sci. U.S.A. **114**, 10560–10565 (2017). https://doi.org/10.1073/pnas.1711493114

130. B. Yang, L. Chen, S. Xue, H. Sun, K. Feng et al., Electrocatalytic CO_2 reduction to alcohols by modulating the molecular geometry and Cu coordination in bicentric copper complexes. Nat. Commun. **13**, 5122 (2022). https://doi.org/10.1038/s41467-022-32740-z

131. C.W. Li, M.W. Kanan, CO_2 reduction at low overpotential on Cu electrodes resulting from the reduction of thick Cu_2O films. J. Am. Chem. Soc. **134**, 7231–7234 (2012). https://doi.org/10.1021/ja3010978

132. Y. Song, R. Peng, D.K. Hensley, P.V. Bonnesen, L. Liang et al., High-selectivity electrochemical conversion of CO_2 to ethanol using a copper nanoparticle/N-doped graphene electrode. ChemistrySelect **1**, 6055–6061 (2016). https://doi.org/10.1002/slct.201601169

133. C. Reller, R. Krause, E. Volkova, B. Schmid, S. Neubauer et al., Selective electroreduction of CO_2 toward ethylene on nano dendritic copper catalysts at high current density. Adv. Energy Mater. **7**, 1602114 (2017). https://doi.org/10.1002/aenm.201602114

134. D. Ren, Y. Deng, A.D. Handoko, C.S. Chen, S. Malkhandi et al., Selective electrochemical reduction of carbon dioxide to ethylene and ethanol on copper(I) oxide catalysts. ACS Catal. **5**, 2814–2821 (2015). https://doi.org/10.1021/cs502128q

135. K.P. Kuhl, E.R. Cave, D.N. Abram, T.F. Jaramillo, New insights into the electrochemical reduction of carbon dioxide on metallic copper surfaces. Energy Environ. Sci. **5**, 7050–7059 (2012). https://doi.org/10.1039/C2EE21234J

136. K.L. Bae, J. Kim, C.K. Lim, K.M. Nam, H. Song, Colloidal zinc oxide-copper(I) oxide nanocatalysts for selective aqueous photocatalytic carbon dioxide conversion into methane. Nat. Commun. **8**, 1156 (2017). https://doi.org/10.1038/s41467-017-01165-4

137. A.S. Varela, M. Kroschel, T. Reier, P. Strasser, Controlling the selectivity of CO_2 electroreduction on copper: the effect of the electrolyte concentration and the importance of the local pH. Catal. Today **260**, 8–13 (2016). https://doi.org/10.1016/j.cattod.2015.06.009

138. C.T. Dinh, T. Burdyny, M.G. Kibria, A. Seifitokaldani, C.M. Gabardo et al., CO_2 electroreduction to ethylene via hydroxide-mediated copper catalysis at an abrupt interface. Science **360**, 783–787 (2018). https://doi.org/10.1126/science.aas9100

139. K.D. Yang, W.R. Ko, J.H. Lee, S.J. Kim, H. Lee et al., Morphology-directed selective production of ethylene or ethane from CO_2 on a Cu mesopore electrode. Angew. Chem. Int. Ed. Engl. **56**, 796–800 (2017). https://doi.org/10.1002/anie.201610432

140. A.S. Varela, W. Ju, T. Reier, P. Strasser, Tuning the catalytic activity and selectivity of Cu for CO_2 electroreduction in the presence of halides. ACS Catal. **6**, 2136–2144 (2016). https://doi.org/10.1021/acscatal.5b02550

141. Y. Lum, B. Yue, P. Lobaccaro, A.T. Bell, J.W. Ager, Optimizing C–C coupling on oxide-derived copper catalysts for electrochemical CO_2 reduction. J. Phys. Chem. C **121**, 14191–14203 (2017). https://doi.org/10.1021/acs.jpcc.7b03673

142. W. Luo, X. Nie, M.J. Janik, A. Asthagiri, Facet dependence of CO_2 reduction paths on Cu electrodes. ACS Catal. **6**, 219–229 (2016). https://doi.org/10.1021/acscatal.5b01967

143. T. Cheng, H. Xiao, W.A. Goddard 3rd., Full atomistic reaction mechanism with kinetics for CO reduction on Cu(100) from *ab initio* molecular dynamics free-energy calculations at 298 K. Proc. Natl. Acad. Sci. U.S.A. **114**, 1795–1800 (2017). https://doi.org/10.1073/pnas.1612106114

144. W. Tang, A.A. Peterson, A.S. Varela, Z.P. Jovanov, L. Bech et al., The importance of surface morphology in controlling the selectivity of polycrystalline copper for CO_2 electroreduction. Phys. Chem. Chem. Phys. **14**, 76–81 (2012). https://doi.org/10.1039/c1cp22700a

145. A. Eilert, F. Cavalca, F.S. Roberts, J. Osterwalder, C. Liu et al., Subsurface oxygen in oxide-derived copper electrocatalysts for carbon dioxide reduction. J. Phys. Chem. Lett. **8**, 285–290 (2017). https://doi.org/10.1021/acs.jpclett.6b02273

146. R. Yang, J. Duan, P. Dong, Q. Wen, M. Wu et al., *In situ* halogen-ion leaching regulates multiple sites on tandem catalysts for efficient CO_2 electroreduction to C_{2+} products. Angew. Chem. Int. Ed. **61**, e202116706 (2022). https://doi.org/10.1002/anie.202116706

147. B. Deng, M. Huang, K. Li, X. Zhao, Q. Geng et al., Crystal plane is not the key factor for CO_2-to-methane electrosynthesis on reconstructed Cu_2O microparticles. Angew. Chem. Int. Ed. **61**, 202114080 (2021). https://doi.org/10.1002/anie.202114080

148. P. De Luna, R. Quintero-Bermudez, C.-T. Dinh, M.B. Ross, O.S. Bushuyev et al., Catalyst electro-redeposition controls morphology and oxidation state for selective carbon dioxide reduction. Nat. Catal. **1**, 103–110 (2018). https://doi.org/10.1038/s41929-017-0018-9

149. Y. Hori, I. Takahashi, O. Koga, N. Hoshi, Electrochemical reduction of carbon dioxide at various series of copper single crystal electrodes. J. Mol. Catal. A Chem. **199**, 39–47 (2003). https://doi.org/10.1016/S1381-1169(03)00016-5

150. F.S. Roberts, K.P. Kuhl, A. Nilsson, High selectivity for ethylene from carbon dioxide reduction over copper nanocube electrocatalysts. Angew. Chem. Int. Ed. **54**, 5179–5182 (2015). https://doi.org/10.1002/anie.201412214

151. A. Loiudice, P. Lobaccaro, E.A. Kamali, T. Thao, B.H. Huang et al., Tailoring copper nanocrystals towards C_2 products in electrochemical CO_2 reduction. Angew. Chem. Int. Ed. **128**, 5883–5886 (2016). https://doi.org/10.1002/ange.201601582

152. M. Ma, K. Djanashvili, W.A. Smith, Controllable hydrocarbon formation from the electrochemical reduction of CO_2 over Cu nanowire arrays. Angew. Chem. Int. Ed. **55**, 6680–6684 (2016). https://doi.org/10.1002/anie.201601282

153. Z. Wang, G. Yang, Z. Zhang, M. Jin, Y. Yin, Selectivity on etching: creation of high-energy facets on copper nanocrystals for CO_2 electrochemical reduction. ACS Nano **10**, 4559–4564 (2016). https://doi.org/10.1021/acsnano.6b00602

154. H. Xiao, W.A. Goddard 3rd., T. Cheng, Y. Liu, Cu metal embedded in oxidized matrix catalyst to promote CO_2 activation and CO dimerization for electrochemical reduction of CO_2. Proc. Natl. Acad. Sci. U.S.A. **114**, 6685–6688 (2017). https://doi.org/10.1073/pnas.1702405114

155. H. Mistry, A.S. Varela, C.S. Bonifacio, I. Zegkinoglou, I. Sinev et al., Highly selective plasma-activated copper catalysts for carbon dioxide reduction to ethylene. Nat. Commun. **7**, 12123 (2016). https://doi.org/10.1038/ncomms12123

156. H. Jung, S.Y. Lee, C.W. Lee, M.K. Cho, D.H. Won et al., Electrochemical fragmentation of Cu_2O nanoparticles enhancing selective C–C coupling from CO_2 reduction reaction. J. Am. Chem. Soc. **141**, 4624–4633 (2019). https://doi.org/10.1021/jacs.8b11237

157. H. Xiao, T. Cheng, W.A. Goddard 3rd., Atomistic mechanisms underlying selectivities in C(1) and C(2) products from electrochemical reduction of CO on Cu(111). J. Am. Chem. Soc. **139**, 130–136 (2017). https://doi.org/10.1021/jacs.6b06846

158. T. Burdyny, P.J. Graham, Y. Pang, C.-T. Dinh, M. Liu et al., Nanomorphology-enhanced gas-evolution intensifies CO_2 reduction electrochemistry. ACS Sustain. Chem. Eng. **5**, 4031–4040 (2017). https://doi.org/10.1021/acssuschemeng.7b00023

159. P. Wang, H. Yang, C. Tang, Y. Wu, Y. Zheng et al., Boosting electrocatalytic CO_2-to-ethanol production via asymmetric C–C coupling. Nat. Commun. **13**, 3754 (2022). https://doi.org/10.1038/s41467-022-31427-9

160. C.G. Morales-Guio, E.R. Cave, S. Nitopi, J.T. Feaster, L. Wang et al., Improved CO_2 reduction activity towards C^{2+} alcohols on a tandem gold on copper electrocatalyst. Nat. Catal. **1**, 764–771 (2018). https://doi.org/10.1038/s41929-018-0139-9

161. W. Zhang, P. He, C. Wang, T. Ding, T. Chen et al., *Operando* evidence of Cu^+ stabilization *via* a single-atom modifier for CO_2 electroreduction. J. Mater. Chem. A **8**, 25970–25977 (2020). https://doi.org/10.1039/D0TA08369K

162. W. Guo, S. Liu, X. Tan, R. Wu, X. Yan et al., Highly efficient CO_2 electroreduction to methanol through atomically dispersed Sn coupled with defective CuO catalysts. Angew. Chem. Int. Ed. **60**, 21979–21987 (2021). https://doi.org/10.1002/anie.202108635

163. W. Li, L. Li, Q. Xia, S. Hong, L. Wang et al., Lowering C–C coupling barriers for efficient electrochemical CO_2 reduction to C_2H_4 by jointly engineering single Bi atoms and oxygen vacancies on CuO. Appl. Catal. B Environ. **318**, 121823 (2022). https://doi.org/10.1016/j.apcatb.2022.121823

164. J. Feng, L. Wu, S. Liu, L. Xu, X. Song et al., Improving CO_2-to-C_{2+} product electroreduction efficiency *via* atomic lanthanide dopant-induced tensile-strained CuO_x catalysts. J. Am. Chem. Soc. **145**, 9857–9866 (2023). https://doi.org/10.1021/jacs.3c02428

165. A. Vasileff, C. Xu, Y. Jiao, Y. Zheng, S.-Z. Qiao, Surface and interface engineering in copper-based bimetallic materials for selective CO_2 electroreduction. Chem **4**, 1809–1831 (2018). https://doi.org/10.1016/j.chempr.2018.05.001

166. Z. Yang, F.E. Oropeza, K.H.L. Zhang, P-block metal-based (Sn, In, Bi, Pb) electrocatalysts for selective reduction of CO_2 to formate. APL Mater. **8**, 060901 (2020). https://doi.org/10.1063/5.0004194

167. D. Ren, B.S.-H. Ang, B.S. Yeo, Tuning the selectivity of carbon dioxide electroreduction toward ethanol on oxide-derived Cu_xZn catalysts. ACS Catal. **6**, 8239–8247 (2016). https://doi.org/10.1021/acscatal.6b02162

168. Y. Feng, Z. Li, H. Liu, C. Dong, J. Wang et al., Laser-prepared CuZn alloy catalyst for selective electrochemical reduction of CO_2 to ethylene. Langmuir **34**, 13544–13549 (2018). https://doi.org/10.1021/acs.langmuir.8b02837

169. J. Huang, M. Mensi, E. Oveisi, V. Mantella, R. Buonsanti, Structural sensitivities in bimetallic catalysts for electrochemical CO_2 reduction revealed by Ag–Cu nanodimers. J. Am. Chem. Soc. **141**, 2490–2499 (2019). https://doi.org/10.1021/jacs.8b12381

170. T. Zhang, Z. Li, J. Zhang, J. Wu, Enhance CO_2-to-C_{2+} products yield through spatial management of CO transport in Cu/ZnO tandem electrodes. J. Catal. **387**, 163–169 (2020). https://doi.org/10.1016/j.jcat.2020.05.002

171. A.H.M. da Silva, S.J. Raaijman, C.S. Santana, J.M. Assaf, J.F. Gomes et al., Electrocatalytic CO_2 reduction to C_{2+} products on Cu and Cu_xZn_y electrodes: effects of chemical composition and surface morphology. J. Electroanal. Chem. **880**, 114750 (2021). https://doi.org/10.1016/j.jelechem.2020.114750

172. J. Timoshenko, H.S. Jeon, I. Sinev, F.T. Haase, A. Herzog et al., Linking the evolution of catalytic properties and structural changes in copper–zinc nanocatalysts using operando EXAFS and neural-networks. Chem. Sci. **11**, 3727–3736 (2020). https://doi.org/10.1039/D0SC00382D

173. T.T.H. Hoang, S. Verma, S. Ma, T.T. Fister, J. Timoshenko et al., Nanoporous copper–silver alloys by additive-controlled electrodeposition for the selective electroreduction of CO_2 to ethylene and ethanol. J. Am. Chem. Soc. **140**, 5791–5797 (2018). https://doi.org/10.1021/jacs.8b01868

174. D. Wei, Y. Wang, C.-L. Dong, Z. Zhang, X. Wang et al., Decrypting the controlled product selectivity over Ag–Cu bimetallic surface alloys for electrochemical CO_2 reduction. Angew. Chem. Int. Ed. **62**, e202217369 (2023). https://doi.org/10.1002/anie.202217369

175. Y. Pan, R. Lin, Y. Chen, S. Liu, W. Zhu et al., Design of single-atom co-N_5 catalytic site: a robust electrocatalyst for CO_2 reduction with nearly 100% CO selectivity and remarkable stability. J. Am. Chem. Soc. **140**, 4218–4221 (2018). https://doi.org/10.1021/jacs.8b00814

176. H. Zhang, J. Li, S. Xi, Y. Du, X. Hai et al., A graphene-supported single-atom FeN_5 catalytic site for efficient electrochemical CO_2 reduction. Angew. Chem. Int. Ed. **58**, 14871–14876 (2019). https://doi.org/10.1002/anie.201906079

177. Y. Cai, J. Fu, Y. Zhou, Y.-C. Chang, Q. Min et al., Insights on forming N, O-coordinated Cu single-atom catalysts for electrochemical reduction CO_2 to methane. Nat. Commun. **12**, 586 (2021). https://doi.org/10.1038/s41467-020-20769-x

178. A. Guan, Z. Chen, Y. Quan, C. Peng, Z. Wang et al., Boosting CO_2 electroreduction to CH_4 via tuning neighboring single-copper sites. ACS Energy Lett. **5**, 1044–1053 (2020). https://doi.org/10.1021/acsenergylett.0c00018

179. D.-H. Nam, O.S. Bushuyev, J. Li, P. De Luna, A. Seifitokaldani et al., Metal-organic frameworks mediate Cu coordination for selective CO_2 electroreduction. J. Am. Chem. Soc. **140**, 11378–11386 (2018). https://doi.org/10.1021/jacs.8b06407

180. D. Karapinar, N.T. Huan, N. Ranjbar Sahraie, J. Li, D. Wakerley et al., Electroreduction of CO_2 on single-site copper-nitrogen-doped carbon material: selective formation of ethanol and reversible restructuration of the metal sites. Angew. Chem. Int. Ed. **58**, 15098–15103 (2019). https://doi.org/10.1002/anie.201907994

181. H. Xu, D. Rebollar, H. He, L. Chong, Y. Liu et al., Highly selective electrocatalytic CO_2 reduction to ethanol by metallic clusters dynamically formed from atomically dispersed copper. Nat. Energy **5**, 623–632 (2020). https://doi.org/10.1038/s41560-020-0666-x

182. Y. Liang, J. Zhao, Y. Yang, S.-F. Hung, J. Li et al., Stabilizing copper sites in coordination polymers toward efficient electrochemical C–C coupling. Nat. Commun. **14**, 474 (2023). https://doi.org/10.1038/s41467-023-35993-4

183. K. Zhao, X. Nie, H. Wang, S. Chen, X. Quan et al., Selective electroreduction of CO_2 to acetone by single copper atoms anchored on N-doped porous carbon. Nat. Commun. **11**, 2455 (2020). https://doi.org/10.1038/s41467-020-16381-8